

Synthesis, Characterization, and Applications of Solution-processed Nanomaterials: From Thin-film Transistors to Flexible “Smart Bandages”

Sarah Swisher



Electrical Engineering and Computer Sciences
University of California at Berkeley

Technical Report No. UCB/EECS-2016-30

<http://www.eecs.berkeley.edu/Pubs/TechRpts/2016/EECS-2016-30.html>

May 1, 2016

Copyright © 2016, by the author(s).
All rights reserved.

Permission to make digital or hard copies of all or part of this work for personal or classroom use is granted without fee provided that copies are not made or distributed for profit or commercial advantage and that copies bear this notice and the full citation on the first page. To copy otherwise, to republish, to post on servers or to redistribute to lists, requires prior specific permission.

Synthesis, Characterization, and Applications of Solution-processed Nanomaterials:
From Thin-film Transistors to Flexible “Smart Bandages”

by

Sarah Lohry Swisher

A dissertation submitted in partial satisfaction of the

requirements for the degree of

Doctor of Philosophy

in

Engineering – Electrical Engineering and Computer Sciences

in the

Graduate Division

of the

University of California, Berkeley

Committee in charge:

Professor Vivek Subramanian, Chair

Professor Michel M. Maharbiz

Professor Oscar D. Dubon

Spring 2015

Synthesis, Characterization, and Applications of Solution-processed Nanomaterials:
From Thin-film Transistors to Flexible “Smart Bandages”

Copyright © 2015 by Sarah Lohry Swisher

All Rights Reserved

Abstract

Synthesis, Characterization, and Applications of Solution-processed Nanomaterials:
From Thin-film Transistors to Flexible “Smart Bandages”

by

Sarah Lohry Swisher

Doctor of Philosophy in Engineering – Electrical Engineering and Computer Sciences

University of California, Berkeley

Professor Vivek Subramanian, Chair

In parallel with the continued scaling of traditional CMOS devices, another paradigm of electronics has taken shape: *flexible electronic systems*. Flexible displays, electronic textiles, bio-inspired sensors, and wearable or implantable medical devices are just a few applications that benefit from large-area form factors and mechanical flexibility, both of which are challenging to achieve with conventional wafer-based electronics.

Advances in thin-film materials and devices over the past several decades have helped to drive the development of flexible electronics. Printing solution-based electronic materials is a particularly desirable path towards flexible devices. Because it is a purely additive process, printing results in lower overall process complexity, eliminates etching steps, and reduces material usage. Additive processing also enables the integration of various functional materials onto the same substrate, even when the materials or processing technologies would otherwise be incompatible. Printed electronics are compatible with low-cost roll-to-roll manufacturing techniques, offering a significant cost advantage over traditional microelectronic fabrication.

Solution-based electronic materials utilizing metal oxides (In_2O_3 , ZnO , SnO_2 , etc.) have been the focus of intense research efforts to enable high-performance printed electronics because of their high field-effect mobility in amorphous or disordered states. In this work, indium oxide nanocrystal inks are demonstrated as a promising pathway towards high-performance, air-stable, solution-processed transistors.. Thin-film transistors (TFTs) that utilize indium oxide nanocrystals as the channel material were developed, and the impact of materials synthesis and device fabrication on the TFT performance was explored in the context of printed electronic devices.

To highlight the merits of flexible electronics based on solution-processed nanomaterials and to demonstrate how these materials will enable innovation, one specific application was demonstrated. Biomonitoring devices benefit from lightweight form factors that can make conformal contact with the body, and are thus a particularly interesting proof-of-concept application. Here, a “smart bandage” prototype was designed to detect and monitor tissue wounds *in vivo*. A flexible, electronic device was developed that non-invasively maps pressure-induced tissue damage, even when such damage cannot be visually observed. Employing impedance spectroscopy across flexible electrode arrays *in vivo* on a rat model, it was observed that the frequency spectra of impedance measurements were correlated in a robust way with the state of the underlying tissue across multiple animals and wound types. Tissue damage detected using the impedance sensor is represented visually as a wound map, identifying regions at risk of developing a pressure ulcer and thus enabling intervention. These results demonstrate the feasibility of an automated, non-invasive “smart bandage” for early monitoring and diagnosis of pressure ulcers, improving patient care and outcomes.

To Charlie –

*“If you can imagine it,
you can achieve it.
If you can dream it,
you can become it.”*

- W.A. Ward

Acknowledgements

I cannot say enough to thank my advisor, Prof. Vivek Subramanian, for his guidance and support during my years at Berkeley. He struck just the right balance between providing direction and allowing me enough freedom to develop my own academic curiosity. He somehow knew when to challenge me and when to support me, and has helped me develop both competence and confidence in my research. He fostered a group culture of collaboration and camaraderie that made working in the lab even more enjoyable. He was the best teacher I've ever had, both in and out of the classroom. I am so grateful to him for being there to support me during the challenges I faced early in my graduate career; without him, I honestly do not think I would have reached my long-held goal of earning a Ph.D. and becoming a professor. Thank you, Vivek, for all that you have done for me in my academic, professional, and personal endeavors.

I have been fortunate to have many other excellent mentors at Berkeley. In particular, thank you to Prof. Oscar Dubon, Prof. Tsu-Jae King Liu, and Prof. Sayeef Salahuddin for their helpful feedback and direction while serving on my qualifying exam committee, and to Prof. Oscar Dubon and Prof. Michel Maharbiz for serving on my dissertation committee.

Of course this work would not have been possible without the support of all of my colleagues in the Printed Electronics group. In particular, Huai Yuan (Michael) Tseng, Lakshmi Jagannathan, Alejandro de la Fuente Vornbrock, and Steve Volkman helped me get started in my research career, even before I joined their group. Thanks to Rungrot (Jack) Kitsomboonloha for his kindness, for his willingness to teach, and for being such a positive and supportive group member. A special thanks to the Oxides group – Steve Volkman, Jaewon Jang, Andre Zeumault, and Will Scheideler – for their support and constructive criticism of my work. Jake Sadie was always there when I needed someone, whether it was to get coffee, proofread an abstract, or just to listen to me vent. Jake was also a great co-chair for planning our group's social events, so I have him to thank for corralling everyone to group football games, for a great ski trip, and for our summer BBQs. Gerd Grau has been a great friend, and I could always count on him for good feedback when I needed to bounce an idea off someone (not to mention an endless source of entertainment during Bayern Munich games).

During my graduate career, I was fortunate to have many excellent collaborators outside my research group as well. In particular, I am grateful to my colleagues at Berkeley and at UCSF that contributed to the success of impedance sensor project: Prof. Michel Maharbiz, Prof. Ana Claudia Arias, Monica Lin, Amy Liao, Yasser Khan, Felipe Pavinatto, Dr. Elisabeth Leeflang, Dr. Agne Naujokas, Prof. David Young, Prof. Shuvo Roy, and Prof. Michael Harrison. A special thanks to Michel for being an unofficial co-advisor, and to Ana for her support both professionally and personally. Thanks, as well, to Prof. Paul Alivisatos and his group members – in particular Jessy (Baker) Rivest, Charina Choi, Trevor Ewers, Ming Lee Tang, Jen Dionne, and Katie (Lutker) Lee – for their support during my early years

at Berkeley. A big thanks, as well, to the staff at the UC Berkeley Marvell Nanolab, the Stanford Nanocharacterization Lab, the Stanford Nanofabrication Facility, and the Stanford Synchrotron Radiation Lightsource.

I am grateful for the funding I have received from the National Science Foundation through the Graduate Research Fellowship Program, and from the Intel Foundation through the Robert Noyce Memorial Fellowship in Microelectronics.

Most importantly, I gratefully acknowledge the support of my amazing family. My husband, Greg, has given me the strength to persevere through the challenges of graduate school, and has given me a reason to smile every single day. He was always there to remind me of what really matters in life, never lost faith in me, and never let me give up on my dreams. Thank you, Greg, for everything you do; I literally could not have done this without you. I am also extremely grateful to our parents and my sisters for their unending love and support. You have all been my source of strength, hope, persistence, and joy; for that I will be forever filled with gratitude.

Table of Contents

CHAPTER 1: INTRODUCTION.....	1
1.1 FLEXIBLE ELECTRONICS: A NEW DIRECTION IN THE DIGITAL REVOLUTION	1
1.2 SOLUTION-PROCESSED ELECTRONIC DEVICES.....	3
1.2.1 <i>Advantages and challenges of solution-processing</i>	3
1.2.2 <i>Solution-processed electronic materials</i>	3
1.2.2.1 Sol-gels	3
1.2.2.2 Colloidal nanocrystals.....	5
1.3 METAL OXIDE SEMICONDUCTORS.....	7
1.3.1 <i>A high-performance alternative to amorphous silicon TFTs</i>	7
1.3.2 <i>Electron transport in amorphous metal oxide semiconductors</i>	7
1.4 APPLICATIONS FOR HIGH-PERFORMANCE SOLUTION-PROCESSED ELECTRONICS.....	9
1.4.1 <i>Next-generation displays</i>	9
1.4.2 <i>Flexible biological sensors</i>	9
1.5 MOTIVATION FOR THIS WORK	10
1.6 DISSERTATION OUTLINE.....	11
CHAPTER 2: SOLUTION-PROCESSED INDIUM OXIDE NANOCRYSTAL TFTS....	13
2.1 INTRODUCTION	13
2.2 METHODS.....	14
2.2.1 <i>Synthesis of indium oxide semiconductor nanocrystals</i>	14
2.2.2 <i>Fabrication of nanocrystal TFTs</i>	15
2.3 TAILORING THE NANOCRYSTAL SYNTHESIS FOR HIGH-PERFORMANCE TFTS	19
2.3.1 <i>Vacuum degassing</i>	19
2.3.2 <i>Nanocrystal growth temperature</i>	20
2.3.3 <i>Characterization of nanocrystals and TFTs using optimized synthesis</i>	24
2.4 MULTIFACTORIAL ANALYSIS OF TFT PROCESSING CONDITIONS.....	27
2.4.1 <i>Design of experiments</i>	27
2.4.2 <i>Experimental details</i>	30
2.4.3 <i>Results and discussion</i>	32
2.5 CONCLUSIONS.....	40
CHAPTER 3: BIOCOMPATIBLE FLEXIBLE ELECTRONICS.....	41
3.1 MOTIVATION: APPLICATIONS FOR BIOCOMPATIBLE ELECTRONICS	41
3.1.1 <i>Low-cost medical sensors</i>	42
3.1.2 <i>Body-integrated and wearable electronics</i>	43
3.1.3 <i>Energy harvesting and storage</i>	44
3.2 BIOCOMPATIBILITY STANDARDS.....	45
3.2.1 <i>Material toxicity tests for ISO 10993 biocompatibility standards</i>	46
3.2.2 <i>Toxicity considerations for solution-processed materials</i>	46
3.2.2.1 Particle size affects toxicity at the nanoscale.....	47
3.2.2.2 Residual contaminants in solution-processed materials	48
3.3 PROGRESS TOWARDS BIOCOMPATIBLE PRINTED ELECTRONICS	49
3.3.1 <i>High-performance biocompatible TFTs</i>	49
3.3.2 <i>Dissolution in a simulated body environment</i>	50
3.4 FUTURE STUDIES	52

3.4.1	<i>Promising material candidates</i>	52
3.4.2	<i>Dependence of toxicity on processing parameters</i>	52
3.5	CONCLUSIONS.....	54
CHAPTER 4: DETECTION OF PRESSURE ULCERS <i>IN VIVO</i>		55
4.1	INTRODUCTION	55
4.1.1	<i>Pressure ulcers: causes and prevention</i>	55
4.1.2	<i>Biological impedance measurements</i>	56
4.2	METHODS.....	58
4.2.1	<i>Two-dimensional electrode array for impedance mapping</i>	58
4.2.2	<i>Rigid electrode array board</i>	60
4.2.3	<i>Ink-jet printed electrode array</i>	60
4.2.4	<i>Rat model for pressure ulcers</i>	63
4.2.4.1	<i>Fluorescence angiography</i>	63
4.2.5	<i>Skin samples for histology</i>	65
4.2.6	<i>Impedance measurements</i>	65
4.2.6.1	<i>Minimizing parasitics: contact impedance and stray capacitance</i>	66
4.2.6.2	<i>Mounting the sensor array to the wound</i>	69
4.2.6.3	<i>Rejecting data from damaged electrode arrays</i>	70
4.2.6.4	<i>Four-point vs. two-point measurements, and the “current path problem”</i>	71
4.3	RESULTS.....	73
4.3.1	<i>Multiplexed electrode array maps tissue impedance</i>	73
4.3.2	<i>Impedance spectrum correlates to tissue health</i>	76
4.3.3	<i>Impedance spectroscopy identifies damage that is not visible</i>	79
4.3.4	<i>Cell membrane disruption correlates with impedance change</i>	81
4.3.5	<i>Applications extend beyond pressure ulcers</i>	82
4.4	CONCLUSIONS.....	83
CHAPTER 5: CONCLUSIONS & FUTURE OUTLOOK		85
5.1	SUMMARY	85
5.2	SUGGESTED FUTURE WORK	87
CHAPTER 6: BIBLIOGRAPHY		90
APPENDIX A: NANOCRYSTAL TFT FABRICATION PROCESS		100
APPENDIX B: IMPEDANCE SENSOR CONTROL BOARD CIRCUIT SCHEMATIC ..		101
APPENDIX C: IMPEDANCE SENSOR CONTROL BOARD BILL OF MATERIALS ..		103

List of Figures

Figure 1.1: Flexible electronics products and concepts.	2
Figure 1.2: Schematic of various routes in the sol-gel process.....	4
Figure 1.3: Schematic of nanoparticle sintering process.	6
Figure 1.4: Nanoparticle melting point vs. particle size.	6
Figure 1.5: Transport in metal oxides vs silicon.	8
Figure 2.1: Schematic of a Schlenk line apparatus for air-free reactions.	15
Figure 2.2: Indium oxide nanocrystal reaction scheme.	15
Figure 2.3: Nanocrystal TFT fabrication process flow.....	18
Figure 2.4: In ₂ O ₃ nanocrystal TFT structure.....	19
Figure 2.5: Effect of vacuum degassing on nanocrystal solubility.....	20
Figure 2.6: Effects of nanocrystal growth temperature.	22
Figure 2.7: Thickness and roughness of In ₂ O ₃ nanocrystal thin films.....	23
Figure 2.8: TEM images of In ₂ O ₃ nanocrystals.	24
Figure 2.9: XRD of In ₂ O ₃ nanocrystals, as deposited (no anneal).....	25
Figure 2.10: Transfer and output characteristics of In ₂ O ₃ nanocrystal TFTs.	26
Figure 2.11: TGA and DSC of In ₂ O ₃ nanocrystals.	29
Figure 2.12: Experimental design space for In ₂ O ₃ TFT processing conditions.....	30
Figure 2.13: Geometry of GIXD measurements.....	31
Figure 2.14: Analysis of GIXD data collected from 2D detector plate.	32
Figure 2.15: Effect test results for experimental input factors.....	33
Figure 2.16: In ₂ O ₃ nanocrystal TFT performance metrics vs processing conditions.	34
Figure 2.17: Transfer curves for In ₂ O ₃ TFTs vs anneal temperature.	35
Figure 2.18: Transfer and output curves for In ₂ O ₃ TFTs vs gate dielectric.....	36
Figure 2.19: GIXD of In ₂ O ₃ nanocrystals vs anneal condition.	37
Figure 2.20: GIXD of In ₂ O ₃ nanocrystals vs gate dielectric.....	38
Figure 2.21: Mobility of In ₂ O ₃ TFTs vs the effective electric field in the channel.	39
Figure 3.1: Potential applications for flexible bio-integrated electronics.....	42
Figure 3.2: Solution-processed optoelectronic sensor for pulse oximetry.....	43
Figure 3.3: Epidermal electronics.	44
Figure 3.4: Piezoelectric energy harvesting from heart motions.	45
Figure 3.5: <i>In vitro</i> tests for material toxicity.	46
Figure 3.6: Toxicity of ZnO powder vs ZnO nanoparticles.....	48
Figure 3.7: Transfer and output characteristics for SnO ₂ TFTs.....	50
Figure 3.8: Silicon-based transient electronics.	51
Figure 3.9: Dissolution of ZnO film in PBS.	51
Figure 4.1: Formation and stages of pressure ulcers.....	56
Figure 4.2: Simplified model of electric current through cells.	57
Figure 4.3: Biological impedance measurements.	59
Figure 4.4: Creating 2D impedance maps.....	60
Figure 4.5: Inkjet-printed flexible electrode array.....	61
Figure 4.6: 2D impedance sensor electrode arrays.	61

Figure 4.7: Formation of pressure ulcers on rat model.	63
Figure 4.8: Principle of fluorescence imaging with ICG.	64
Figure 4.9: Fluorescence angiography following ischemic event.	65
Figure 4.10: Wound measurement system diagram.	66
Figure 4.11: Parasitic impedance contributions.	67
Figure 4.12: De-embedding parasitic impedance from hardware.	68
Figure 4.13: Repeatability of impedance measurements with hydrogel.	69
Figure 4.14: Mounting sensor arrays on wounds.	70
Figure 4.15: Rejected pairs from damaged flexible electrode array.	71
Figure 4.16: Current path problem in 2-pt vs. 4-pt impedance measurements.	73
Figure 4.17: Average impedance using rigid vs. flexible array.	74
Figure 4.18: Flexible electrode array fabrication and characterization.	75
Figure 4.19: Reproducibility of the inkjet printing process.	76
Figure 4.20: Impedance spectrum correlates to severe, irreversible tissue damage.	78
Figure 4.21: Impedance maps identify mild, reversible pressure damage.	80
Figure 4.22: Three outcomes observed for pressure-induced tissue damage.	81
Figure 4.23: Histology of skin samples.	82
Figure 4.24: Impedance measurements of open wounds.	83

List of Tables

Table 1–1: Electron configuration of select metals.	8
Table 2–1: Summary of In ₂ O ₃ TFT linear mobility values.....	35
Table 3–1: Promising materials for biocompatible printed electronics.	52
Table 4–1: Specifications of flexible and rigid arrays.	62

Chapter 1: Introduction

In the nearly six decades since the first demonstration of an integrated circuit in 1958, the rapid growth of semiconductor technology has changed the world as we know it. Moore's Law and the "virtuous cycle" of investment, scaling, and market growth that have driven the semiconductor industry have had far-reaching effects on every aspect of our lives, our homes, our jobs, and our economy. The dramatic drop in the cost of computing power – from \$5.52 for a single transistor in 1954 to a billionth of a dollar in 2004 [1] – has enabled us to achieve myriad milestones from the Apollo missions to the Social Networking era.

In parallel with the continued scaling of traditional CMOS devices, another paradigm of electronics has taken shape: *flexible electronics*. Rather than focusing on shrinking critical dimensions and reducing power consumption, the growing field of flexible electronics aims to leverage compliant form factors and lightweight designs to enable new ways of integrating electronic devices into our lives. Flexible displays, electronic textiles, bio-inspired sensors, and wearable or implantable medical devices are just a few applications that are out of reach using the rigid form factor of conventional wafer-based electronics. Like the integrated circuit in the 1960s, flexible electronics could lead to a paradigm shift in the 21st century that would have a dramatic effect on our everyday lives.

1.1 Flexible Electronics: a New Direction in the Digital Revolution

Advances in thin-film materials and devices over the past several decades have helped to drive the development of flexible electronics [2]. Flexible devices are typically achieved by depositing thin-film transistors (TFTs) onto thin stainless steel or plastic substrates. Thin-film electronic materials not only cost less than crystalline substrates, but can also be deposited over a much larger area. This makes them a particularly good choice for low-cost and large-area applications, where the overall size of the system is the primary scaling metric rather than the transistor dimensions. Examples of several concepts and devices made possible by

flexible electronics are shown in Figure 1.1. Flexible power sources will be required to realize these devices; to this end, flexible thin-film solar photovoltaic (PV) cells and batteries are also research areas under rapid development.



Figure 1.1: Flexible electronics products and concepts.

Clockwise from top left: foldable map concept (display-central.com), Google glucose-sensing contact lens, stretchable ‘biostamp’ skin sensor (J.A. Rogers, UIUC), flexible transparent display concept from Phillips (mybroadband.co.uk), curved flexible phone concept (gizmag.com).

Currently, researchers in the field of flexible electronics aim to develop materials and patterning processes that increase TFT performance while decreasing the cost per unit area [3]. Significant efforts are devoted towards the development high-quality semiconductor materials that are compatible with the low-temperature processing requirements of inexpensive plastic substrates. A variety of material deposition techniques have been used that can be broadly categorized as either “top-down” or “bottom-up” manufacturing processes. “Top-down” approaches typically utilize standard silicon lithographic and etching techniques to create thin films, such as patterning the surface of a crystalline wafer into thin strips that can be transferred to a secondary flexible substrate. Alternatively, “bottom-up” assembly methods are chemical synthetic routes in which the composition, size, and morphology of the desired structure are well-controlled during the fabrication process [3], [4]. Bottom-up approaches are particularly attractive for nanoscale applications, in which top-down lithographic processes begin to face their fundamental scaling limits. Because they do not rely on expensive, fragile crystalline wafers as their starting material, bottom-up approaches also have the potential to enable flexible electronics at a low cost with greatly simplified manufacturing processes. One such bottom-up approach – printing electronics using solution-based materials – is discussed in more detail in the next section.

1.2 Solution-processed Electronic Devices

1.2.1 Advantages and challenges of solution-processing

Printing solution-based electronic materials is a particularly desirable path towards flexible electronics [5], [6]. Because it is a purely additive process, printing results in lower overall process complexity, eliminates etching steps, and reduces material usage. Additive processing also enables the integration of various functional materials onto the same substrate, even when the materials or processing technologies would otherwise be incompatible. For example, different TFT channel materials can be deposited to build sensing arrays, or to incorporate sensor devices with high-performance logic devices.

Although printed electronics have made great strides recently, challenges still exist that place limits on the transistor density and performance. The resolution of printed lines is much lower than what is achieved with lithography, and worse resolution leads to higher cost per function. The size and density of devices is further limited by the registration accuracy of the printers themselves. Furthermore, printing can result in poor quality films that yield low-performance materials and devices. Together, these limitations typically result in printed transistors that are relatively large (~1-100 micron features) and operate at frequencies below 1 MHz.

Despite these limitations, arguably the biggest advantage of solution-processing is *cost*; a thorough discussion is presented in reference [5]. The key point in the cost analysis is that printed electronics are very cheap *per unit area* compared to the traditional deposition, lithography, and etching that is required for silicon. It is not cheap *per transistor*, however, and thus printing is only economical for large-area applications with low transistor density and relatively low performance requirements. Overall, low cost roll-to-roll processing techniques, reduced tooling cost, reduced capital expenditure and increased throughput are expected to provide 10x cost advantages for printed electronics over conventional processes [5].

1.2.2 Solution-processed electronic materials

From a materials perspective, printed electronics require highly repeatable synthetic methods to produce consistently high-quality inks. Historically, most work on printed electronics has focused on organic systems, but inorganic materials are particularly interesting since they offer potential advantages in terms of performance, environmental stability, and transparency. Two key pathways towards solution-processed inorganic electronic materials have been recently explored for TFTs: (1) sol-gels, and (2) colloidal nanocrystals.

1.2.2.1 Sol-gels

In the broadest sense, the *sol-gel* method is defined as the preparation of ceramic materials by the preparation of a sol, gelation of the sol, and removal of the solvent [7]. The sol-gel method has been utilized to produce inorganic ceramic and glass materials since the mid-1800s [8]. Early sol-gel studies focused on silica gels, but more recently a quickly

progressing field of materials research has evolved that explores sol-gel routes to metal oxide thin films for solution-processed electronics. The following definitions are provided to aid the reader (based on the text by Brinker and Scherer [7]):

- A *colloid* is a suspension in which the dispersed phase is so small (1-1000 nm) that gravitational forces are negligible and interactions are dominated by short-range forces, such as van der Waals attraction and surface charges. The dispersed phase
- A *sol* is a colloidal suspension of solid particles in a liquid (as opposed to a liquid/liquid suspension (*emulsion*) or a solid/gas suspensions (*smoke*)).
- A *gel* is a two-phase substance in which one molecule reaches macroscopic dimensions such that it extends throughout the solution. It contains a continuous solid skeleton and a continuous liquid phase, both with colloidal dimensions ($\leq 1 \mu\text{m}$).

Dense metal oxide thin films can be formed using the sol-gel method, as illustrated in Figure 1.2. The precursors typically consist of a metal element surrounded by alkoxide, nitrate, or chloride ligands. The precursors are dissolved into a solvent to form a monomer solution; the nature of the complexes that are formed in solution (i.e. hydroxo [M—OH], oxo [M=O], etc.) are determined primarily by the properties of the metal and the pH of the solution [7]. The precursor solution can be deposited onto a substrate by printing or spin-coating. The solvent is removed during the deposition and during a subsequent drying process, resulting in densification of the film. A thermal treatment is usually necessary to eliminate excess precursor materials and further densify the film towards the target oxide composition.

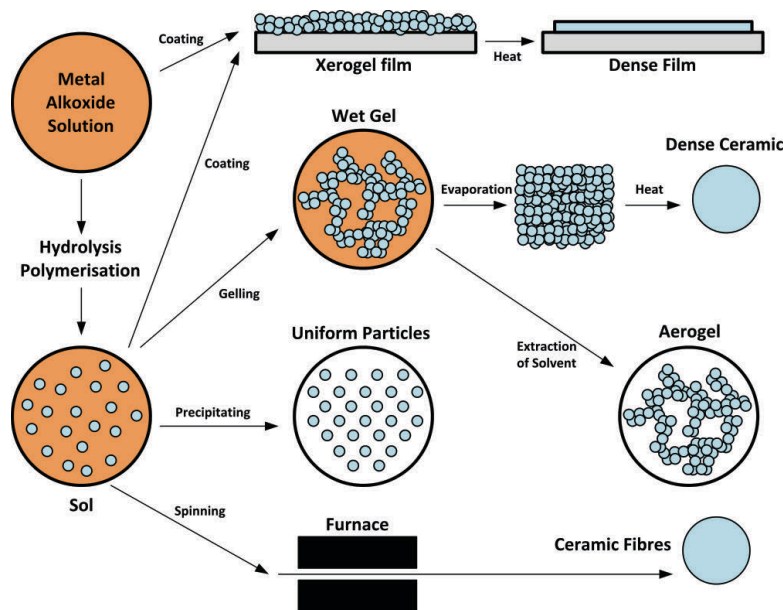


Figure 1.2: Schematic of various routes in the sol-gel process.

A metal oxide film can be produced by spin-coating a precursor solution or sol to form a dried gel (“xerogel”), and then using a thermal treatment to densify the film. Image source: Wikimedia Commons, adapted from [7].

The investigation of sol-gel routes to metal oxide thin films has mainly been driven by next-generation display applications. Progress in the last decade has led to the development of high-performance sol-gel TFTs [9]–[16], some exhibiting field effect mobilities as high as $\sim 40 \text{ cm}^2/\text{Vsec}$. However, despite the reports of high-performance sol-gel TFTs, it is widely recognized within the community that the device performance can be very sensitive to precursor solution preparation and processing (i.e., the sit-time or “aging” of the precursor solution, and how quickly the film is dried or annealed after deposition). For example, Lee et al. recently demonstrated that controlling the temperature of the precursor solution alters the ionic species in solution; this changes the metal-oxide lattice formation in the annealed film, thus significantly impacting the transport in the TFT [17]. Similarly, while sol-gels can indeed provide high-performance semiconductors [9], in some cases the device performance is degraded as the sol-gel ink ages. Unfortunately, the myriad process sensitivities have not been thoroughly studied, and their impacts are not always understood. These instabilities pose challenges both in terms of device uniformity and, ultimately, the large-scale manufacturability of such an approach to printed electronics.

1.2.2.2 Colloidal nanocrystals

Though much of the current printed electronics literature focuses on ink formulations based on inorganic sol-gels, colloidal semiconductor nanocrystals are an attractive alternative that may provide more stable inks. Colloidal nanocrystals consist of a solution-grown solid inorganic core with organic surfactant molecules attached to the surface [18], [19]. Technically speaking, the nanocrystals described in this section can be categorized as ‘sols’ as defined above; the key distinction between sol-gel and nanocrystal inks for printed electronics is the ability to precisely control the size, shape, crystal structure, and surface properties of nanocrystals, and to do so completely independently from the substrate.

Nanocrystals can be easily solubilized in printable solvents, providing a highly crystalline and phase-pure material in solution. Thus nanocrystals can combine the physical properties of inorganic solids with the low-cost, high-volume processing of plastics [19]. The ligands that help control particle growth during nanocrystal synthesis and provide solubility in the final ink formulation can be tuned to favor outcomes such as high mass loading or low sintering temperature [20], and post-synthesis ligand exchange procedures can allow further tailoring of the nanocrystal surface properties [21]. Unlike sol-gel formulations, the size and shape of colloidal nanocrystals are determined during the synthesis, and are thus unaffected by the thermal budget constraints of the substrate. In fact, this control over morphology and surface chemistry has already lead to the widespread use of sintered metal nanoparticles to form electrodes and interconnects in printed electronics.

Colloidal nanocrystals for thin-film semiconductors have been explored as well, though this work has primarily focused on exploiting the high degree of electronic coupling that is achieved in quantum confined particles of metal chalcogenides (CdSe, CdTe, PbSe, etc.); Talapin *et al.* provide a thorough review [22]. The significant drawbacks of chalcogenide materials have so far outweighed their potential benefits, however: they typically deliver poor TFT mobility due to the degraded transport resulting from the ligands that maintain quantum confinement in the film, they are inherently toxic, and their extreme sensitivity to air and

moisture requires all device fabrication and electrical characterization to be performed in an inert-atmosphere glovebox.

Rather than exploiting quantum confinement effects, an alternative approach to nanocrystal TFTs is to employ a sintering technique that deliberately removes encapsulation molecules and excess solvent, converting the solution-deposited layer into a high-performance thin film (Figure 1.3). Using this approach, the unique physical properties of nanocrystals provide significant benefits to printed electronics: the increased surface area to volume ratio of a nanoparticle leads to an increase in the surface energy, and a dramatic reduction in melting point as the size of the particle is reduced (Figure 1.4) [23]. As a result, printed nanoparticle films can be fused at relatively low temperatures (<150C in many cases) leading to properties close to those of thin films deposited by more conventional techniques at processing temperatures that are compatible with flexible plastic substrates [5].

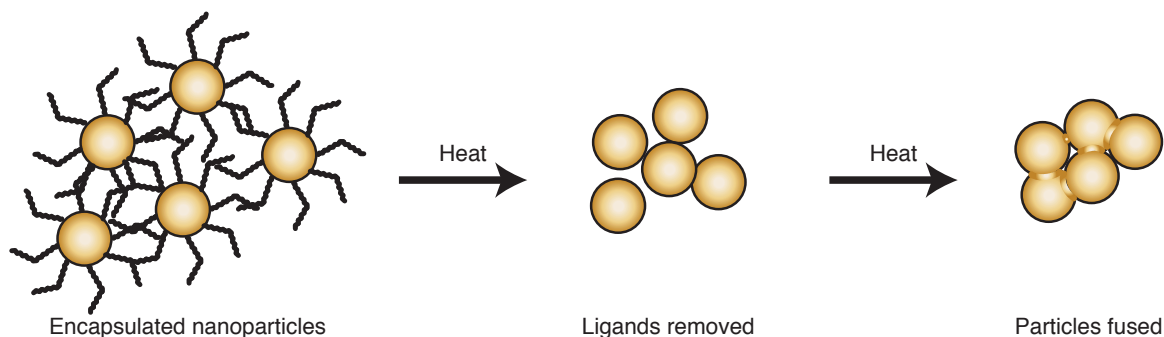


Figure 1.3: Schematic of nanoparticle sintering process.

Inorganic nanoparticles are encapsulated with organic ligands to control growth and solubility. After the particles are deposited onto a substrate, heat is applied to remove the ligands from the film and fuse the nanoparticles together to form percolation networks.

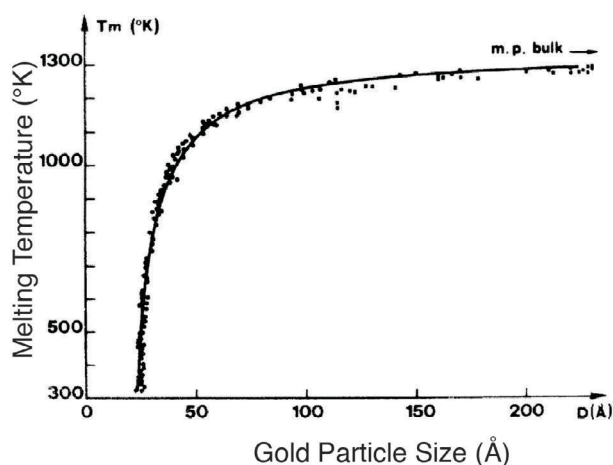


Figure 1.4: Nanoparticle melting point vs. particle size.

Reducing the size of gold particles results in a dramatic reduction in the melting point (m.p.) [23], allowing them to sinter at plastic-compatible temperatures.

1.3 Metal Oxide Semiconductors

A unique family of materials, metal oxide semiconductors (ZnO, In₂O₃, SnO₂, and combinations thereof), has been intensely studied in recent years as an alternative to amorphous silicon TFTs. Conductive oxides such as indium tin oxide (ITO) and oxide semiconductors such as ZnO have been used for decades, but there has been renewed interest in amorphous metal oxides for high-performance TFTs. The demonstration in 2004 of amorphous thin films of a quaternary metal oxide, In-Ga-Zn-O, with mobility an order of magnitude greater than that of amorphous silicon [24] has resulted in dramatic interest and rapid advances in this field.

1.3.1 A high-performance alternative to amorphous silicon TFTs

The primary application driving the requirements for TFTs is active matrix liquid crystal displays (LCDs). Amorphous silicon (a-Si) TFTs typically exhibit a mobility $< 1 \text{ cm}^2/\text{Vsec}$ and a subthreshold slope of $\sim 0.5 \text{ V/dec}$, which is sufficient for pixel switching but too slow to be used for the driving circuitry of the display [25]. Even though polysilicon has superior performance, a-Si has remained the dominant technology because polysilicon requires costly, complex processing [26]. In addition, grain boundaries in polysilicon act like shunt paths for impurities and water vapor, so – if the mobility is sufficient – amorphous materials are more desirable because they generally provide better uniformity over large areas [26].

Amorphous metal oxides offer the same benefits as amorphous silicon, with three key advantages[26]. First, metal oxides have 20~40x higher mobility than a-Si, enabling faster switching and higher current. Second, they can achieve this boost in performance even with low-temperature (or even room-temperature) fabrication processes. Amorphous silicon films are typically around deposited at 300-350°C, and the performance suffers when plastic-compatible temperatures ($< 200^\circ\text{C}$) are used. Third, metal oxides are transparent. Pixel transistors that do not block light lead to brighter displays with higher aperture ratios [26]. For these reasons, metal oxides are being pursued as a replacement for amorphous silicon, leading to significant research efforts into the fundamental device physics of these materials.

1.3.2 Electron transport in amorphous metal oxide semiconductors

One of the most attractive aspects of metal oxides is that the field effect mobility is not degraded severely in amorphous films compared to crystalline films. Metal oxide semiconductors are typically made up of some combination of zinc, gallium, indium, and tin. The electron configurations and the most common oxidation states of these elements are listed in Table 1–1. Note that, in their most common oxidation state, the *s*- and *p*-orbitals are empty. In these materials, it is the large spherical *s*-orbital of the metal that forms the conduction band minimum [24]. This is the key to achieving good transport in the amorphous phase.

Element	Electron Configuration	Oxidation state
Zinc (Zn)	[Ar] 4s ² 3d ¹⁰	+2
Gallium (Ga)	[Ar] 4s ² 3d ¹⁰ 4p ¹	+3
Indium (In)	[Kr] 4d ¹⁰ 5s ² 5p ¹	+3
Tin (Sn)	[Kr] 4d ¹⁰ 5s ² 5p ²	+4

Table 1–1: Electron configuration of select metals.

The electron configuration and the most common oxidation state of the elements that comprise metal oxide semiconductors result in empty *s*- and *p*-orbitals.

Figure 1.5 illustrates the benefit of the spherical *s*-orbital for amorphous transport, when compared to the sp^3 hybridization in silicon. Overlapping orbitals act like electron highways through the material, providing routes for efficient transport. In amorphous covalent semiconductors (such as silicon), the disorder disrupts the orbital overlap and carrier transport is controlled by hopping between localized tail states. In contrast, in metal oxides the conduction band is mainly composed of unoccupied *ns* orbitals which overlap with neighboring atoms, so disorder has a much less severe effect on transport. Because there is efficient transport even in amorphous films, high performance devices can be fabricated using low-temperature, low-cost methods such as printing.

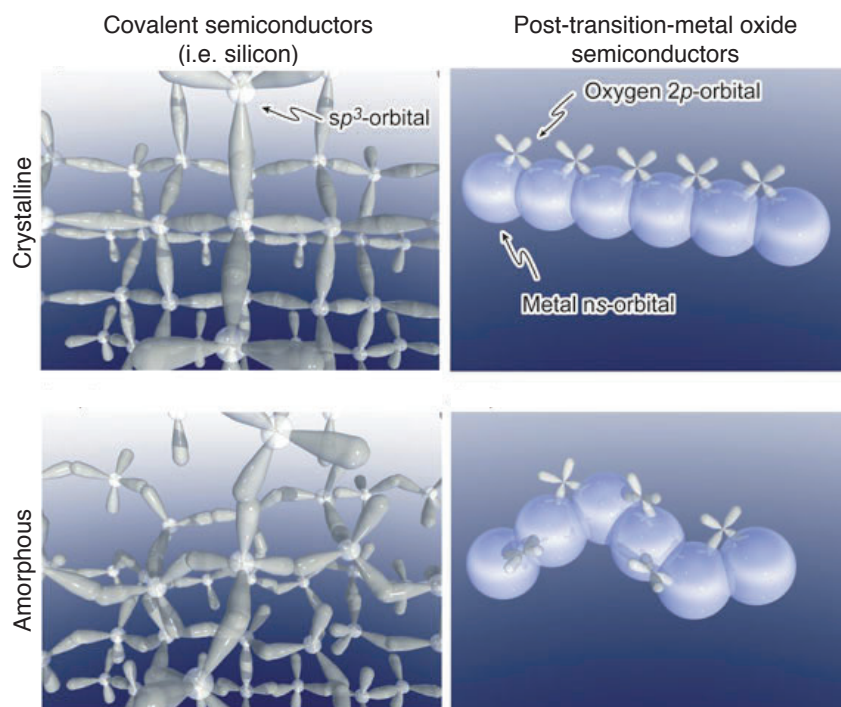


Figure 1.5: Transport in metal oxides vs silicon.

Schematic orbital drawings for the carrier transport paths in crystalline and amorphous semiconductors. The spherical orbitals of metal oxides are less disrupted by disorder than the hybridized sp^3 orbitals in silicon. Adapted from [24].

1.4 Applications for High-performance Solution-Processed Electronics

1.4.1 Next-generation displays

Amorphous silicon has been the material of choice for TFT backplane pixel transistors for decades. However, as the pixel density increases in high-resolution displays, the size of each pixel shrinks, and the size of each pixel transistor must scale proportionally to maintain the same brightness and aperture ratio. Higher mobility is required to obtain the same drive current from a smaller transistor, and a-Si TFTs will not be able to meet the demands of next-generation displays.

In addition to the trend towards higher resolution in the high-end display market, organic light emitting diodes (OLEDs) are emerging as a superior technology to LCDs in many ways. The main difference technologically is that OLEDs are emissive rather than passive, which means they don't require a backlight. They are superior in brightness, contrast, and viewing angle, and elimination of the backlight can result in thinner form factors and reduced cost. Brightness in OLEDs is proportional to current, so high-brightness displays require transistors that can source higher currents. Increasing the width of the TFT would increase the current, but at the expense of brightness because the aperture ratio decreases.

To address the growing need for higher performance pixel transistors, many display manufacturers are pursuing polysilicon as a replacement for a-Si because it exhibits much higher mobility. Unfortunately, that high performance comes at a substantially higher cost. Uniformity is also a challenge with polysilicon, causing problems when it is scaled up for large area displays.

Metal oxide semiconductors can address many of the challenges facing the display industry. These materials are an attractive option for next-generation displays because of their high mobility in the amorphous phase. The boost in mobility means oxide TFTs can be scaled down for high-resolution displays, and can provide sufficient current to drive OLEDs. Furthermore, metal oxides are also a promising route towards realizing transparent pixel transistors that do not block light, leading to brighter displays with higher aperture ratios. The superior performance of metal oxides can even be achieved when they are deposited using solution-processing methods. Thus, metal oxides can provide the additional benefits of additive manufacturing discussed previously: low cost for large area applications, less material waste, reduced processing complexity, and compatibility with flexible substrates.

1.4.2 Flexible biological sensors

When electronic circuits are mounted directly onto the skin, they have the potential to change the way health care is provided to patients. Non-invasive sensors placed on the body could collect data, then wirelessly transmit information directly to a doctor using a smartphone or computer. The ability to remotely diagnose or "self-monitor" medical conditions without traveling to a clinic could change the standard of care for myriad diseases

affecting elderly or immobile patients, as well as those in rural or medically underserved areas.

To this end, flexible and stretchable electronics for biomonitoring applications is currently an area of intense research focus [27]–[30]. Devices have been designed to measure physiological markers such as temperature, oxygenation, hydration level, and tissue strain. Therapeutic treatments such as the application of heat, electric stimulation, and drug delivery have also been demonstrated. Unlike traditional electronics based on rigid silicon wafers, flexible devices can make conformal contact with the body and be comfortably left in place for long periods of time. They can leverage low-cost manufacturing methods to make inexpensive devices that are designed to be single-use and disposable. Recent advancements in materials and device research have enabled rapid progress in the exciting field of ‘wearable electronics’, paving a path toward future innovations in health care.

1.5 Motivation for This Work

Though the field of flexible electronics has a bright future, significant advances in semiconductor materials, devices, and fabrication methods are needed to help realize its potential. Specifically, more progress is needed developing high performance solution-processed electronic materials and manufacturing methods that produce uniform devices over a large area (making them suitable for applications such as displays and sensors), with maximum processing temperatures that are compatible with display glass ($\leq 500^{\circ}\text{C}$) and plastic substrates ($\sim 200^{\circ}\text{C}$). To pave the way for these technologies to be used in pioneering medical devices, biocompatibility and flexible form factors must also be investigated.

To pursue these goals, this dissertation explores solution-processed nanomaterials for high-performance transistors and flexible electronics applications. First, the materials synthesis and transistor fabrication are explored in detail. For this work, the central focus is a solution-processed indium oxide semiconductor material. Among the family of metal oxide semiconductors discussed previously, indium oxide was chosen because of its propensity for high field-effect mobility: in many mixed metal oxide systems, higher indium content increases performance. A colloidal nanocrystal approach was chosen to obtain solution-processed thin films of indium oxide. As discussed previously, nanocrystals can be more precisely controlled (their composition, size, shape, etc.) than sol-gels, and thus may produce high-quality thin films for flexible electronics. Understanding the impacts of the nanocrystal preparation and thin film transistor fabrication procedures on device performance will be critical to the successful implementation of large-area low-temperature nanocrystal metal oxide TFTs.

After demonstrating the feasibility of high-performance nanocrystal-based semiconductor materials and devices, one particular application was chosen to highlight the potential impacts of flexible electronics based on solution-processed nanomaterials. As previously discussed, biomonitoring devices benefit from lightweight form factors that can make conformal contact with the body, and are thus a particularly interesting proof-of-concept application. Hence, a flexible sensing device – fabricated using gold nanoparticles inkjet-printed onto a thin,

flexible substrate – was designed to detect physiological changes in live tissue by measuring the complex impedance of skin. Pressure ulcers (also known as bedsores) were selected as a test case because of their clinical significance; treatment costs in the US alone are more than \$11 billion, roughly 29% of patients in long-term care facilities will experience a pressure ulcer, and there are more than 60,000 deaths each year that result from hospital-acquired pressure ulcers [31]. Impedance spectroscopy has been explored for decades to characterize biological tissues, but the fabrication of a flexible sensing array using nanocrystal inks enabled higher spatial resolution and reduced the parasitic impedance of the measurement apparatus. In doing so, the flexible ‘smart bandage’-like device was able to detect pressure-induced tissue damage with such sensitivity that physiological changes not visible to the clinician could be identified with the impedance sensor. While this is arguably only one specific application, it demonstrates the enormous potential for innovative biomedical devices that can be realized by pursuing flexible devices based on solution-processed nanomaterials.

1.6 Dissertation Outline

In Chapter 2, indium oxide nanocrystal inks are demonstrated as a promising pathway towards high-performance, air-stable, solution-processed transistors. First, the synthesis of indium oxide nanocrystals is presented. The impact of indium oxide nanocrystal synthesis conditions on TFT performance is explored in the context of printed electronic devices. Then, using a multifactorial approach, the effects of fabrication conditions on indium oxide nanocrystal TFTs is investigated. The annealing temperature, the annealing ambient, and the gate dielectric material are varied, and TFT parameters are reported from devices made at each condition. The experimental factors that have the most statistically significant impact on device performance are identified, illustrating the benefits of multifactorial experimental design techniques. The best conditions found within this experimental space yield devices with an average mobility of $10.5 \text{ cm}^2/\text{Vs}$, $I_{\text{ON}}/I_{\text{OFF}}$ ratio of above 10^6 , subthreshold swing of 0.25 V/decade , and a turn-on voltage of -1 V with negligible hysteresis. Semiconductor nanocrystal inks are shown to be a promising route towards exploiting the physical properties of inorganic solids while leveraging the low-cost manufacturing methods of large-area printing.

Chapter 3 proposes biocompatible routes towards solution-processed electronic devices. Building on the platform of materials and device development presented in Chapter 2, alternative printable materials are explored that are non-toxic and biocompatible. Unique aspects of toxicity in solution-based nanomaterials are discussed, and future experiments are proposed to assess the changes in material toxicity that may occur at the nanoscale.

In Chapter 4, a flexible biosensor is demonstrated as an example of how the materials and fabrication methods presented in Chapters 1 through 3 can enable innovative solutions in health care. A flexible, inkjet-printed electronic device was developed that non-invasively maps pressure-induced tissue damage, even when such damage cannot be visually observed. Employing impedance spectroscopy across flexible electrode arrays *in vivo* on a rat model, it is found that impedance is robustly correlated with tissue health across multiple animals and

Chapter 1: Introduction

wound types. These results demonstrate the feasibility of an automated, non-invasive “smart bandage” for early detection of pressure ulcers.

Finally, Chapter 5 summarizes the key contributions of this dissertation, and suggests directions for future studies based on this work.

Chapter 2: Solution-processed Indium Oxide Nanocrystal TFTs

2.1 Introduction

Recently, solution-processable routes to post-transition metal oxides (ZnO, SnO₂, In₂O₃, and combinations thereof) have been an area of intense focus among the printed electronics research community [9]–[16] because this family of materials can deliver electron mobilities in the amorphous phase an order of magnitude higher than amorphous silicon [24]. Many of these materials are also non-toxic, adding to their appeal. In these systems, indium is thought to be a key component for obtaining good transport properties [32], and is included in many ternary and quaternary metal oxide semiconductors (IZO, IGZO, IZTO, etc.) [10]–[16], [24]. Pure indium oxide has been less thoroughly studied as a solution-processed semiconductor material, though several reports of sol-gel indium oxide transistors thus far have been extremely promising [12]–[14]. Indium oxide nanocrystals are particularly attractive for solution-processed semiconductor thin films because they may be able to combine the high performance and straightforward processing techniques of sol-gels with the crystalline purity and size control of colloidal nanocrystals. Several groups have reported on the synthesis of In₂O₃ nanocrystals [33]–[36], but the few reports of indium oxide nanoparticle TFTs have exhibited poor transport (mobility values of 0.004 – 0.8 cm²/Vs) and poor electrostatic control (on/off current ratios of ~10³ and lower) [37], [38]. Further, the effect of synthetic conditions – including choice of reagents, reaction temperature, and purification methods – on the performance of printed electronics has not yet been studied.

In this chapter, a dramatic improvement in performance in indium oxide nanocrystal TFTs is realized; it is shown how nanoparticle synthetic and device processing conditions can be optimized to demonstrate high-performance transistors using colloidal In₂O₃ nanocrystals

as the solution-processed channel material, without the need for specialized inert-atmosphere fabrication or testing procedures. The motivation to use nanocrystals in this case is not to exploit quantum confinement effects; instead a sintering technique is employed that deliberately removes encapsulation molecules and excess solvent, converting the solution-deposited layer into a high-performance thin film [39], [40]. First, this chapter discusses the impact of the synthesis conditions of indium oxide nanocrystals on their performance as the semiconducting layer in TFTs. A synthetic method is presented that yields a high quality indium oxide nanocrystal ink for high-performance solution-processed electronics [41]. The next section of this chapter presents an investigation of the impact of fabrication and processing conditions on the performance of In_2O_3 nanocrystal TFTs using a full factorial experimental design [42]. Models of input factors and output responses are leveraged to determine the most statistically significant effects, which can provide guidance for future device optimization. The morphology of the In_2O_3 films was studied to elucidate the physical mechanisms responsible for the variation in TFT performance. Finally, a method is presented that can be used to more fairly compare the mobility of metal-oxide TFTs fabricated on different gate dielectrics by considering the effective transverse electric field in the channel region.

2.2 Methods

2.2.1 Synthesis of indium oxide semiconductor nanocrystals

A method for obtaining highly crystalline colloidal In_2O_3 nanocrystals published by Seo *et al.*[33] is used as a starting point. Soluble indium oxide nanocrystals were synthesized utilizing a one-pot thermal decomposition synthesis performed under argon atmosphere using standard air-free Schlenk line techniques; a diagram of a complete Schlenk line is illustrated in Figure 2.1, and the reaction scheme is shown Figure 2.2;. In a typical procedure, 1 mmol of indium (III) acetylacetonate (STREM Chemicals, 98%, CAS 14405-45-9) was mixed with 40 mmol of oleylamine (Sigma Aldrich, 70%, technical grade, CAS 112-90-3) in a 100 mL three-neck round-bottom-flask. The reaction was placed under vacuum (~ 100 mTorr), heated to 70°C over 10 minutes, then held at that temperature for 30 minutes to degas. The reaction was flushed three times with argon during the degassing period. The solution was then heated to 250°C over 30 minutes under flowing argon, and the reaction was allowed to proceed at that temperature for 4 hours. After cooling to room temperature, the flask was opened to air and 30 mL dichloromethane was added. Insoluble reaction products (if any) were removed by centrifugation (2000 rpm for 2 minutes), and then the nanocrystals were precipitated by centrifugation (5000 rpm for 10 minutes) with 120 mL ethanol. To remove excess surfactant, the particles were washed with ethanol and precipitated by centrifugation (2000 rpm for 2 minutes) three times. (Note that section 2.3 discusses modifications to this procedure to study the effect of different synthetic conditions on TFT performance.) The nanocrystals were redispersed in chloroform at a concentration of approximately 1 weight percent and transferred to a glass vial for storage. The size and morphology of the nanocrystals were investigated using a FEI Tecnai G2 F20 X-TWIN transmission electron microscope (TEM) at

an operating voltage of 200 kV. A SIEMENS D5000 X-Ray Diffractometer was used to determine the crystal structure.

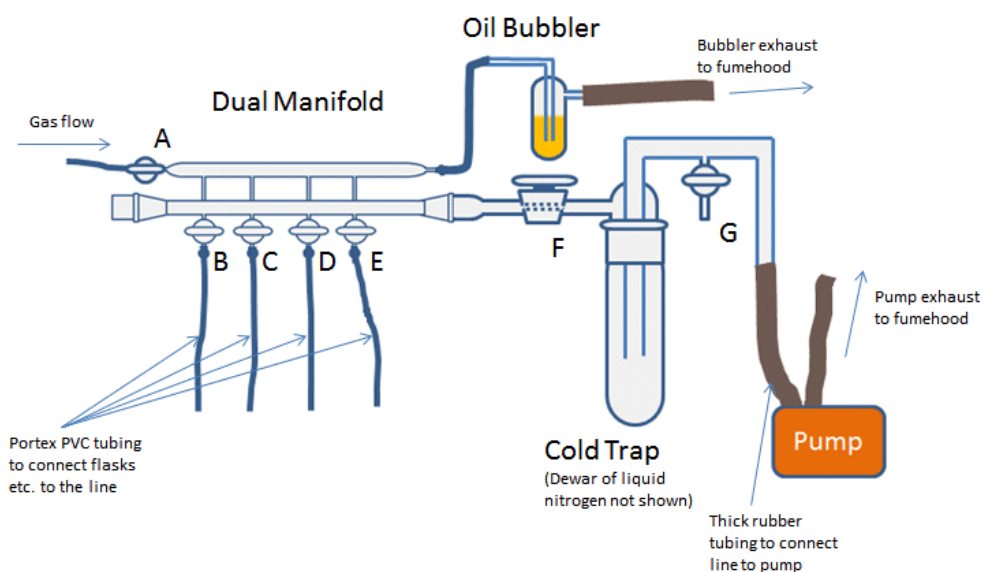


Figure 2.1: Schematic of a Schlenk line apparatus for air-free reactions.

Inert gas flows into the manifold through valve A. Reaction vessels are connected with flexible tubing to valves B-E, allowing each reaction to be connected either to inert gas or to the vacuum pump. A dewar of liquid nitrogen on the cold trap condenses contaminants to protect the vacuum pump, and an oil bubbler allows inert gas to flow without building up excess pressure inside the manifold. (Image source: www.chemistryviews.org.)

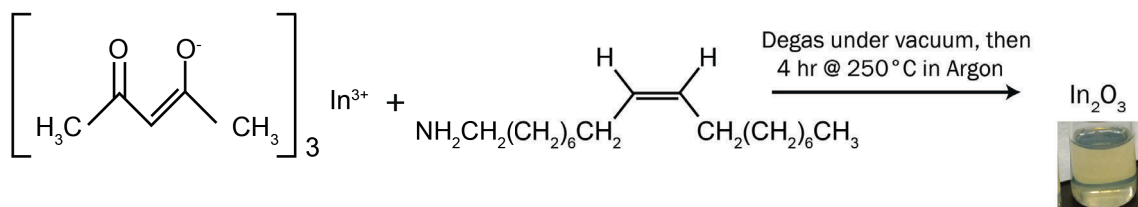


Figure 2.2: Indium oxide nanocrystal reaction scheme.

Indium (III) acetylacetonate is degassed with oleylamine, then heated under argon to grow indium oxide nanocrystals encapsulated with oleylamine.

2.2.2 Fabrication of nanocrystal TFTs

Bottom-gate, top-contact thin-film transistor (TFT) structures were fabricated utilizing the indium oxide nanocrystal solution as the channel material. The fabrication process flow is diagrammed in Figure 2.3; a more detailed step-by-step fabrication process is documented in the Appendix. The TFTs were fabricated as follows (the numbers below correspond to the step numbers in Figure 2.3):

1. All devices utilized heavily doped silicon wafers as the starting substrate and gate electrode, providing a robust test platform for the semiconductor material development and characterization.
2. Next, the gate dielectric was deposited. The purpose of this work was to develop and characterize the indium oxide nanocrystal semiconductor layer; for that reason, deposition methods were selected that could provide highly uniform dielectric layers to reduce experimental error from material variations. Metal oxide semiconductors have been shown to exhibit higher field-effect mobility when used with high- κ gate dielectrics so two types of devices were fabricated for this work.
 - A. For convenience and repeatability of testing, SiO₂ was used as the gate dielectric. Wafers were cleaned with piranha and hydrofluoric acid (HF), then 100 nm SiO₂ was grown in a dry oxidation furnace at 900°C.
 - B. For high-performance devices, a high- κ metal oxide was used as the gate dielectric. Zirconia (ZrO₂) was deposited using atomic layer deposition (ALD) in order to obtain smooth, uniform, and repeatable gate dielectric layers. Tetrakis (dimethylamido) zirconium (Zr(NMe₂)₄) was used as the zirconium precursor, and a substrate temperature of 200°C was maintained during the deposition. With these conditions, the ZrO₂ deposition rate was 0.9/Åcycle, with roughly 1% uniformity across a 4" silicon wafer. As discussed in section 2.4, other ALD films of high- κ gate dielectrics – Al₂O₃ and HfO₂ – were also investigated. The Al₂O₃ films were deposited under conditions similar to those described above for ZrO₂, while the HfO₂ films utilized an O₂ plasma-enhanced ALD process.
3. Indium oxide nanocrystals ~10 nm in diameter were synthesized following the method in section 2.2.1 and suspended in chloroform at a concentration of 1 wt%. Immediately prior to depositing the nanocrystal ink, the gate oxide layer was cleaned with piranha to ensure a clean semiconductor-gate dielectric interface; this was shown to have no effect on the leakage, breakdown strength, or dielectric constant of the high- κ gate oxide. The In₂O₃ nanocrystals were spin-coated onto the gate oxide at 5000 rpm for 60 seconds.
4. The semiconductor deposition was followed by an annealing step in a tube furnace; the standard procedure was a 1 hour anneal in oxygen at 500°C. This maximum processing temperature was chosen to remain glass-compatible. The oxygen-rich annealing environment was chosen because it resulted in TFTs with higher field-effect mobility. (Note that section 2.4 discusses modifications to this fabrication procedure to study the effect of different processing conditions on TFT performance.)
5. Source and drain regions were patterned using positive i-line photoresist to produce TFTs with W/L = 200 μm/40 μm.
6. Aluminum source/drain electrodes (80-100 nm thick) were deposited by electron beam evaporation. Aluminum was chosen because it makes an ohmic contact to the indium oxide semiconductor layer. Depositing aluminum using electron beam deposition proved to be a more reliable process with less contamination than thermal evaporation.

7. Excess aluminum was removed using a lift-off process by sonicating the devices in acetone. A lift-off process was selected rather than a metal etching step to minimize damage to the channel region while patterning the source and drain.
8. The active area of the TFTs was patterned using positive i-line photoresist and manual alignment to the source/drain electrodes. The photoresist defining the active area overlapped the source/drain electrodes by 10 μm to ensure that the aluminum was not damaged by the active area etching step.

The process described above was designed to produce large arrays of TFTs with uniform dimensions. Alternatively, the lithography in steps 5, 7, and 8 above can be omitted, and the aluminum can be deposited through a shadow mask to produce TFTs with $W/L = 200 \mu\text{m}/40 \mu\text{m}$. The active area can then be defined by manual trenching of the semiconductor. This simplified process does produce high-quality devices, but the shadow mask is less robust than lift-off and there is more error in the definition of the active area. Both patterning methods were used in this work. A schematic and a transmission electron microscope (TEM) cross-section image of a final device are shown in Figure 2.4. Film morphology and surface roughness were measured by atomic force microscopy (AFM) using a Digital Instruments Nanoscope 3100 AFM. TFTs were characterized using an HP 4155 Semiconductor Parameter Analyzer connected to a probe station. With the exception of the oxygen anneal, all processing was performed in air.

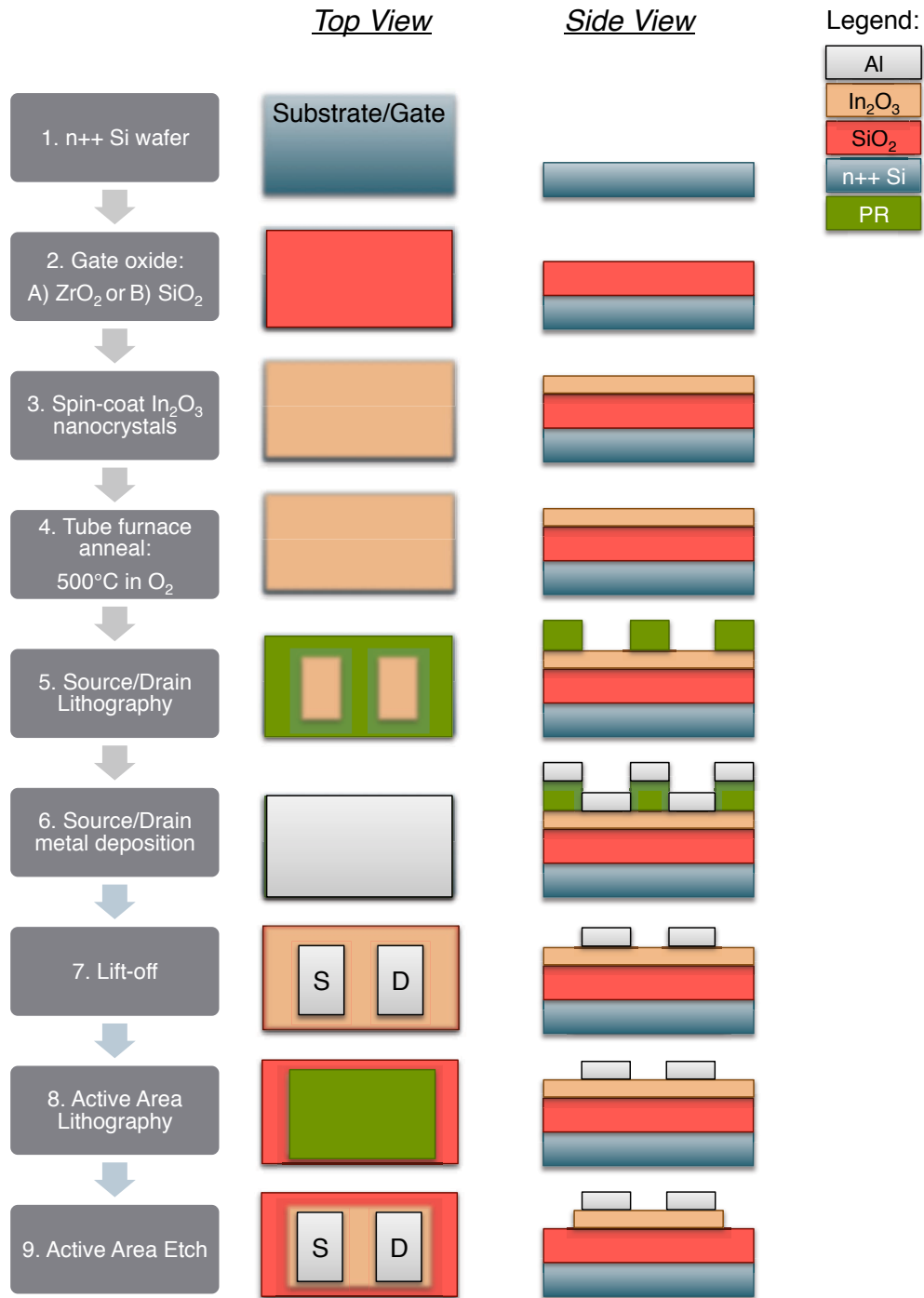


Figure 2.3: Nanocrystal TFT fabrication process flow
Schematic top view and side view of the nanocrystal TFT structures following each fabrication step.

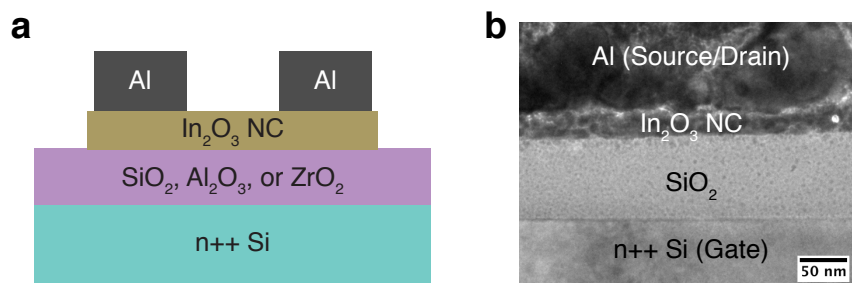


Figure 2.4: In₂O₃ nanocrystal TFT structure.

(a) Schematic and (b) a TEM cross-sectional image of an indium oxide nanocrystal TFT. The device shown in (b) was annealed for 1 hr at 500°C in oxygen.

2.3 Tailoring the Nanocrystal Synthesis for High-performance TFTs

2.3.1 Vacuum degassing

Many studies have demonstrated that the presence of even a small amount of water or organic impurities in a nanocrystal synthesis can have a significant impact on the outcome of the reaction [19]. Thus, the effect of a vacuum degassing step in the In₂O₃ nanocrystal synthesis procedure was investigated. The In₂O₃ particles resulting from a synthesis that included a 30 minute degas step at 70°C, during which time the reaction was purged three times with high-purity argon (our standard reaction) were compared with an otherwise identical reaction with the degas step omitted. A dramatic improvement was observed in the solubility of the final product in the reaction that included the degas step. When the two samples were redispersed in chloroform after collection from the reaction and washing in ethanol, the sample that underwent the vacuum degassing step dissolved immediately into a nearly transparent yellowish-blue solution. In contrast, upon dissolving the sample that was simply ramped to the growth temperature under argon flow without the vacuum step, a cloudy yellow solution was obtained. The marked improvement in solubility and lack of aggregation in solution was also observed by TEM (Figure 2.5).

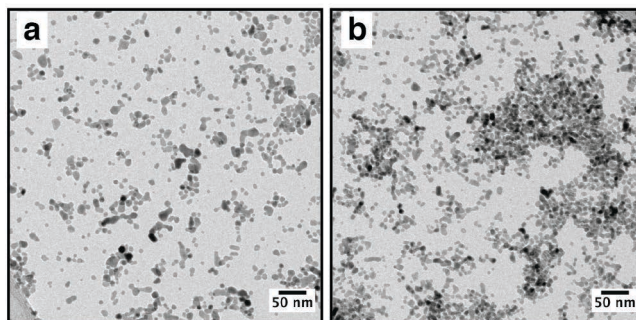


Figure 2.5: Effect of vacuum degassing on nanocrystal solubility.

Typical TEM images of In_2O_3 nanocrystals synthesized with (a) and without (b) a vacuum degas step. Using a vacuum degas step improved the solubility and reduced aggregation in solution.

In addition to the removal of water, the improvement in the solubility evident from this experiment may also be partially attributed to the removal of other contaminants present in the oleylamine. Technical grade oleylamine is only 70% pure as purchased, though it contains >98% primary amines. Shorter chain primary amines and saturated primary alkylamines will generally have lower boiling points than the oleylamine and thus be more easily removed during the vacuum degas step; this purification step may have contributed to the high batch-to-batch consistency that was observed following the synthetic procedure outline above. For example, despite the similar length and basicity of oleylamine and octadecylamine, previous studies have shown that using oleylamine as the stabilizer allowed better control of nanoparticle size [43]. In a study of Au nanoparticles, Lu and co-workers attributed a more stable precursor complex to the formation of a coordination bond between the C=C in oleylamine and the Au precursor, thus decreasing the precursor decomposition rate and the nanoparticle growth rate.

2.3.2 Nanocrystal growth temperature

Nanocrystal growth temperature is one of the most critical aspects of the synthetic procedure. Providing sufficient heat to the reaction turns the precursors into active atomic or molecular species (*monomers*). The characteristics of the nanoparticles are determined by the competing processes of nucleation and growth during the reaction. In the nucleation phase, precursors rapidly decompose resulting in a supersaturation of monomers, then the nucleation of nanocrystal “seeds”. Monomers remaining in solution following the nucleation event are consumed during the growth phase: monomers add to the nanocrystal seeds in solution, and the particles grow. To obtain high quality crystals, the reaction temperature must be sufficiently high to allow rearrangement of the atoms during growth, and to provide dynamic solvation by the surfactant molecules [19]. The binding strength of surfactant molecules and the stability and diffusion rate of the intermediate complexes in the reaction solution are all strongly dependent on the reaction temperature: increasing the temperature greatly reduces the stability of intermediate complexes in the solution and increases their diffusion rates, thus inducing nanocrystal nucleation and growth. Excessive temperature, however, can lead to rapid and uncontrolled growth, such that subtle kinetic or energetic effects cannot be leveraged to precisely control particle size and shape. During the course of the In_2O_3

synthesis, a visible change in the reaction was observed from transparent yellow to dark grey at a temperature of approximately 215°C, then another abrupt change back to a yellowish translucent color at approximately 240°C. No further color change was observed up to 260°C, until the reaction was cooled to room temperature. To investigate the effect of nanocrystal growth temperature on the performance of solution-processed nanocrystal TFTs, the synthesis was repeated with varied reaction temperatures between 210°C and 260°C. Each batch of nanocrystals was examined using TEM, then transistors were fabricated and the extracted linear field effect mobility was used as a metric for comparing TFT performance.

At low growth temperatures, polydisperse nanocrystals with poor solubility were observed, resulting in non-uniform solution-processed semiconductor films. Large multicrystalline particles were observed in the TEM images for temperatures up to 230°C (Figure 2.6a, left). It is unclear from the TEM images whether the large particles are the result of a small number of nucleation events followed by excessive growth, or if they are aggregations of many smaller particles. These nanocrystal solutions appeared cloudy immediately following synthesis, and after ~24 hours the particles had flocculated and precipitated out of solution. Correspondingly, spin-coated films made using these poorly solubilized particles were non-uniform at the device scale, exhibiting thick streaks and/or patchy deposition (Figure 2.6a, right). For growth temperatures below 230°C, the particles in the ink appeared large enough to form thick films that contain percolation networks between the source and drain electrodes. At a growth temperature of 230°C, the semiconductor film appeared patchy and discontinuous; as a result, no TFTs could be fabricated.

As the growth temperature increased, there were fewer large multicrystalline particles observed in TEM. This is consistent with increased nucleation: a larger number of particle 'seeds' form, and growth is limited by the low concentration of monomers in the reaction solution. The nanocrystals were more uniform in size and their solubility improved; as a result, the films became smoother and more continuous. At 240°C many large particles were still present; by 250°C the particles were relatively uniform in size and well-dispersed. At these temperatures, uniformly smooth films were observed at the device scale using optical microscopy. The nanoscale film morphology was further characterized using atomic force microscopy (AFM) for spin-coated films of In₂O₃ nanocrystals grown at 250°C; the resulting nanocrystal film was ~32 nm thick film with surface roughness of 4 nm_{RMS} (Figure 2.7).

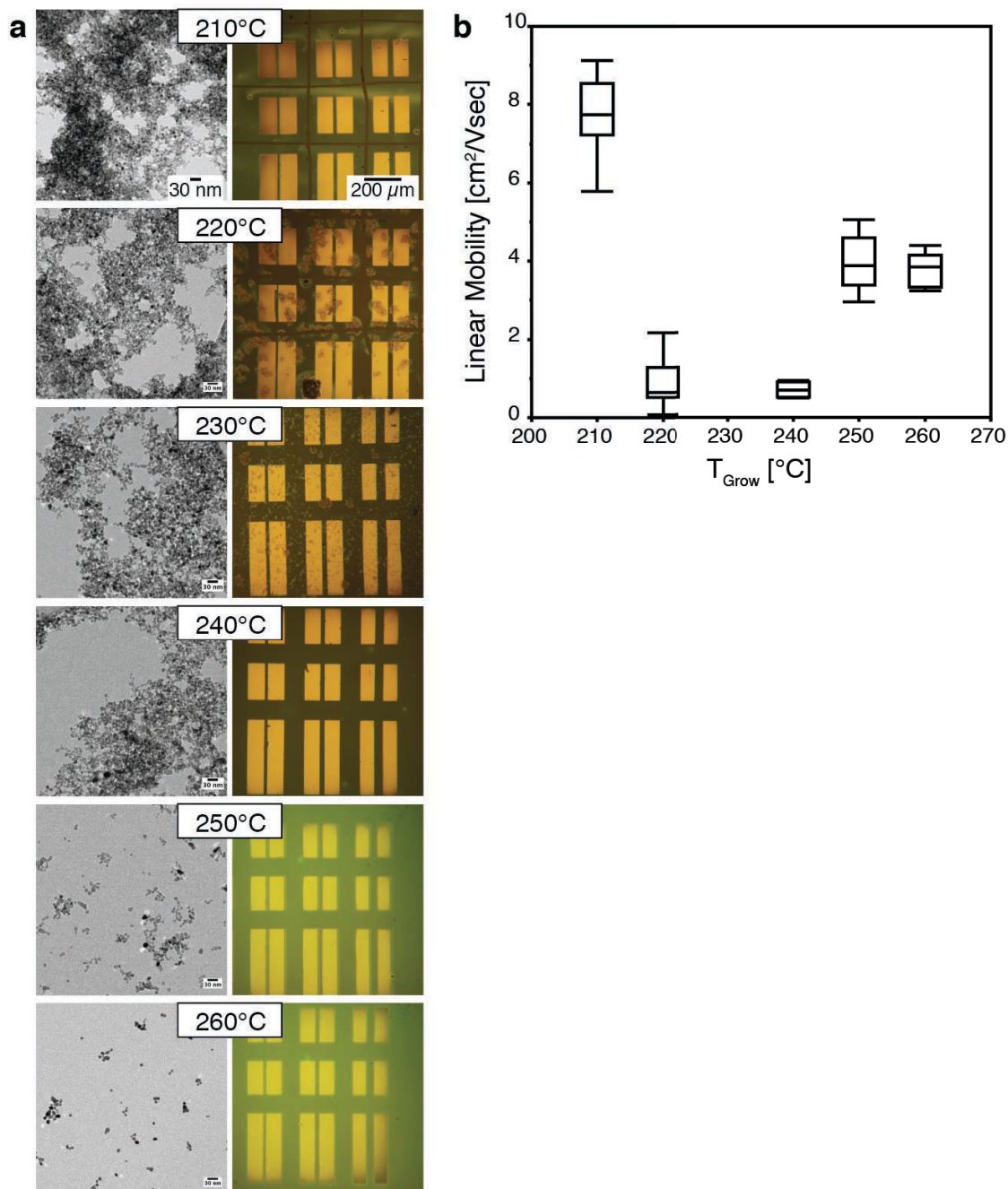


Figure 2.6: Effects of nanocrystal growth temperature.

Effects of growth temperature during synthesis (T_{Grow}) on nanocrystal solubility, film quality, and TFT performance. (a) TEM images of nanocrystals synthesized at temperatures from 210–260°C, and optical microscope images of the corresponding TFT samples. Scale bar = 30 nm for TEM images; scale bar = 200 μm for optical micrographs. (b) Linear field-effect mobility from TFTs fabricated with nanocrystals from each synthesis temperature. Mobility could not be extracted for devices from the $T_{\text{Grow}} = 230^\circ\text{C}$ sample because the film was not continuous, and no working devices could be fabricated.

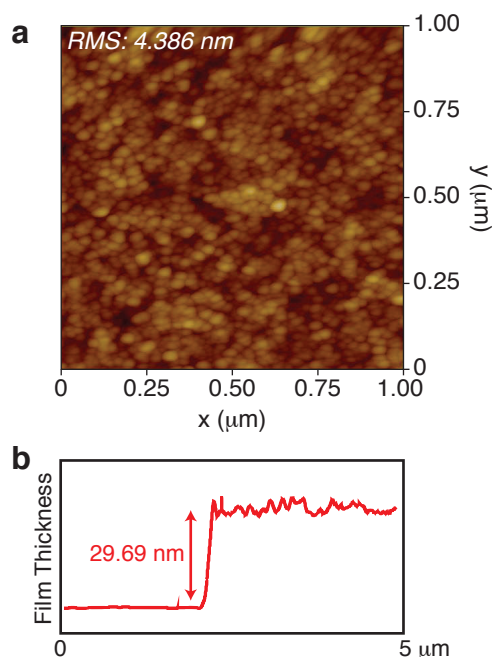


Figure 2.7: Thickness and roughness of In₂O₃ nanocrystal thin films.

In₂O₃ nanocrystal layer in a TFT annealed at 500°C for 1 hour. (a) Surface roughness is 4 nm_{RMS}, and (b) thickness is 30 nm.

Achieving such thin, smooth semiconductor films is critical to maximize TFT performance, and to minimize variation between devices on large-area substrates. Interestingly, the TFT mobility does not vary monotonically with nanocrystal growth temperature (Figure 2.6b). At lower growth temperatures, the indium oxide nanocrystal synthesis appears to be growth-dominated, so the solution consists of large multicrystalline nanoparticles. Increasing the growth temperature results in a larger number of smaller nanocrystals; this improves solubility and produces thin films that are smoother and more compact. Thus, we hypothesize that as the nanocrystal growth temperature increases, the TFT mobility first drops as the crystallite size shrinks, then it increases as the channel becomes denser and more continuous. In addition, the high mobility of the 210°C sample could be partially attributed to an incomplete precursor-to-monomer reaction, producing a mixture of nanocrystals and intermediate precursor complexes. In this case, nanocrystals would essentially be deposited in a sol-gel, accounting for the higher mobility. This hypothesis also explains the instability of the low growth temperature inks, since sol-gels often rapidly form precipitates. It is also consistent with the fact that the reaction is run below or near the temperature where a color change is observed (215°C), which most likely indicates the monomer formation or a nucleation event. Because all devices underwent a post-deposition anneal at 500°C for 1 hour, residual ligands in the film are not likely to be a dominant factor in the mobility variation.

The best combination of film morphology and TFT mobility is achieved with a nanocrystal growth temperature of 250°C. No further improvements in solubility or TFT performance were observed by raising the growth temperature above 250°C. Though the

highest mobility was actually achieved using particles grown at only 210°C, it is important to note that this result is ultimately undesirable for printed electronics because of the poor ink stability and film uniformity. Aggregation of the nanocrystals in the ink would prohibit its use in ink-jet and gravure printing applications due to nozzle clogging and uncontrollable printing due to changing fluid properties. Film quality is particularly problematic in fully printed devices, because the deleterious effects of film roughness are compounded as additional layers are deposited.

2.3.3 Characterization of nanocrystals and TFTs using optimized synthesis

Having determined that 250°C was the optimal nanocrystal growth temperature for solution-processed In_2O_3 nanocrystal TFTs, the material synthesized under this condition was further characterized. A bright-field TEM image of the indium oxide nanocrystals obtained from a standard synthesis showed roughly spheroidal particles (Figure 2.8a) that are easily dispersed in nonpolar organic solvents. Statistics collected from >100 individual particles indicate that the average diameter of the as-prepared particles is $9.3 \text{ nm} \pm 2.5 \text{ nm}$ (Figure 2.8b). High-resolution TEM (Figure 2.8c) confirmed the single-crystalline nature of the particles as prepared; the spacing between lattice fringes in the phase-contrast image was 2.92 \AA , corresponding to the (222) interplanar spacing of bulk cubic In_2O_3 (PDF no. 00-006-0416).

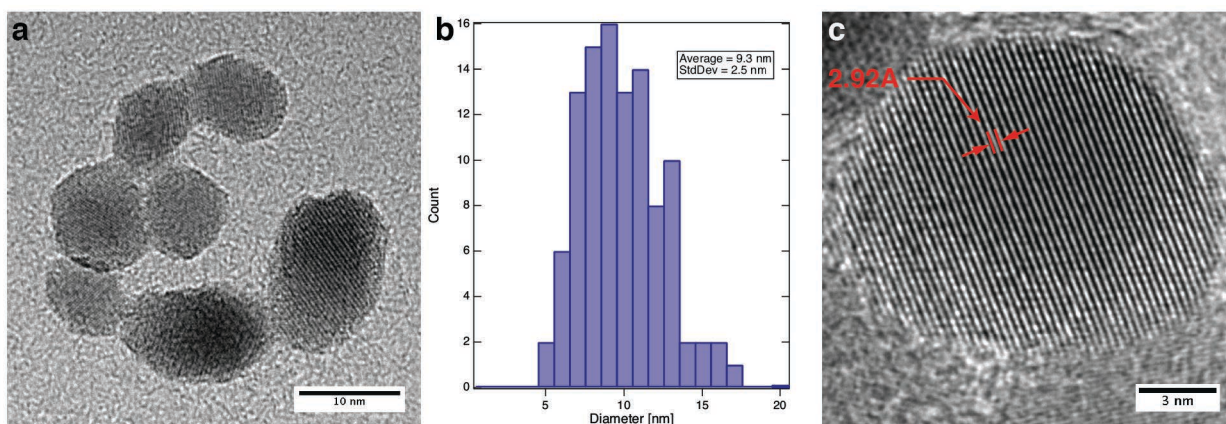


Figure 2.8: TEM images of In_2O_3 nanocrystals.

(a) Transmission electron micrograph (TEM) of In_2O_3 nanocrystals from the air-free reaction of indium (III) acetylacetonate and oleylamine at 250°C. Scale bar = 10 nm. (b) Histogram of nanocrystal diameter calculated from >100 individual particles. (c) High-resolution TEM confirming the single-crystalline nature of the particles; fringe spacing of 2.92 \AA corresponds to the d_{222} interplanar spacing of bulk cubic In_2O_3 . Scale bar = 3 nm.

The x-ray diffraction (XRD) pattern for the nanocrystals as-deposited (dried in air at room temperature) shown in Figure 2.9 is well matched to that of bulk cubic In_2O_3 (PDF no. 00-006-0416). The average crystallite size calculated from the Scherrer equation using the full-width at half-maximum (fwhm) of the most intense reflection peak ($2\theta = 30.5^\circ$) is 10 nm. The agreement of the particle size from TEM and the crystallite size from XRD further confirms the single-crystalline nature of the In_2O_3 nanocrystals produced using this synthetic

procedure, suggesting that a reaction temperature of 250°C is sufficiently high to allow rearrangement of atoms during nanocrystal growth.

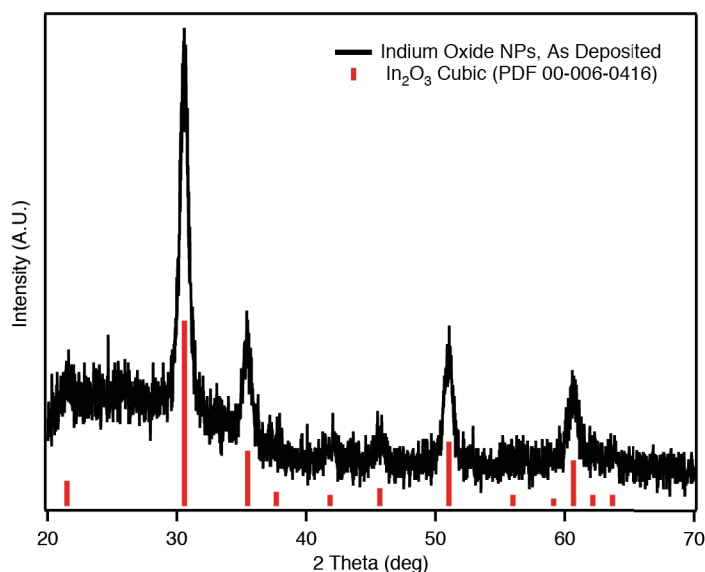


Figure 2.9: XRD of In₂O₃ nanocrystals, as deposited (no anneal).

X-ray diffraction pattern of indium oxide nanoparticles as deposited from solution (dried in air at room temperature), and standard bulk cubic In₂O₃ reference spectrum (PDF no. 00-006-0416).

The transfer characteristics and output characteristics of a typical In₂O₃ nanocrystal TFT fabricated at the optimal conditions are shown in Figure 2.10, along with a schematic drawing of the device structure. Metal-oxide semiconductors are known to exhibit higher performance when they incorporate a gate dielectric material with a high dielectric constant, particularly ZrO₂; thus, a 41 nm layer of ZrO₂ deposited by ALD ($\kappa \sim 21$) was employed and, as expected, the TFT performance exceeds the results shown in Figure 2.6 for the same nanocrystal synthesis protocol. This In₂O₃/high- κ device exhibits an electron mobility in the linear regime of 10.9 cm²/Vs, with an I_{ON}/I_{MIN} current ratio greater than 10⁶ and turn-on voltage of -1.5 V. The minimal hysteresis, steep subthreshold swing of 0.3V/decade, and good suppression of carriers in the off-state are evidence of a high quality semiconductor film with low trap density. Clear saturation is evident in the output characteristics, indicating good electrostatic control. These devices exhibit a carrier mobility an order of magnitude higher than any previously reported In₂O₃ nanocrystal TFT [37], [38], and comparable to other solution-processed In₂O₃ TFTs [15], [16].

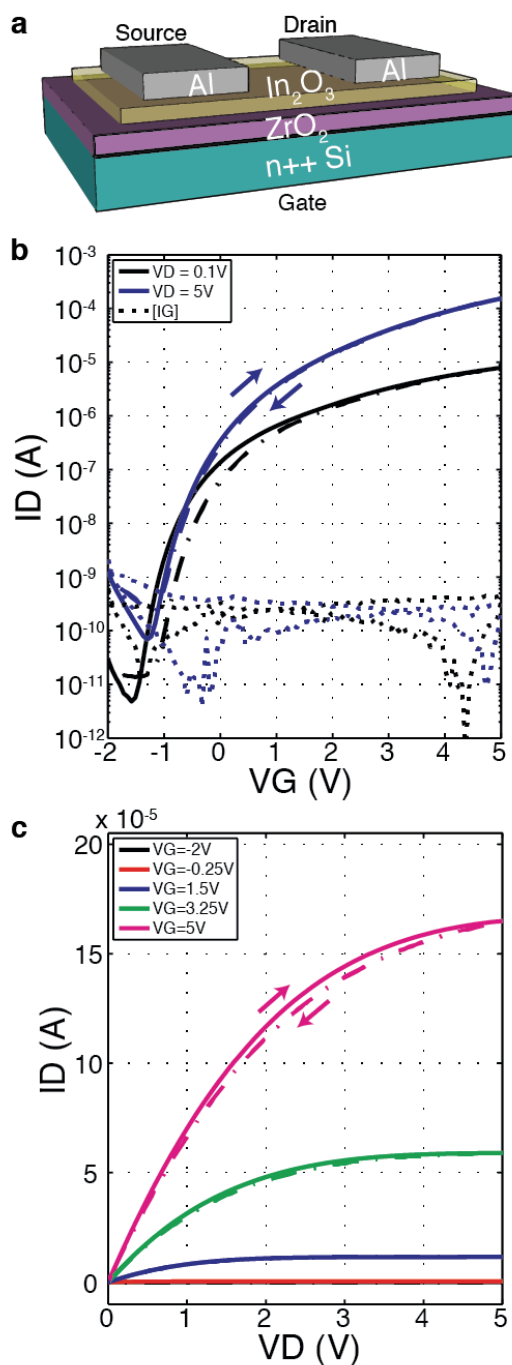


Figure 2.10: Transfer and output characteristics of In₂O₃ nanocrystal TFTs. (a) Structure of the back-gate, top-contact In₂O₃ nanocrystal TFT. (b) Transfer characteristics and (c) output characteristics of a TFT utilizing the In₂O₃ nanocrystals from a typical synthesis ($T_{\text{Grow}} = 250^{\circ}\text{C}$ following a vacuum degassing step) as the channel layer, after a 500°C post-deposition anneal in oxygen.

2.4 Multifactorial Analysis of TFT Processing Conditions

It is clear that the performance of solution-processed metal-oxide TFTs is a complex function of many variables, such as the ink formulation, deposition method, annealing temperature, annealing ambient, substrate, and gate dielectric material, among others. Given this large number of factors, a multifactorial design of experiments with statistical analysis of input factors and output responses is more efficient than the typical “one variable at a time” method to understand the most important aspects of the material synthesis and device fabrication. Here, a full factorial experimental design is employed to study the impact of fabrication and processing conditions on the performance of the In_2O_3 nanocrystal TFTs presented in the previous section. Input factors and output responses are modeled to determine the most statistically significant effects, which can provide guidance for future device optimization. The morphology of the In_2O_3 films was investigated to elucidate the physical mechanisms responsible for the variation in TFT performance. Finally, a method is presented that more fairly compares the mobility of metal-oxide TFTs fabricated on different gate dielectrics by considering the effective transverse electric field in the channel region.

2.4.1 Design of experiments

A multifactorial experimental design was used to investigate the effects of fabrication conditions on the performance of solution-processed In_2O_3 nanocrystal TFTs. Previous screening experiments highlighted the impact of two key variables on the performance of solution-processed metal oxide TFTs, namely (1) annealing temperature and (2) the choice of gate dielectric material. Higher annealing temperatures result in better device performance, and some high- κ gate dielectrics have been shown to provide an additional mobility boost in metal oxide semiconductors [9], [12], [13], [44], [45]. Additionally, previous reports of metal oxide films deposited using gas-phase deposition techniques showed that the oxygen partial-pressure during deposition had a dramatic impact on the carrier concentration, presumably because of its impact on the oxygen vacancy concentration [46]. The presence of oxygen during the annealing process might produce similar effects in solution-processed metal oxide devices, so it was included as a third input variable in the experimental design.

Because these experimental factors may have compounded effects on the device performance (for example, the *combination* of annealing temperature and annealing ambient might have a stronger effect than either variable alone), a full factorial experimental design was selected. A full factorial design contains all possible combinations of a set of factors, making it the most fool-proof design approach but also the most costly in terms of experimental resources. In a full factorial design, none of the main effects or interaction effects are confounded with one another; thus it is a good choice when the interaction effects are likely to be significant, and enables the experimenter greater certainty of the true impacts of processing conditions on device performance. For further details on experimental design and analysis techniques, the text by Box, Hunter, and Hunter [47] is an excellent reference.

In general, the goal of the experiment is to determine a model for the observable output variable (the response, y) that can be defined as a function of the input variables (the factors x_1, x_2 , etc.). The prediction equation is typically a linear combination of x values such as

$$y = \beta_0 + \beta_1 x_1 + \cdots + \beta_k x_k + \varepsilon \quad (\text{Equation 2-1})$$

where the coefficients, β , are the values to be estimated in the model and ε is an error term. Therefore, selecting appropriate bounds for each input factor not only ensures that the experiment provides technologically relevant results, but it also improves the likelihood that the responses can be accurately modeled. With this in mind, an experimental design space was defined for each of the three factors to be examined: annealing temperature, gate dielectric material, and annealing ambient.

The annealing temperature range was chosen based on thermogravimetric analysis (TGA) and differential scanning calorimetry (DSC) of the indium oxide nanocrystals. A nanocrystal sample was dried in air at room temperature, then the temperature was ramped from 20°C to 500°C at a rate of 5°C/min; the mass loss and heat flow are plotted in Figure 2.11. The most significant mass loss and heat flow occurred in the range of 200°C-500°C. The boiling point of the oleylamine ligand is between 350-365°C depending on purity, so a significant change in film composition is expected near that temperature.. Three annealing temperatures were selected – 200°C, 350°C, and 500°C – to probe the changes in the nanocrystal film in this temperature range, and the subsequent effect on the TFT performance. This is also technologically relevant: 200°C is near the temperature limit for most plastic substrates, and setting the maximum processing temperature to 500°C ensures compatibility with glass substrates for display applications. A tube furnace was selected to perform the anneals (rather than a standard laboratory hotplate) because it could reach 500°C more reliably and with better uniformity than a hotplate, and because of the capability to control the annealing environment.

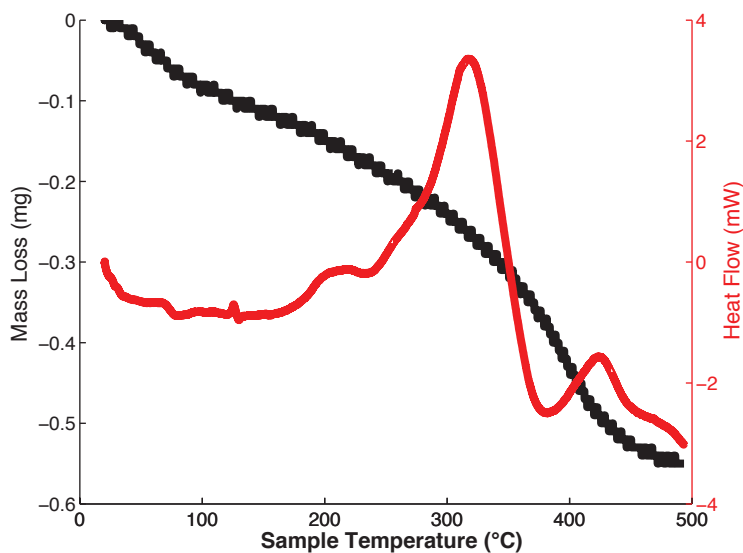


Figure 2.11: TGA and DSC of In_2O_3 nanocrystals.

Most significant mass loss occurs below 450°C , helping to set the bounds for the annealing temperature.

The gate dielectric materials were chosen to cover a range of dielectric constants, and specifically to include ZrO_2 . Many groups have reported that metal oxide semiconductors exhibit higher field-effect mobility when fabricated on a high- κ gate dielectric [9], [12], [13], [44], [45], but the mechanism of the improved transport is not well understood. Three dielectric materials were selected: SiO_2 , Al_2O_3 , and ZrO_2 ($\kappa = 3.9$, 7, and 21, respectively). Silicon dioxide was chosen for ease and convenience of testing, and as a consistent benchmark to other reports in literature. Sol-gel ZrO_2 films have demonstrated substantial improvements in TFT performance of SiO_2 [9], thus ZrO_2 was included as the upper bound for these experiments. Aluminum oxide was chosen as the mid-range gate dielectric because of its ease of deposition; Al_2O_3 is often considered the model system for ALD [48]. Deposition methods were selected that could provide highly uniform dielectric layers to reduce experimental error from material variations. A standard dry oxidation of silicon was used to grow thermal SiO_2 , and films of Al_2O_3 and ZrO_2 were deposited by ALD.

Finally, the ambient annealing environments were selected to compare an oxygen-rich environment with a standard air environment. Annealing in air is the simplest option from a manufacturing point of view, and would provide the lowest fabrication cost for solution-processed devices on a large scale. It is also an important benchmark, since solution-processed devices reported in literature are typically annealed in air. In gas-phase deposition of metal oxides, however, the oxygen partial-pressure during deposition had a dramatic impact on the carrier concentration [46]. Thus, oxygen was chosen as an alternate annealing ambient. Only two levels were selected for this factor due to limitations in the gas mixing capabilities of the tube furnace used for device annealing.

The experimental design space is shown schematically in Figure 2.12. A full factorial design including (3 annealing temperatures)*(3 gate dielectric materials)*(2 annealing

ambients) resulted in a total of 18 experimental trials. JMP Pro 11 statistical software was used for experimental design and statistical analysis.

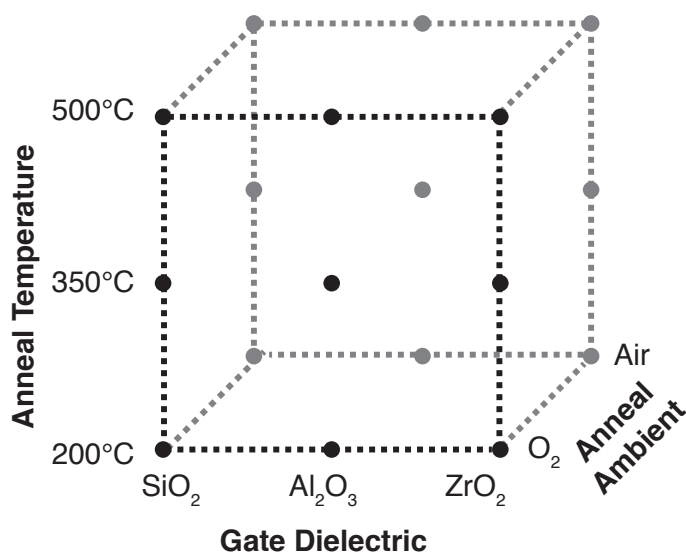


Figure 2.12: Experimental design space for In₂O₃ TFT processing conditions.
The multifactorial experimental design space, illustrating the processing condition variables examined for indium oxide nanocrystal TFTs.

2.4.2 Experimental details

Bottom-gate/top-contact TFT test structures were fabricated using In₂O₃ nanocrystals as the active channel material following the method described in Section 2.2.2. The standard fabrication process was varied according to the experimental trials shown in Figure 2.12. The gate dielectric deposited onto the silicon wafers was either 100 nm thermally grown SiO₂, 41 nm of Al₂O₃ deposited by ALD, or 41 nm of ZrO₂ deposited by ALD. Following deposition of the nanocrystals onto the gate dielectric, the films were annealed for 1 hour in a tube furnace at 200°C, 350°C, or 500°C in either oxygen or air. A schematic and a TEM cross-section image of a device are shown in Figure 2.4.

The crystalline structure and crystallite size in the annealed nanocrystal films were characterized using glancing-incidence x-ray diffraction (GIXD). In the glancing-incidence geometry, the angle of incidence of the x-rays is very small (near the critical angle), and thus penetration depth into the sample is on the order of nanometers. This surface-sensitive diffraction method is ideal for characterizing very thin films with negligible contribution from the crystalline substrate. Even in the glancing-incidence geometry, many thin-film materials with nanometer-sized crystallites are difficult to characterize using standard laboratory diffractometers due to low signal-to-noise ratios. In this work, such limitations were overcome by leveraging the high photon flux of synchrotron radiation. GIXD data were obtained using beamline 1-5 at the Stanford Synchrotron Radiation Lightsource (SSRL) with an x-ray energy of 8 keV, an incident angle of 0.3° and a MAR345 image plate detector. The

geometry of the GIXD measurement is shown in Figure 2.13. The incident x-ray beam k_0 strikes the surface at a very small angle $\omega = 0.3^\circ$. The film of nanocrystals produces multiple scattered beams, shown here as k_1 and k_2 . Diffraction data were analyzed using WxDiff, and open source diffraction image processing and data analysis software package available from SSRL. The data are first converted from the raw data (pixels) on the detector to a spherical projection of the scattered beams (Figure 2.14a); the radii of the concentric rings correspond to the q -spacing of the scattered beam from a randomly oriented film of crystallites. The spherical projection data can be plotted as the intensity of the scattered beam for a given q -spacing vs the angular position, χ (Figure 2.14b). Summing the intensity values over χ produces the traditional diffraction plot of intensity vs. q -spacing (Figure 2.14c). The diffraction data in this work was analyzed as described, and will be presented as a standard diffraction plot.

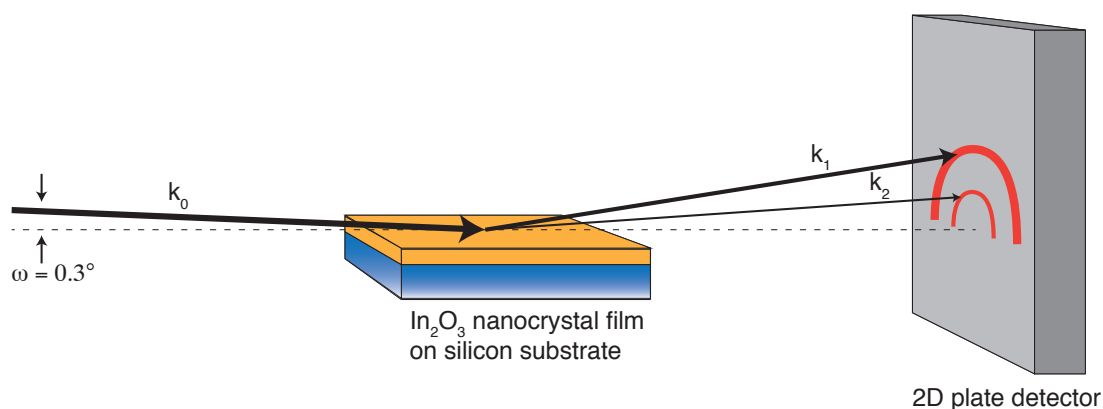


Figure 2.13: Geometry of GIXD measurements.

The incident x-ray beam k_0 strikes the surface at a very small angle ω . A film of randomly oriented nanocrystals produces multiple scattered beams, shown here as k_1 and k_2 .

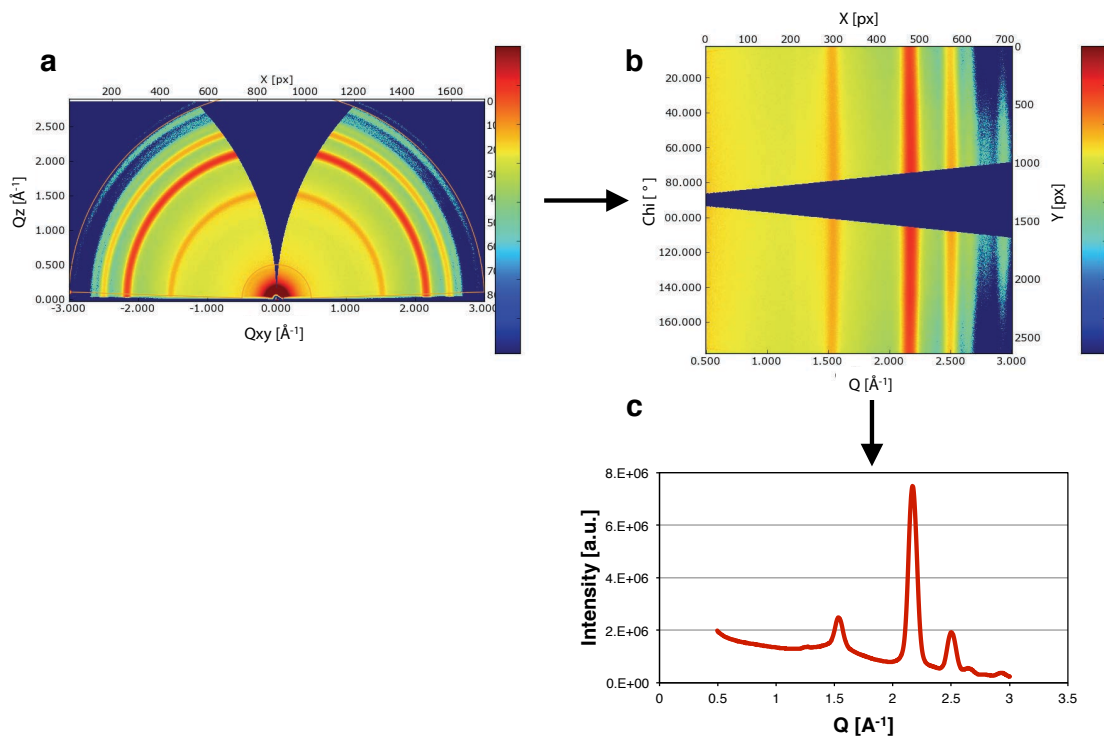


Figure 2.14: Analysis of GIXD data collected from 2D detector plate.

GIXD data are collected using a flat image detector plate. Diffracted beams from a non-textured sample result in concentric rings with a diameter that corresponds to the d-spacing of the crystallites in the sample. Data from the flat plate detector can be converted (a, b) and summed to obtain the traditional diffraction plot (c).

2.4.3 Results and discussion

The In_2O_3 nanocrystal TFTs in this study operate as n-type accumulation mode devices. Transistor parameters were extracted from the measured current-voltage curves including field-effect mobility, subthreshold swing, $I_{\text{ON}}/I_{\text{OFF}}$ current ratio, turn-on voltage, and hysteresis. Multifactorial analysis of In_2O_3 nanocrystal TFTs identifies which factors and interactions had a statistically significant effect on each TFT parameter. The results of the effect test are shown for mobility, $I_{\text{ON}}/I_{\text{OFF}}$ ratio, and swing in Figure 2.15; the p -values give the probability that the effect is zero, so smaller p -values indicate more certainty that an effect is significant. Overall, the gate dielectric material, D , along with its interaction effects $D*T$ and $D*A$, had the most significant impact on the TFT performance parameters. The annealing temperature, T , also significantly affected the mobility and the $I_{\text{ON}}/I_{\text{OFF}}$ ratio ($p < 0.0001$). The annealing ambient, A , affected the $I_{\text{ON}}/I_{\text{OFF}}$ ratio and the subthreshold swing ($p < 0.0001$), but as a main effect it did not significantly impact mobility. The *interaction* of the annealing ambient with the other factors, however, amplified its effect on mobility, such that $D*A$ and $T*A$ were both significant effects ($p = 0.03$ and 0.002 , respectively). The ability to identify the impact of these interaction effects on the TFT performance characteristics highlights the benefits of a properly designed multifactorial experiment, compared to a one-variable-at-a-time experimental approach.

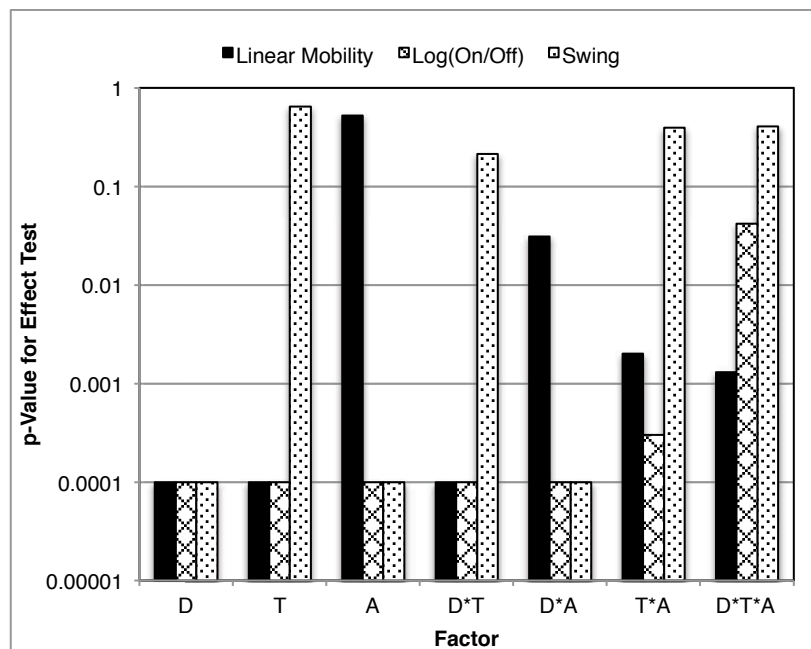


Figure 2.15: Effect test results for experimental input factors.

Results of the statistical effect tests for each main factor, second order, and third order interaction on TFT mobility, I_{ON}/I_{OFF} current ratio, and subthreshold swing. D = gate dielectric, T = anneal temperature, A = anneal ambient; an asterisk (*) denotes interaction effects. Smaller p -values indicate a more statistically significant effect.

These results are also observed in the summarized TFT parameters shown in Figure 2.16 and the summary of linear mobility values listed in Table 2–1. In addition to mobility, I_{ON}/I_{OFF} ratio, and swing, Figure 2.16 also includes the turn-on voltage and the hysteresis in the I_D - V_G curves (defined as $V_{ON,Reverse} - V_{ON,Forward}$) for each experimental trial. Turn-on voltage and hysteresis were not included in the effect test analysis due to a lack of fit in the model. Devices made with high- κ gate oxide materials exhibited higher mobility, better subthreshold swing, a larger I_{ON}/I_{OFF} ratio, a turn-on voltage closer to zero, and reduced hysteresis. Increasing the annealing temperature from 200°C to 500°C increased the mobility by roughly two orders of magnitude and, with the resulting increase in on-current, boosted the I_{ON}/I_{OFF} ratio. The notable exception to this trend is on SiO_2 : the mobility and on-current increased, but a negative shift in the turn-on voltage with increased annealing temperatures (seen clearly in Figure 2.17) and the failure to fully turn off the devices annealed in oxygen resulted in a reduction in the I_{ON}/I_{OFF} ratio.

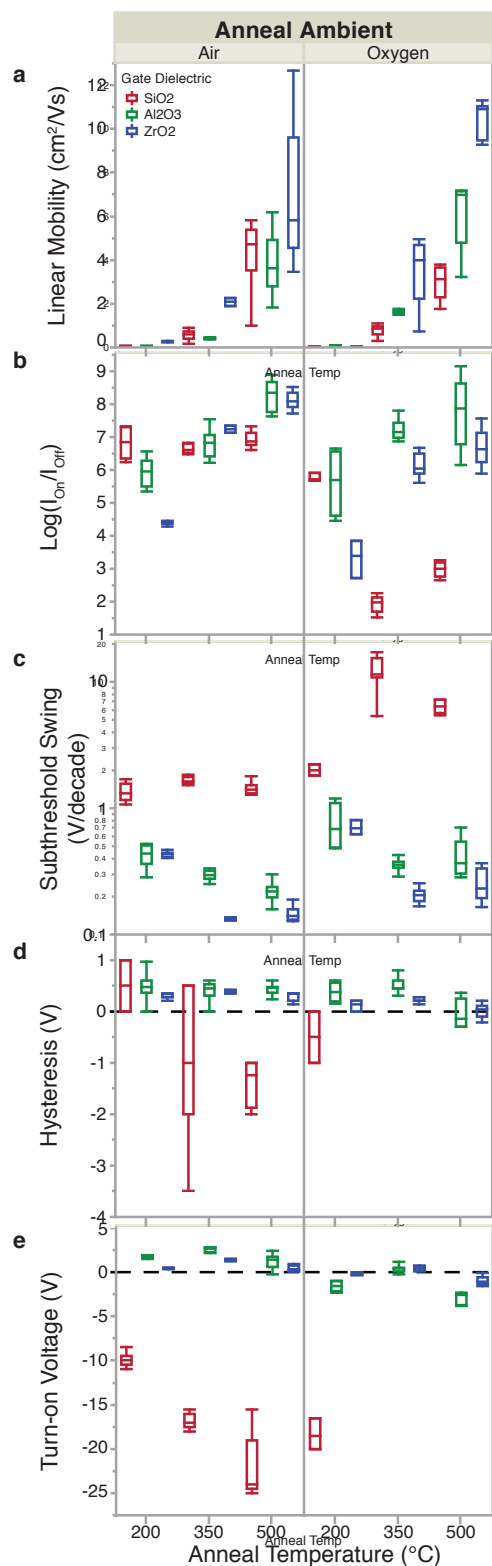


Figure 2.16: In₂O₃ nanocrystal TFT performance metrics vs processing conditions. Multifactorial analysis of the effects of processing conditions and gate dielectric material on TFT performance. All devices have W/L = 200 μm / 40 μm.

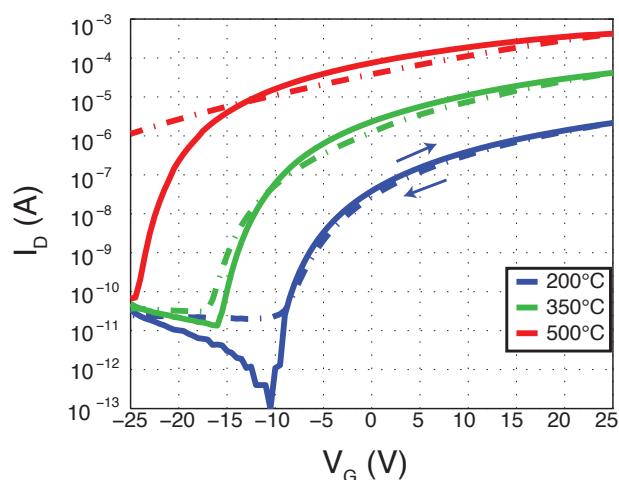


Figure 2.17: Transfer curves for In_2O_3 TFTs vs anneal temperature.

Representative transfer curves of indium oxide nanocrystal TFTs on SiO_2 gate dielectric annealed in air at 200°C, 350°C, and 500°C, illustrating the negative shift in the turn-on voltage at higher annealing temperatures. All curves are measured in the saturation regime ($V_D = 25\text{V}$).

Gate Dielectric	Anneal Temperature	μ_{Lin} (cm^2/Vs) (Ambient = O_2)	μ_{Lin} (cm^2/Vs) (Ambient = Air)
SiO_2	200°C	0.02	0.05
SiO_2	350°C	0.8	0.6
SiO_2	500°C	3.0	4.3
Al_2O_3	200°C	0.06	0.05
Al_2O_3	350°C	1.6	0.4
Al_2O_3	500°C	6.2	3.9
ZrO_2	200°C	0.3	0.02
ZrO_2	350°C	3.3	2.1
ZrO_2	500°C	10.5	7.2

Table 2–1: Summary of In_2O_3 TFT linear mobility values.

Summary of the linear mobility values for In_2O_3 nanocrystal TFTs fabricated using each condition of the experimental design illustrated in Figure 2.12.

Table 2–1 lists the average linear mobility values at each experimental condition. The highest performance on each gate dielectric was achieved using a 500°C anneal in oxygen, with the ZrO_2 gate dielectric demonstrating a $\sim 3.5\text{x}$ increase in mobility over SiO_2 . The results using ZrO_2 are particularly promising because even at a moderate annealing temperature of 200°C in oxygen, the average mobility was $0.3 \text{ cm}^2/\text{Vs}$. Representative transfer curves and output characteristics after a 500°C oxygen anneal are shown in Figure

2.18 for each of three gate dielectric materials. The best conditions found within this experimental space (ZrO_2 gate dielectric, 500°C anneal in oxygen) yielded devices with an average mobility of $10.5 \text{ cm}^2/\text{Vs}$, $I_{\text{ON}}/I_{\text{OFF}}$ ratio of $>10^6$, subthreshold swing of 0.25 V/decade , and a turn-on voltage of -1 V with negligible hysteresis. The steep slope, lack of hysteresis, and clear saturation in the output curves all demonstrate excellent electrostatic control of the In_2O_3 nanocrystal channel and suppression of carriers in the off state, which is a critical requirement for display applications to achieve fully saturated black pixels. The high $I_{\text{ON}}/I_{\text{OFF}}$ coupled with the high mobility and good swing thus make these excellent candidates for use as pixel transistors.

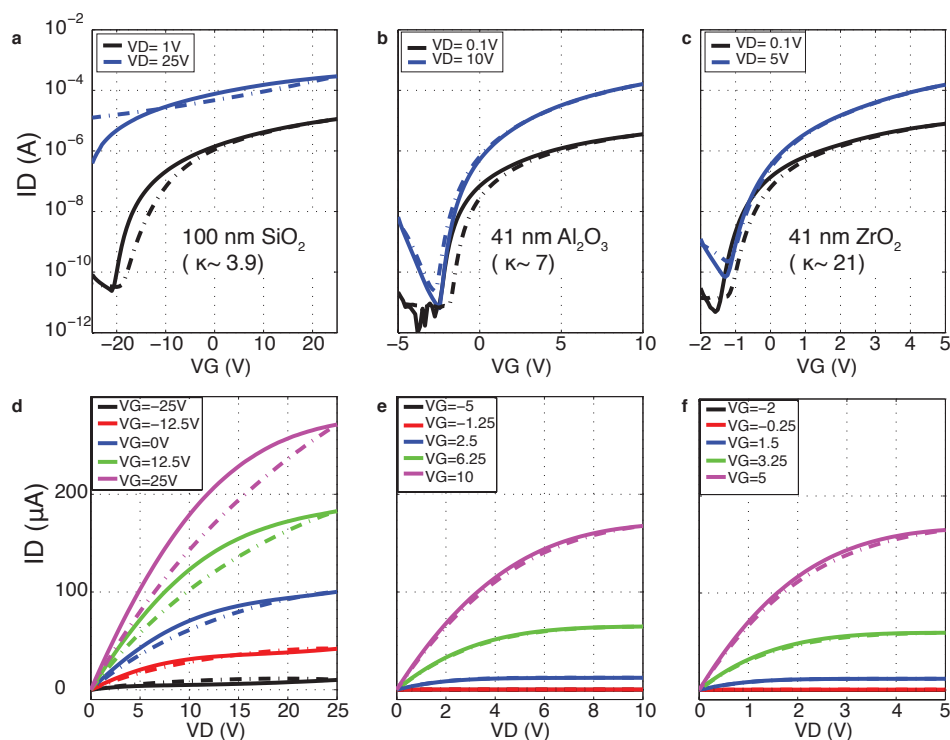


Figure 2.18: Transfer and output curves for In_2O_3 TFTs vs gate dielectric.

Representative transfer and output curves of indium oxide nanocrystal TFTs annealed for 1hr at 500°C in oxygen on three gate dielectric materials: (a, d) SiO_2 , (b, e) Al_2O_3 , and (c, f) ZrO_2 .

Although all the annealing conditions in this experiment were compatible with all major classes of display glass, improving the performance of the devices at the lower annealing temperatures is desirable to enable the use of low-cost plastic substrates. Understanding the film transformations during the annealing is an important step towards reducing the maximum processing temperature. One possible explanation for improved transport at higher temperatures is crystallite growth in the channel, but, interestingly, this is not the case in these devices. To investigate the crystal structure of the annealed In_2O_3 films, x-ray diffraction patterns were collected using a synchrotron radiation light source in glancing-incidence geometry. The average crystallite size was calculated from the full-width-at-half-maximum (fwhm) of the most intense reflection peak in the glancing-incidence x-ray diffraction (GIXD) spectra using the Scherrer equation.

GIXD spectra for the In_2O_3 nanocrystals as-deposited and for each annealing condition are shown in Figure 2.19. Despite dramatic differences in TFT performance, the average crystallite size in the In_2O_3 film does not change after annealing, nor is there significant densification that occurs in the film. These data indicate that transport in the In_2O_3 nanocrystal devices is not limited by the crystallinity. From the standpoint of reducing the processing temperature without sacrificing performance, this is a promising result: further crystallization is not necessary for good transport, so future experiments can focus instead on modifications to the nanocrystal ligands and surfaces that will promote efficient removal of ligand residue at low temperatures.

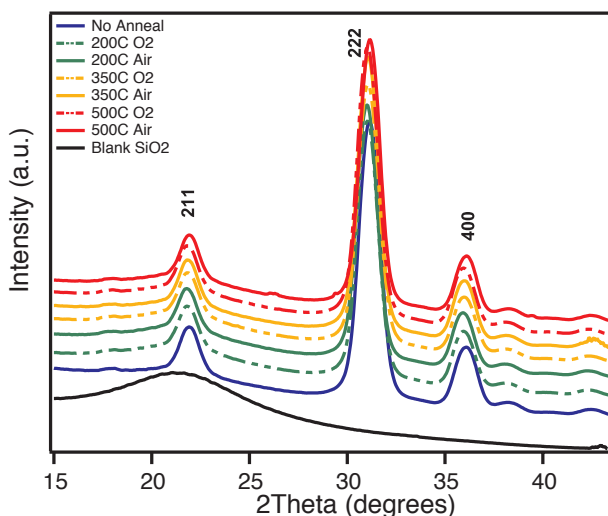


Figure 2.19: GIXD of In_2O_3 nanocrystals vs anneal condition.

Glancing-incidence x-ray diffraction spectra of indium oxide nanocrystal thin films as-deposited on SiO_2 , and with various annealing conditions: ambient = {air, oxygen}, temperature = {200°C, 350°C, 500°C}.

It has been widely reported in literature that metal oxide semiconductor TFTs exhibit higher mobility when used with high- κ gate dielectrics. Various theories have been proposed to explain the boost in mobility, such as an increase in carrier concentration that fills localized states and allows band-like transport [9], reduced trap density at the semiconductor-dielectric interface [12], [44], or defect relaxation and suppression of free carriers resulting from diffusion of material from the gate dielectric to the semiconductor [45]. Here, TFTs fabricated with the ZrO_2 gate dielectric exhibited $\sim 3.5\times$ higher mobility, steeper subthreshold slope, reduced operating voltage, and reduced hysteresis when compared to a device fabricated on SiO_2 under the same conditions. However, for a given annealing condition, there was no notable difference in the GIXD spectra on different gate dielectrics and no change in average crystallite size in the In_2O_3 film (Figure 2.20). Thus the mobility boost on ZrO_2 over SiO_2 cannot be attributed to differences in the TFT channel such as grain size or orientation. This conclusion was further confirmed by examining a cross-section of the semiconductor-dielectric interface in high-resolution TEM, which showed no difference in morphology between SiO_2 and ZrO_2 devices.

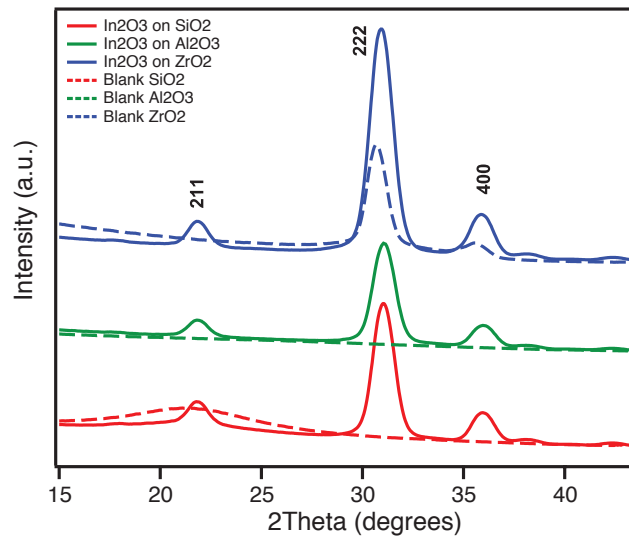


Figure 2.20: GIXD of In₂O₃ nanocrystals vs gate dielectric. Glancing-incidence x-ray diffraction spectra of indium oxide nanocrystal thin films on SiO₂, Al₂O₃, and ZrO₂ gate dielectrics; all devices shown here were annealed for 1hr at 500°C in oxygen.

An alternative method of comparing the performance of TFTs fabricated with different gate dielectrics is to examine the field-effect mobility as a function of the transverse electric field felt by an electron in the channel. This ensures a fair comparison of mobility, normalized for gate capacitance and turn-on voltage for different devices. This idea is similar to the universal mobility curves developed for silicon MOSFETs, where the mobility is impacted by the physical parameters of the device [49]. Since metal-oxide TFTs operate in accumulation mode, we define the effective transverse electric field in the channel and the accumulation charge density, respectively, as

$$E_{eff} = \frac{Q_{acc}}{\epsilon_{semi}} \quad (\text{Equation 2-2})$$

and

$$Q_{acc} = C_{ox}(V_{GS} - V_{FB}), \quad (\text{Equation 2-3})$$

where ϵ_{semi} is the relative permittivity of the semiconductor, C_{ox} is the gate oxide capacitance per unit area, V_{GS} is the gate voltage, and V_{FB} is the flat-band voltage. The flat-band voltage is defined as the onset of accumulation in the channel, and we assume it is approximately equal to the turn-on voltage, V_{ON} , which can be easily and accurately obtained from the TFT transfer curves. Substituting Equation 2-3 into Equation 2-2 and replacing V_{FB} with V_{ON} , we have

$$E_{eff} = \frac{C_{ox}(V_{GS} - V_{ON})}{\epsilon_{semi}}. \quad (\text{Equation 2-4})$$

In Figure 2.21, the field-effect mobility in the linear region is plotted against the effective transverse field in Equation 2-4 for TFTs made with SiO₂, Al₂O₃, and ZrO₂. For any given

transverse electric field felt by an electron in the In_2O_3 nanocrystal channel, the mobility is higher for high- κ gate dielectrics Al_2O_3 and ZrO_2 than for SiO_2 . While the highest mobilities are achieved by reaching higher transverse fields on ZrO_2 , it is not the sole reason for the mobility improvement on high- κ gate dielectrics.

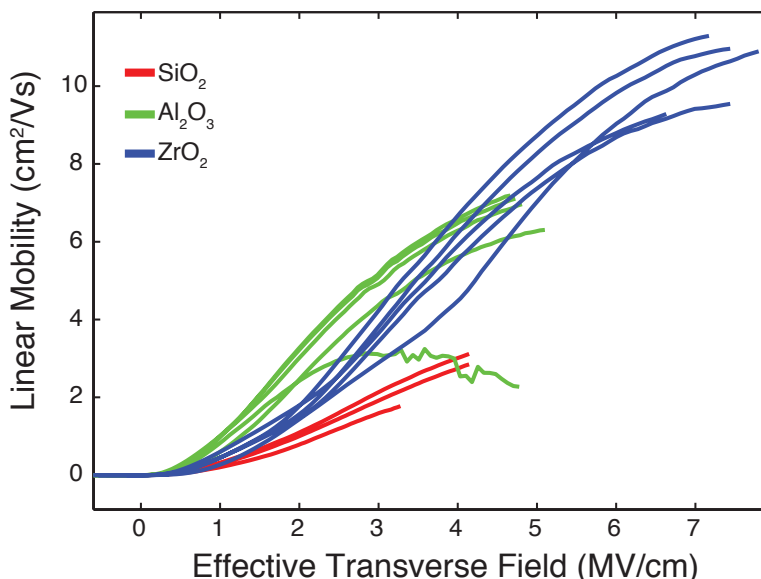


Figure 2.21: Mobility of In_2O_3 TFTs vs the effective electric field in the channel.

Linear mobility vs the effective transverse electric field felt by an electron in the channel for various gate dielectric materials. Multiple devices are plotted for each gate dielectric; all devices shown here were annealed for 1hr at 500°C in oxygen.

Though the phenomenon of increased mobility on high- κ materials has been frequently observed, the mechanism for improved transport is still not well understood. Many groups broadly attribute the increase in mobility to improved interface characteristics, but exploiting this improvement in future device designs requires a better fundamental understanding of the device physics at play. Finding that the improved mobility on high- κ gate dielectrics cannot be fully attributed to higher transverse electric fields motivates further study of these metal oxide/ high- κ systems. This result – especially in combination with the knowledge that the crystalline structure of the channel is not altered by the gate dielectric – calls for an investigation of the density of states in the In_2O_3 nanocrystal channel to elucidate the underlying mechanism for improved electron transport. Conduction in disordered semiconductors is strongly dependent on the density of states in the bandgap, which can be probed using temperature-dependent field-effect conductance measurements. The details of such an experiment (along with other ideas for future studies) is discussed in Chapter 5.

2.5 Conclusions

Metal-oxide semiconductors are poised to displace silicon in the pixel transistors of next-generation displays due to their excellent transparency and their mobility in the amorphous phase. Solution-phase deposition techniques for this family of materials have been intensely studied in recent years, and progress has been made in understanding the complex impacts of fabrication conditions on device performance. In this chapter, In_2O_3 nanocrystal inks were shown to be a promising pathway towards high-performance, air-stable, solution-processed transistors. The nanocrystal TFTs in this work have undergone a post-deposition anneal to remove the surfactants from the nanocrystal surfaces, allowing the particles to form a high-quality semiconductor channel material. The impact of In_2O_3 nanocrystal synthesis conditions and device fabrication conditions on TFT performance was investigated. The most statistically significant factors in device performance were the choice of a high- κ gate dielectric and annealing temperature, with devices fabricated on ZrO_2 and annealed at 500°C in oxygen exhibiting the best performance. Despite a dramatic difference in the transport characteristics, there was no change in the average crystallite size in the channel with different annealing conditions or different gate dielectric materials. Further, even when the effective transverse electric field in the channel is taken into account, the mobility of TFTs fabricated on high- κ dielectrics is higher than the mobility on SiO_2 . These results indicate that the transport in In_2O_3 nanocrystal TFTs is not limited by the crystallinity, and that the mobility boost cannot be attributed strictly to the higher fields achieved with high- κ gate oxides. Further experiments to elucidate the impact of ZrO_2 on the density of states in In_2O_3 will help to identify the mechanisms at work in the transport of these unique systems. Continuing work is needed to reduce the temperature at which the ligands are removed, bringing down the total thermal budget for the device fabrication to potentially enable the use of plastic substrates and leverage low-cost roll-to-roll printing processes.

Chapter 3: Biocompatible Flexible Electronics

In chapter 2, detailed studies of a solution-processed nanocrystal semiconductor were reported, including the material synthesis, characterization, and device fabrication. In this chapter, exciting applications for flexible, biocompatible electronic devices are introduced to motivate the study of biocompatible electronic materials. The biocompatibility requirements of solution-processed electronic materials are then discussed. Progress towards biocompatible and bioresorbable devices is presented, as well as an outline for future studies in this area.

3.1 Motivation: Applications for Biocompatible Electronics

Flexible electronics will enable innovation in biomonitoring and health care applications due to their lightweight, flexible form factor and potential to realize low-cost ubiquitous sensors (Figure 3.1). In the medical arena, “bandage-like” electronic devices manufactured using inexpensive roll-to-roll fabrication techniques could pave the way for single-use disposable sensors to detect tissue wounds, vascularization, oxygenation, and tumors. In this way, point-of-care diagnostics and disease detection could be revolutionized by the introduction of efficient and economical devices that provide objective measurements and analyze results in real time. In addition to the possible applications for medical devices, consumers are beginning to utilize integrated and wearable biofeedback sensors for health and fitness applications. For example, detecting multiple physiological indicators such as heart rate, heart rate variability, and temperature could be used to monitor the physiological signs of stress, enabling in-home care that would allow people to change their behavior to improve their health. Building a “body-area network” of sensors would open the door to these and

many other opportunities for individuals to gather the real-time biological data necessary to efficiently manage their own health and fitness.



Figure 3.1: Potential applications for flexible bio-integrated electronics.

Clockwise from left: concept for Cisco wearable fitness monitoring devices; Medtronic implantable continuous glucose monitoring system for diabetic patients; wearable sensors to detect impact during sports activities; remote biomonitoring for military applications; embedded sensors to study and prevent head injuries in sports (Intel); concept for integration of wearable electronics to control smart homes.

The design of flexible, stretchable electronics for biosensing applications has attracted considerable attention in recent years. This progress has been fueled by advancements in thin film materials and manufacturing methods that have enabled high-performance electronics in biocompatible form factors. Several recent examples of flexible, bio-integrated systems are introduced below. These proof-of-concept studies demonstrate the potential of flexible electronics in biomedical applications, which further underscores the need for biocompatible electronic materials.

To begin, state-of-the-art flexible electronic systems for biomedical applications are reviewed in three key areas: low-cost medical sensors, body-integrated wearable electronics, and energy harvesting. Next, the biocompatibility standards applicable to such devices are introduced. Toxicity tests required by the International Organization of Standardization (ISO) are described, along with special considerations for solution-processed materials. Progress towards high-performance biocompatible devices is discussed, and future studies are proposed that will provide key guidance for developing biocompatible flexible electronic systems.

3.1.1 Low-cost medical sensors

Pulse oximetry measures the pulse rate and arterial blood oxygen saturation using an optoelectronic sensor. Conventional pulse oximeters utilize two light-emitting diodes (LEDs) and a photodetector; light from the LEDs is transmitted through a finger or earlobe and sensed by the photodetector. Applications of currently available pulse oximeters are limited because of the bulky, rigid form factor, and high cost per unit area of traditional inorganic optoelectronics. Lochner, *et al.* [50] developed an all-organic pulse oximeter that uses red

and green organic LEDs (OLEDs) in place of the traditional inorganic red and near-infrared LEDs, as well as an organic photodetector (OPD), illustrated in Figure 3.2. The organic semiconductors used to fabricate the OLEDs and OPD can be solution-processed using low-cost roll-to-roll manufacturing techniques and flexible substrates. The ability to produce low-cost large-area devices makes organic optoelectronics attractive for the fabrication of disposable, wearable medical devices. This study also demonstrated that a flexible OPD that could wrap around a finger had significantly less parasitic short circuit current from ambient light than a flat photodetector. Thus the flexibility of the device not only reduces the cost, but also improves the performance and diversifies the possible sensing locations on the human body.

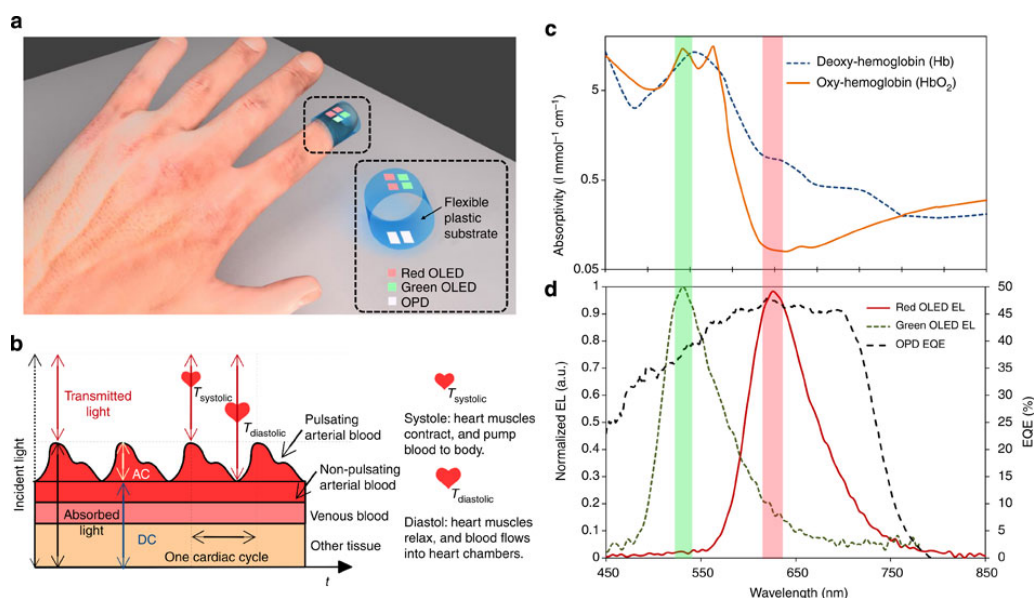


Figure 3.2: Solution-processed optoelectronic sensor for pulse oximetry.

Schematic and optical properties of a flexible pulse oximeter implemented with red and green OLEDs and an organic photodetector, from reference [50].

3.1.2 Body-integrated and wearable electronics

Various medical applications rely on physiological measurements acquired on or through human skin, including electroencephalography (EEG), electrocardiography (ECG), and electromyography (EMG), among others. Bulky electrodes are typically mounted to the skin using straps, clamps, or adhesives, and signals collected from the body are transmitted to an external piece of equipment. A new type of ‘wearable electronic skin’ developed by Kim, *et al.* [51] (shown in Figure 3.3) aims to provide reliable, long-lasting contact to human skin by integrating the electronics in a thin, flexible, wearable patch. Temperature sensors, strain gauges, and ECG/EMG sensors are integrated with a wireless power coil and RF communication capability. The device is laminated onto the skin and held in place by local van der Waals interactions for several days without the need for adhesives. The use of serpentine-shaped wires allow the entire device to stretch and compress with the skin, without compromising the integrity of the electronics. The materials and mechanical properties of these ‘epidermal electronics’ allow the integration of high-performance electronics with the

body in ways that are not achievable with the existing sensing technologies based on traditional rigid electrodes.

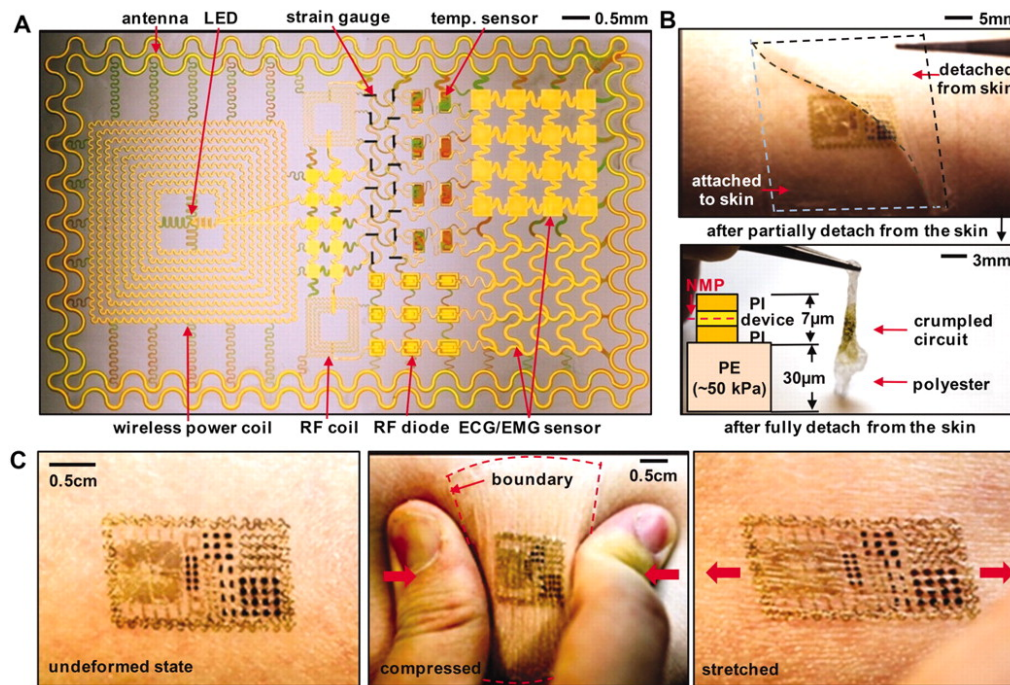


Figure 3.3: Epidermal electronics.

Skin-mountable electronics provide long-lasting, robust contact to the body and perform various physiological measurements (ECG, EMG, temperature, strain, etc); from reference [51].

3.1.3 Energy harvesting and storage

Most wearable and implanted medical devices – including pacemakers, cardioverter defibrillators, and neural stimulators – rely on some type of battery to provide power. This creates a significant challenge for flexible electronics: even when the sensors and electronics themselves are implemented in biocompatible form factors, providing power to the device requires a relatively large, rigid power supply. Recent advances in battery technology have made them thinner and lighter, but the key drawback in using batteries to power long-term medical implants remains: a surgical procedure is required to replace the batteries when the charge is depleted. To circumvent this problem, Dagdeviren *et al.* [52] have developed a flexible thin-film energy harvesting device that is powered by the contraction and relaxation of the heart, lung, and diaphragm. An *in vivo* evaluation demonstrated that when mounted directly onto the organ, the piezoelectric device generates enough energy to power a pacemaker, eliminating the need for a battery. The power output can be easily scaled by stacking multiple devices together; Figure 3.4 shows a 5-layer device. The benefits for implantable devices are clear, but this technology can also benefit external wearable devices such as those described in the previous section. These results open the door for myriad new applications of flexible electronic devices by removing the need for an external power source.

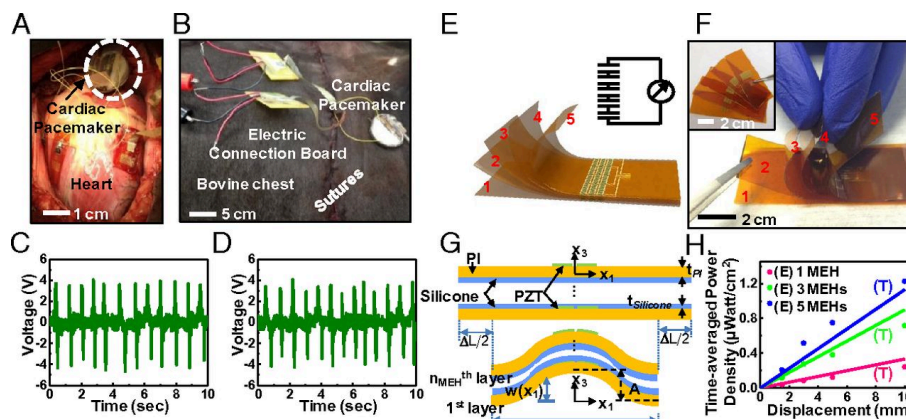


Figure 3.4: Piezoelectric energy harvesting from heart motions.

Flexible piezoelectric devices harvest energy from contractile and relaxation motions of the heart, lung, and diaphragm, from reference [52].

3.2 Biocompatibility Standards

The recent advances outlined in the previous section illustrate the many advantages of flexible electronics – particularly low-cost solution-processed devices – for biomedical devices. Clearly, electronic devices such as those described above that come into regular contact with the body must not cause short- or long-term damage to the user. Thus it is critical that the materials used to fabricate next-generation flexible biosensors are completely biocompatible. In the case of implantable medical devices, the degradation of the materials in the body must also be thoroughly explored to avoid leaching harmful chemicals over time. Further, developing dissolvable, biocompatible materials will be a particularly important step towards the future of implantable “bioresorbable” devices that are designed to disintegrate and be absorbed by the body after their functions are complete to avoid the complications that come with device retrieval.

Biocompatibility is defined by the International Union of Pure and Applied Chemistry (IUPAC) as the “ability to be in contact with a living system without producing an adverse effect” [53]. However, given the complex nature of the human body’s response to foreign substances, it is not sufficient to determine the biocompatibility of an electronic device based solely its constituent materials. For this reason, the biocompatibility of medical devices is evaluated using a series of standards laid out by the International Organization for Standardization (ISO) in ISO 10993, “Biological evaluation of medical devices”. Parts 3 and 5 of ISO 10993 outline the testing standards for genotoxicity (damage to genetic information within a cell, causing mutations) and cytotoxicity (toxic to cells, leading to cell death through necrosis or apoptosis), respectively. These standards are particularly relevant for early stage research developing biocompatible electronics, because promising materials can be screened for any adverse biological effects. Although testing individual materials is not sufficient to demonstrate biocompatibility of the final device, doing so is an important first step leading up to initial animal studies and pre-clinical trials.

3.2.1 Material toxicity tests for ISO 10993 biocompatibility standards

Materials that are promising candidates for solution-processed flexible electronics can be tested according to the ISO 10993 standards for cytotoxicity and genotoxicity, helping to identify the most promising path toward flexible biocompatible electronic devices. The preferred method for determining the cytotoxicity of a material is known as the MTT assay [54]. MTT is an *in vitro* cellular viability test that measures the metabolic activity of cells using spectrophotometric methods. A yellow water-soluble dye, 3-(4,5-dimethylthiazol-2-yl)-2,5-diphenyltetrazolium bromide (MTT), is reduced by mitochondrial enzymes in a healthy, viable cell. The reduction product, formazan, is dark purple in color (Figure 3.5a). After cells are exposed to the material being tested, the MTT is added to the cell culture. Because the biochemical reaction (turning the yellow MTT into the dark purple formazan) is only catalyzed by living cells, measuring the absorbance of the final formazan solution with a spectrophotometer is a quantitative measure of cell viability.

Genotoxicity is evaluated using a set of *in vitro* and *in vivo* tests to detect substances that can cause genetic changes (mutagens). Because of the high cost and the ethical considerations of *in vivo* experiments, initial screening with an *in vitro* test is preferred. The most common starting point is the Ames test [55], which uses the bacteria *Salmonella* to detect point mutations *in vitro*. Certain strains of *Salmonella typhimurium* are chosen because of their high sensitivity to mutagens. The bacteria are cultured in a medium lacking the amino acid histidine, which is a vital substance for the colonization of the salmonella bacteria. In order to colonize, the bacteria must mutate to thrive in the absence of histidine. Thus, the mutagenicity of a substance is proportional to the number of bacteria colonies that develop, which are either grown in a petri dish (a “spot test”, shown in Figure 3.5b) or in a standard multi-well plate (the “fluctuation method”).

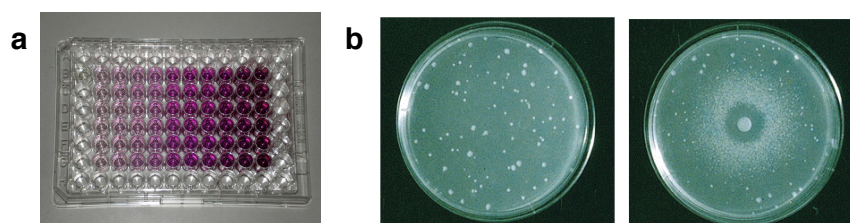


Figure 3.5: *In vitro* tests for material toxicity.

(a) A multi-well plate following a MTT assay for cytotoxicity. Increasing number of cells from left to right results in increasing purple color. (b) Petri dishes showing a “spot test” for genotoxicity using the Ames assay. The left sample is a control, and a mutagenic chemical was placed in the center of the right-hand plate, resulting in more colonization.

3.2.2 Toxicity considerations for solution-processed materials

The materials used in printed electronic devices deserve special consideration in regards to toxicity for two main reasons. First, nanosized materials pose different risks than their bulk counterparts because of their ability to permeate biological tissues. Second, low-temperature processing may result in incomplete conversion from precursors to the target materials,

leading to intermediate chemical complexes and residual precursors or ligands in a thin film. This changes the chemicals to which a user is exposed, and thus investigation is required even for materials that are biocompatible in their bulk form.

3.2.2.1 Particle size affects toxicity at the nanoscale

As discussed previously, many metal oxides that are commonly used to build thin-film electronics are expected to be biocompatible. ZnO, for example, is a frequently-used ingredient in sunscreens and cosmetics. However, the toxicity of ZnO has been shown to increase for nanometer-sized particles. The toxicity of nanomaterials could be higher, for example, because of the catalytic behavior resulting from higher surface energy, increased absorption, altered bioavailability, or easier transport into cells and across barriers (i.e the blood-brain barrier) [56]. This is clearly shown in a study by Hackenberg *et al.* [57], summarized in Figure 3.6. Human nasal mucosa cell viability is unaffected by exposure to ZnO powder (panel **a**), but viability is markedly decreased by exposure to the same concentration of ZnO in nanoparticle form (panel **b**). The genotoxicity (panel **c**) followed the same trend: ZnO powder did not exhibit increased genotoxicity over the control case, but increasing concentrations of ZnO nanoparticles resulted in stronger genotoxic effects. (An increase in the Olive tail moment was an indicator for genotoxic effects.) These data demonstrate that even materials that are “safe” in their bulk form must be studied in the nanometer-size regime.

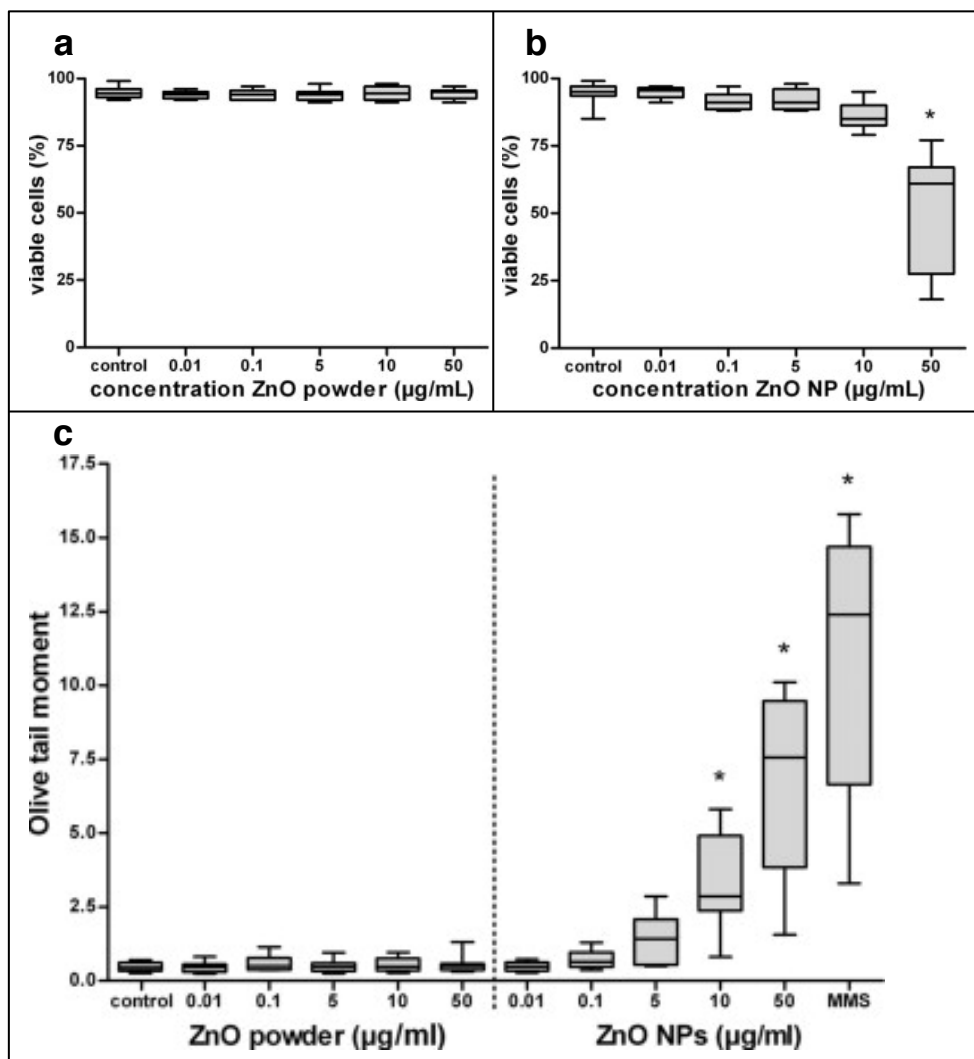


Figure 3.6: Toxicity of ZnO powder vs ZnO nanoparticles.

(a) Cell viability is unaffected by an increasing dose of ZnO powder, but (b) viability decreases with an increasing dose of ZnO nanoparticles. (c) Genotoxicity also increases with increasing dose of ZnO in nanoparticle form, but not in powder form. From reference [57].

3.2.2.2 Residual contaminants in solution-processed materials

Not only will the nanosized nature of solution-processed materials pose potential risks, but the chemical composition (and thus the toxicity) of the electronic materials used to build TFTs and sensors will be altered depending on the processing conditions. At low annealing temperatures, there may be incomplete conversion of the sol-gel metal precursors to the target metal oxide material. Thus a “ZnO” film may contain myriad other chemicals in concentrations that depend on the precursors and processing conditions. This will, of course, cause significant changes in the electronic performance of solution-processed TFTs, but it will also impact the toxicity and dissolution rates of the materials. Many of the metal precursor materials that are commonly used in the preparation of metal oxide thin films from sol-gels pose significant risks to human health. For example, tin chloride dihydrate ($\text{SnCl}_2 \cdot 2\text{H}_2\text{O}$) is a precursor for tin oxide films (SnO_2). Though tin oxide itself is biocompatible in its bulk form,

exposure to tin chloride dihydrate causes severe skin burns, eye damage, cardiovascular organ damage, and is suspected of causing genetic defects and damaging the unborn child. Similarly, some precursors for zinc oxide and zirconium oxide (i.e. zinc acetate dihydrate and zirconium acetylacetonate, respectively) are harmful if swallowed, and cause irritation upon skin exposure. Therefore, sol-gel precursors and processing conditions must be optimized to achieve biocompatibility.

In nanocrystal inks, conversion from precursors to the target material is controlled during the synthesis phase rather than during the post-deposition anneal. Thus, incomplete conversion is less of a concern. However, the toxicity of thin films obtained from colloidal nanocrystals is still dependent on the processing conditions because the encapsulating ligands surrounding the nanocrystals must be removed; this typically occurs during the annealing process. Excess ligands and other molecules that are necessary to achieve the desired fluid properties of printable inks may remain in the final device, and many of these ligands cause significant tissue damage. Many commonly used ligands (such as oleylamine and trioctylphosphine oxide) are corrosive, causing skin and eye damage upon contact. Some (such as dodecylamine) are fatal if swallowed. However, some of the standard ligands are considered not hazardous or cause minimal irritation (octadecylphosphonic acid and oleic acid, respectively). If further studies reveal that significant amounts of excess ligand molecules remain in the film after processing and increase the material toxicity, nanocrystal synthesis procedures and post-deposition processing steps will need to be adjusted to achieve non-toxic materials.

3.3 Progress Towards Biocompatible Printed Electronics

3.3.1 High-performance biocompatible TFTs

To demonstrate the promise of metal oxides for high-performance biocompatible electronics, TFTs were fabricated using materials previously shown to be non-toxic: tin oxide [58] semiconductor, zirconia [59] gate dielectric, and gold [60] contacts. Devices were fabricated for ease of testing on ITO-coated glass substrates. ITO has been associated with health concerns [61] in LCD manufacturing, but the ITO gate electrode here could be replaced with gold to make a completely biocompatible device stack. The liquid SnO₂ precursor was prepared by dissolving 1 mmol SnCl₂·2H₂O (CAS 10025-69-1, >99.995%) in ethanol and sonicating for 1 minute. The liquid ZrO₂ precursor was prepared by dissolving 1 mmol zirconium (IV) acetylacetonate (CAS 17501-44-9) and 0.1 mL ethanolamine (CAS 141-43-5) in ethanol and sonicating for 1 hour. The ZrO₂ was spin-coated onto the ITO substrate for 30 seconds at 3000 rpm, then dried for 1 minute on a hotplate at 350°C; this was repeated to deposit 5 layers of ZrO₂ onto the ITO substrate. Gold source/drain electrodes (50 nm) were deposited using thermal evaporation through a shadow mask (W/L = 200 μm/100 μm). The SnO₂ was then spin-coated on top of the ZrO₂ and gold for 30 seconds at 3000 rpm and dried for 5 minutes on a hotplate at 160°C. The devices were then annealed in air in a tube furnace at 500°C for one hour. A schematic of the complete TFT stack is shown in Figure 3.7, along

with typical transfer and output characteristics. These devices exhibit excellent performance [9], with field effect mobility values reaching $40 \text{ cm}^2/\text{Vs}$. These results show a promising route towards high-performance solution-processed electronics made with all biocompatible materials.

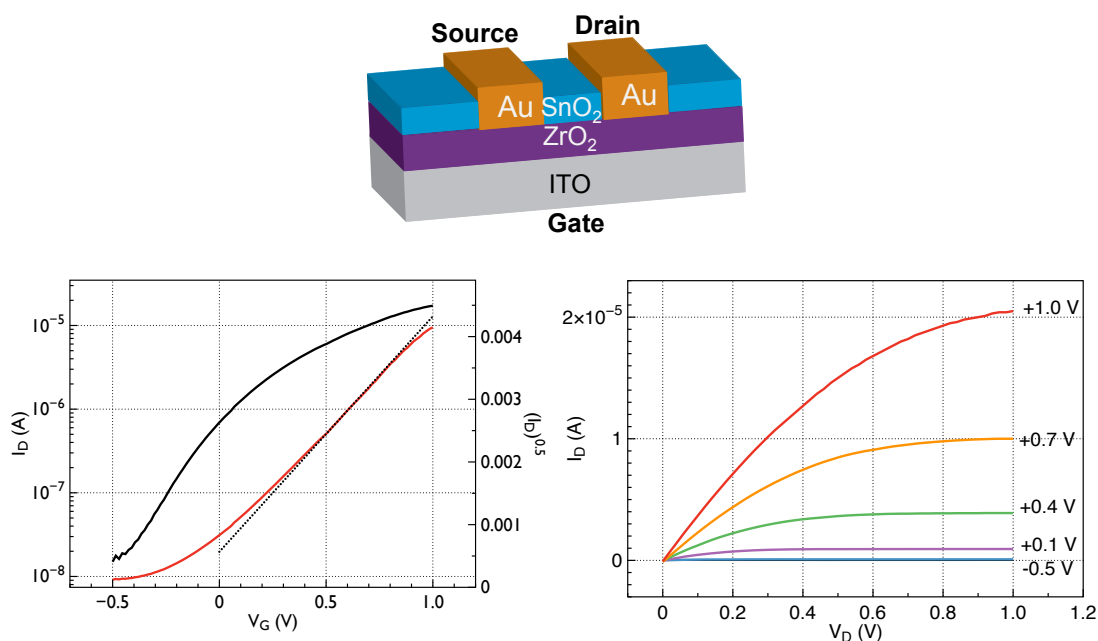


Figure 3.7: Transfer and output characteristics for SnO_2 TFTs.

High-performance solution-processed materials (SnO_2 semiconductor and ZrO_2 gate dielectric) [9] are excellent candidates for biocompatible solution-processed electronic devices.

3.3.2 Dissolution in a simulated body environment

Many people anticipate medical devices in the future that are designed to disintegrate and be absorbed into the body when their functions are complete, much like dissolvable sutures. These “resorbable” electronics might, for example, monitor the healing process of an internal surgical wound and wirelessly transmit information to a receiver outside the body. Rather than performing a secondary surgery to remove the device, it would simply dissolve harmlessly into the body over time. While the safety of resorbable devices needs to be thoroughly studied for local toxicity effects, the same biocompatible materials in Table 3–1 are also promising candidates for resorbable electronics.

One notable demonstration of dissolvable electronics is a study by Hwang, *et al.* [30] in which silicon-based devices on flexible substrates were dissolved in water. These “transient electronics” used magnesium, magnesium oxide, and crystalline silicon nanomembranes as the conductor, dielectric, and semiconductor, respectively. The substrate was made of solution-cast silk, which is water-soluble and enzymatically degradable. Inductors, capacitors, diodes and transistors were demonstrated using these materials; all components disintegrate in water over a time period of 10 minutes. The transient nature of these materials is clearly illustrated in Figure 3.8.

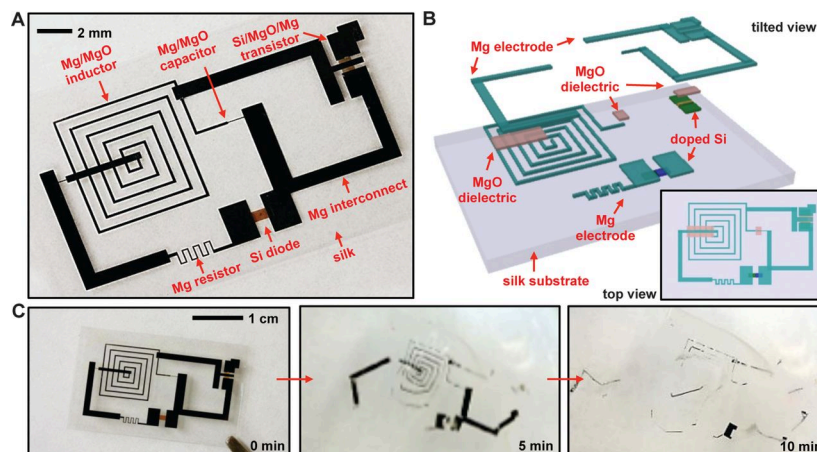


Figure 3.8: Silicon-based transient electronics.

A demonstration of a transient silicon-based electronics platform, from reference [30].

The dissolvable circuits described above were fabricated using traditional thin-film techniques (vacuum deposition, lithography, etching). To demonstrate this concept using printable materials, solution-processed ZnO semiconductor films were dissolved in a simulated body environment. The liquid ZnO precursor was a 0.2M solution of zinc acetate (CAS 557-34-6) in methanol. The ZnO precursor was spin-coated onto an oxidized silicon wafer for 60 seconds at 1000 rpm, then annealed for 1 hour at 200°C on a hotplate. This method has previously yielded TFTs with mobility values around 1 cm²/Vs. The ZnO films were submerged in phosphate-buffered saline (PBS) solution with pH of 7.4 and held at 37°C to mimic blood. Figure 3.9 shows the dissolution of the ZnO film over the course of 5 hours. Incorporating a device encapsulation layer with a slower degradation time would extend the operation life of the device implanted in the body. Poly(lactic-co-glycolic acid) (PLGA) is an excellent candidate for encapsulation because it is an FDA-approved polymer, and the physical properties and dissolution time can be tuned by adjusting parameters such as the ratio of lactide to glycolide [62]. This validates the idea that biocompatible solution-processed materials can dissolve into the body, making a resorbable sensor a possibility.

ZnO film					
Time (hr)	1	2	3	4	5
Thickness (nm)	63	55	19	25	0

Figure 3.9: Dissolution of ZnO film in PBS.

Solution-processed ZnO film dissolves in a simulated body environment, phosphate buffered saline (PBS).

3.4 Future Studies

3.4.1 Promising material candidates

In addition to the excellent electrical and mechanical properties of metal oxides that were highlighted in chapters 1 and 2, these materials are also appealing because they are promising candidates for biocompatible printed electronics. Many metal oxides have already been demonstrated to be safe and non-toxic in some applications; for example, ZnO [63], Al₂O₃ [64], and SnO₂ [58] have been approved by the U.S. Food and Drug Administration (FDA) for use in cosmetics, and Al₂O₃ [65] and ZrO₂ [59] have been employed for decades in medical devices such as total hip replacements. Metal oxides can be used to fabricate each layer of a TFT (conductors, semiconductors, and insulators) by changing the deposition conditions, so it is realistic to expect that high-performance TFTs could be fabricated exclusively from biocompatible materials. However, FDA approval for biocompatibility is based on the particular *preparation method* of a material. Thus, any *new* preparation or manufacturing method for a given material must undergo all the standard safety tests required for FDA approval. Solution-processed metal oxides, therefore, cannot strictly be considered “biocompatible” materials until they undergo tests for toxicity. Table 3–1 lists several materials that have been successfully used to build flexible or printed electronics that are also likely to be biocompatible. Testing the toxicity of these materials in their solution-processed form will help to streamline future research efforts towards printed biocompatible devices.

Materials to Investigate for Biocompatible Printed Electronics	
Semiconductors	In ₂ O ₃ , SnO ₂ , ZnO, In-Ga-Zn-O combinations
Gate Dielectrics	ZrO ₂ , Al ₂ O ₃
Conductors	Au, Ag, Al:ZnO, Sb:SnO ₂ (ATO), In:SnO ₂ (ITO)
Substrates	Silk, cellulose, Poly (lactic- <i>co</i> -glycolic acid) (PLGA)

Table 3–1: Promising materials for biocompatible printed electronics.

Semiconductor, dielectric, conductor, and substrate materials that have been used for printed or flexible electronics, and are promising candidates for biocompatible electronics. Screening these materials for cytotoxic and genotoxic effects is an important first step before attempting *in vivo* animal studies or pre-clinical trials.

3.4.2 Dependence of toxicity on processing parameters

In vitro toxicology studies are needed to identify which materials are the most promising candidates for biocompatible solution-processed electronics. As outlined in section 3.2.2, the toxicity of solution-processed nanomaterials will likely depend on the conditions under which they are processed (solvents and ligands used, annealing temperature, etc). Therefore, once the list of materials is narrowed down, the next round of experiments needs to determine the optimal processing conditions of those materials. The key aim is to find the materials and processing conditions that maximize device performance and minimize the material toxicity.

The first proposed step is a screening experiment to identify which printable electronic materials are the least toxic. Starting with the materials listed in Table 3–1, the MTT assay and the Ames assay should be used to identify the acceptable options from each material category (semiconductor, gate dielectric, conductor, substrate). It is expected that higher processing temperatures will result in lower toxicity because there will be less residual contamination in the film (in other words, more “bulk-like”). Thus the highest possible temperature for each material should be used for the screening experiment; if the material is not biocompatible at high annealing temperatures, it is unlikely to be biocompatible at lower temperatures. Maximum processing temperatures should not exceed 400°C to remain compatible with plastic substrates.

The screening experiment will eliminate the materials with the highest toxicity. Remaining material options should be put through a rigorous multifactorial experiment examining the TFT performance and toxicity under various process conditions. The annealing temperature will likely have a significant impact on the material properties; temperatures between 150-400°C are typical for metal oxides, and should be investigated. If there are various chemical routes to obtain a given material (i.e., preparation in different solvents), each recipe should be included in the experiment. Each sample should be tested for toxicity (MTT and Ames assays), and the relevant material properties should be recorded and compared (breakdown strength and leakage for gate dielectrics, mobility for semiconductors, etc). The outcome of these proposed experiments will be a library of solution-processed materials and preparation methods where material performance can be weighed against potential toxicity. This will help direct future work on biocompatible printed electronics.

The details of the proposed experiments can be summarized as follows:

1. Screening experiment

- a. Input factor: Materials in Table 3–1
- b. Responses: Cytotoxicity (MTT assay)
Genotoxicity (Ames assay)
- c. Constants: Annealing temperature = 400°C or maximum usable temperature, whichever is lower
Annealing ambient = air
Solvent/ligands (select one preparation method for each material the initial screening)

2. Multifactorial study of preparation conditions and toxicity

- a. Input factors: Material = non-toxic candidates from each category (semiconductor, dielectric, conductor)
Annealing temp = 150°C , 200°C, 300°C, 400°C
Material preparation method: multiple solvent/ligand recipes if available
- b. Responses: Cytotoxicity (MTT assay)
Genotoxicity (Ames assay)
Morphology (particle size, crystallinity)
Dielectrics: breakdown strength, leakage, dispersion, surface morphology

Semiconductors: TFT mobility, I_{ON}/I_{OFF} , hysteresis
Conductors: conductivity, surface morphology

3.5 Conclusions

Flexible electronics hold significant promise as a platform for novel biosensors for medical and fitness applications. Developing non-toxic, biocompatible solution-processed materials is a prerequisite for printed electronics if they are to realize low-cost flexible devices that are safe to be worn or used in contact with (or implanted inside) the human body. Many metal oxides are approved for use in medical devices and cosmetics, so – when combined with their excellent electronic characteristics and their ability to be deposited from liquid precursors – they are ideal candidates for biocompatible flexible electronics. In this chapter, high-performance TFTs made from likely biocompatible materials were demonstrated, as well as the ability to dissolve such materials in a simulated body environment. However, the unique properties of nanomaterials and solution-processed thin films require more in-depth investigation to ensure biocompatibility. Several promising materials were presented that are likely candidates for biocompatible printed electronics, and the *in vitro* tests for cytotoxicity and genotoxicity were discussed that are recommended in accordance with ISO 10993, “Biological evaluation of medical devices”.

Chapter 4: Detection of Pressure

Ulcers *in vivo*

4.1 Introduction

Flexible electronic systems have the potential to revolutionize many aspects of health care and medical monitoring. As discussed in chapters 1 and 3, many aspects of flexible electronics – namely their low cost, light weight, and ability to conform to the human body – will enable innovative biomedical sensing applications. In this chapter, one such application is demonstrated: a wound monitoring system featuring a flexible sensing array detects pressure-induced tissue damage by measuring the electrical impedance of the skin [66].

4.1.1 Pressure ulcers: causes and prevention

Chronic skin wounds have been called “a silent epidemic” posing a significant threat to public health and the economy [31]. Each year, an estimated US\$25 billion is spent on the treatment of chronic wounds [31]. They are more common in patients who are diabetic, obese, or elderly; thus, the sharp increase in obesity and diabetes worldwide and the aging population in the U.S. – combined with the ever-increasing cost of health care – underscore the need for advances in wound care. Pressure ulcers are chronic wounds with a particularly high rate of morbidity, affecting over 2.5 million patients and costing an estimated \$11 billion per year in the U.S. alone [31]. A pressure ulcer develops when pressure is applied to a localized area of the body over a period of time, such as when a patient lies in the same position during a lengthy surgery, stays in the ICU, or has limited mobility. Injury typically occurs over a bony prominence, such as the sacrum, heels, or the back of the skull [31], [67]–[69], as shown in Figure 4.1. The pressure causes a loss of blood flow to the tissue resulting in necrosis, and subsequent infection is a major concern. The combination of pressure, time,

and ischemia-reperfusion cycles that results in a pressure ulcer varies widely between patients [31], [67]–[69], making them difficult to predict. Damage can occur from an ischemic event as short as two hours [67]–[69], and the initial stages of damage are not easily detectable with the naked eye. By the time a surface wound is visible, the underlying tissue damage is often severe [67]–[69].

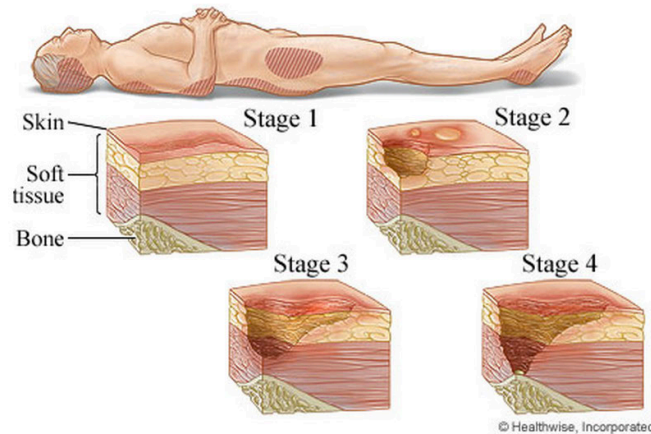


Figure 4.1: Formation and stages of pressure ulcers.

Image source: <http://www.webmd.com/skin-problems-and-treatments/four-stages-of-pressure-sores>.

Prevention of pressure ulcers currently relies on labor-intensive vigilance in nursing care [68]–[70]. Patients are manually turned nearly every hour to relieve pressure, and high-risk areas are visually inspected for pressure ulcers [68]. Pressure-sensitive devices can alert nursing staff when a threshold of pressure is exceeded. However, it is progressive tissue damage that determines ulcer development, not the instantaneous pressure itself. Accurate correlations between the amount of pressure, duration of pressure, and ulcer development across patient populations do not exist. In effect, no clinically relevant method exists to detect progressive tissue damage to indicate a patient is at imminent risk of developing an ulcer.

4.1.2 Biological impedance measurements

A body of literature exists that has both measured and modeled the electrical changes in cells and tissue both *in vivo* and *in vitro*, as well as provided correlations between electrical properties and cell types; this work has been summarized previously [71]–[76]. From an electrical perspective, a cell can be represented as an ion-rich conductive center (cytoplasm) embedded in an ion-rich conductive medium (extracellular fluid), separated by a relatively non-conductive barrier (cell membrane), as illustrated in Figure 4.2. These ion-rich media can be described in terms of their ability to conduct charge by modeling them as resistances. Likewise, barriers to charge flow (e.g. the cell membrane) can be modeled as electrical capacitances. The combination of the loss terms (i.e. resistance) and energy storing terms (i.e. capacitance, inductance) is known as *electrical impedance*. Because the impedance of a material is a function of the electrical signal being passed through it, impedances are

measured across many frequencies to form a spectrum plot; this is known as *impedance spectroscopy*. The complex impedance \mathbf{Z} of a medium can be expressed in polar form as

$$\mathbf{Z} = |Z|e^{j\theta} \tag{1}$$

with magnitude $|Z|$ and phase angle θ , or in Cartesian form as

$$\mathbf{Z} = R + jX \tag{2}$$

with resistance R and reactance X . The reactance X represents the energy storage term; from equations (1) and (2) we see that a material with a higher capacity for energy storage (or polarization) will exhibit a larger reactance, X , and a larger phase angle, θ .

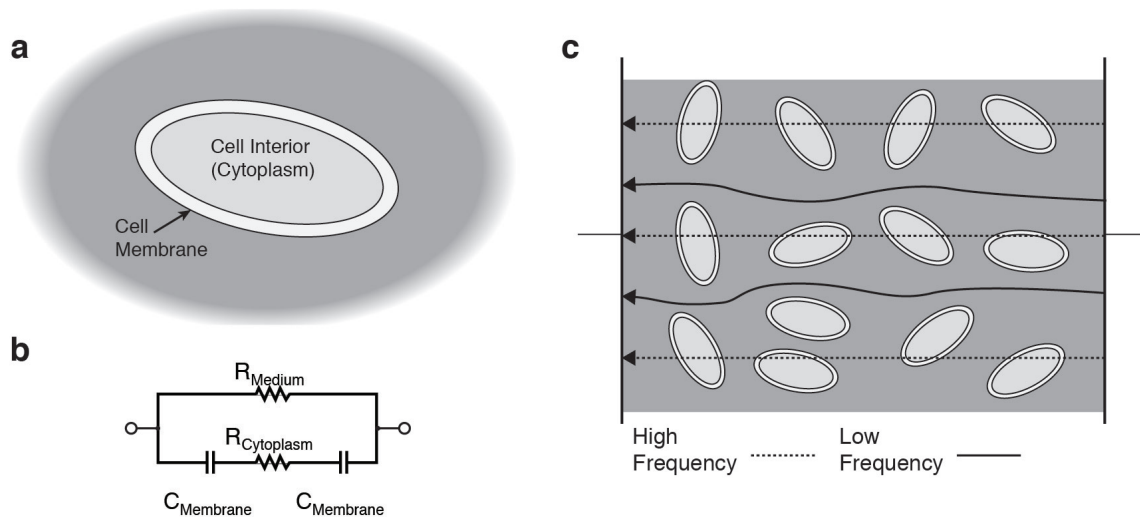


Figure 4.2: Simplified model of electric current through cells. Simplified diagram of a single cell (a) and its equivalent RC circuit model (b), and an illustration of high- and low-frequency current paths through biological tissue (c). Adapted from Grimnes, *et al.* [72]

Certain disturbances of the biological structures result in detectable changes in the impedance spectrum. For example, *in vitro* impedance measurements have been shown to detect cell proliferation and cell-drug interaction [77], quantify biomass in suspensions [76], [78], and create two-dimensional images of cell migration [79]. Much of this work utilizes the electrical “signature” of the cell membrane: a well-functioning cell membrane is relatively impermeable and thus behaves like a capacitor in the presence of electric current [74]–[76], [78], [80]. Cell damage or death results in a loss of membrane structure and integrity, allowing ions and current to pass through the membrane. Thus damaged cells will exhibit higher electrical conductance through the membrane and less capacity to store charge [75]; in other words, the cell behaves less like a capacitor and more like a resistor. In an impedance measurement, this manifests itself as a phase angle θ closer to zero (or equivalently, a smaller reactance, X). Impedance measurements of tissues *in vivo* have also correlated better tissue health with more reactive impedance values: bioelectrical impedance analysis of patients at

high risk for developing pressure sores (as determined by the Braden Scale [81]) exhibited lower reactance and phase angle than the control group [82]. Further studies have observed that reactance increases with epidermal proliferation and granulation, and decreases with infection and cell loss, suggesting that a larger phase angle indicates healthier cell membranes while a decreased phase angle indicates impaired membrane function [83]. Many researchers are actively exploring this area; in fact, clinical trials [84] are underway and impedance-based wound monitoring devices have been patented [85]. These results led to the hypothesis that pressure ulcers may be able to be detected and diagnosed based on the changes in electrical impedance caused by the loss of cellular integrity or cell death following an ischemia/reperfusion event.

In this chapter a flexible, electronic device is demonstrated that non-invasively detects pressure-induced tissue damage, even when such damage cannot be visually observed. Employing impedance spectroscopy across flexible electrode arrays *in vivo* on a rat model, the frequency spectra of impedance measurements were found to correlate in a robust way with the state of the underlying tissue across multiple animals and wound types. Flexible and stretchable electronics for bio-monitoring applications is currently an area of intense research focus [27]–[30]; these results demonstrate the feasibility of an automated, non-invasive “smart bandage” for early diagnosis of pressure ulcers, improving patient care and outcomes.

4.2 Methods

4.2.1 *Two-dimensional electrode array for impedance mapping*

Figure 4.3 illustrates typical methods of measuring impedance of biological tissues in previous studies, from cell cultures to full-body measurements to “localized” wound measurements. Impedance studies to characterize wounds *in vivo* have typically used a single reference electrode placed relatively far away from the wound site. Even “localized” impedance measurements rely on electrodes placed on either side of the wound, which does not provide fine enough spatial resolution to correlate the impedance measurement with different tissue types. For example, the wound bed may contain some granulation tissue and some scab, but these details would be lost in a single measurement of the entire wound. The problem is further confounded by the fact that the current path is unknown (see section 4.2.6.4), so it is impossible to know whether the wounded tissue was actually contributing to the impedance measurement.

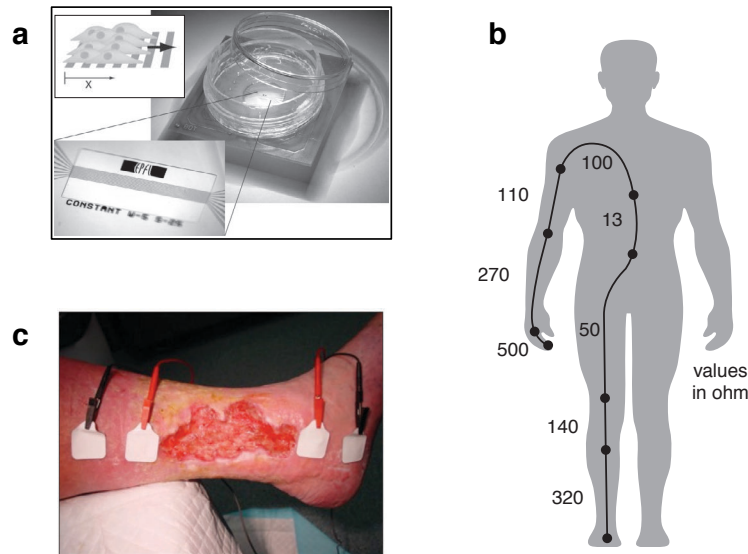


Figure 4.3: Biological impedance measurements.

(a) Cells grown over linear electrodes [79]. (b) Whole-body impedance measurements taken between a hand and a foot, used mainly for body composition analysis [72]. (c) “Localized” wound impedance measurements [83].

In this work, a two-dimensional (2D) array of electrodes is used to provide impedance data with high spatial resolution relative to the wound. Rather than using a single set of electrodes, 55 electrodes were spaced equally in a hexagonal pattern (Figure 4.4a). Selecting any two neighboring electrodes allows an impedance value to be assigned specifically to the tissue at the location of that electrode pair (Figure 4.4b). By performing sequential pair-wise impedance measurements, the impedance magnitude and phase can be plotted as a function of the position of the electrodes (Figure 4.4c), and thus an impedance “map” can be created. This represents a significant advantage over previous studies: with the ability to measure impedance with high spatial resolution and correlate those impedance values to the condition of the tissue, a robust method of detecting damaged tissue can be developed. If the impedance of the tissue can be detected with sufficient sensitivity to discern between healthy tissue and wounded tissue, a 2D impedance sensing array can automatically detect the size and shape of the wound by identifying the wound border. Furthermore, the type of tissue in the wound bed – granulation tissue, pus, scab, etc. – could potentially be identified based on its impedance. Thus, a 2D impedance array provides clear benefits due to the high spatial resolution and the ability to correlate impedance values with a specific location within the wound. Two versions of the electrode array were developed for this study: 1) a commercial rigid printed circuit board (PCB) with gold-plated electrodes, and 2) a flexible bandage-like array produced using inkjet printing on a plastic substrate.

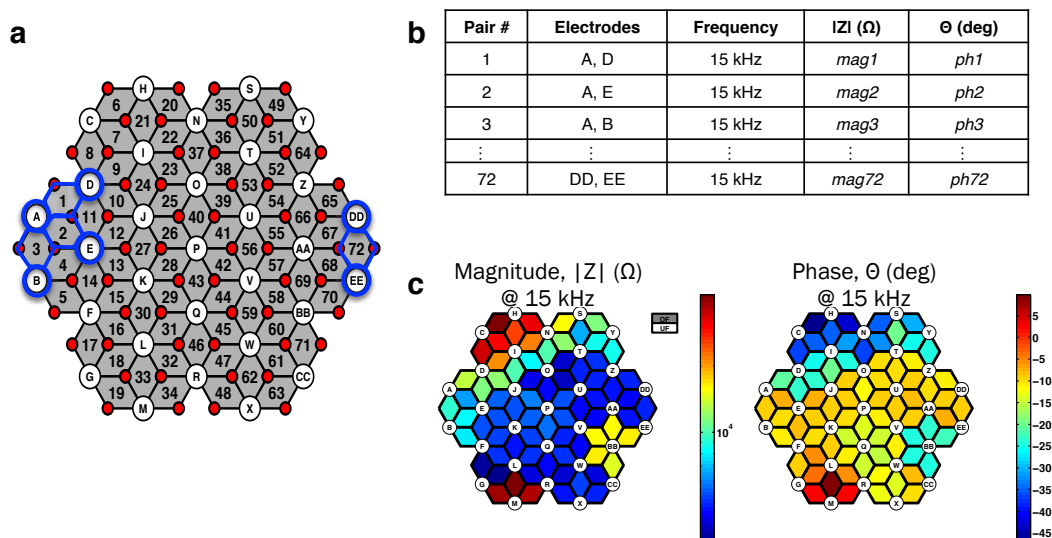


Figure 4.4: Creating 2D impedance maps.

Complex impedance is measured pair-wise across an array of hexagonally-arranged electrodes (a), and the impedance values are recorded with the spatial location of the electrode pair (b). Impedance maps of magnitude and phase at a given frequency (c) are created to provide a visual representation of the underlying tissue health.

4.2.2 Rigid electrode array board

The rigid device was a robust calibration platform that allowed the *method* of detecting pressure ulcers using impedance spectroscopy to be developed while, in parallel, developing the *flexible device* to employ that method *in vivo*. The rigid array was a custom PCB purchased from Advanced Circuits consisting of three layers of FR4 with 1 oz. copper on all layers. All routing was contained on the inner layer of the PCB, with solid copper pours on the outer layers to reduce noise in the measurements. The rigid and flexible arrays had an identical arrangement of 55 electrodes in a hexagonal pattern. The electrodes were plated with immersion gold to provide an inert surface to prevent any surface reactions in the presence of ionic liquids. The overall dimensions of the rigid board were 30.5 mm x 47 mm x 1.5 mm thick, and the array area was roughly 340 mm². The rigid electrode array is shown in Figure 4.5a, and further detailed specifications are provided in Table 4–1.

4.2.3 Ink-jet printed electrode array

While the rigid PCB was an excellent development tool for the impedance sensing method, a flexible array can provide more conformal contact to the body, and represents an important step towards a true ‘smart bandage’ device. The fabrication of the printed flexible array is shown in Figure 4.5. The flexible sensor array was ink-jet printed on top of thin (35 μ m) planarized polyethylene naphthalate (PEN) substrates obtained from DuPont. Gold nanopaste ink purchased from Harima (Model: NPG-J) is made up of gold nanoparticles \sim 7 nm in diameter. The ink contains 53% metal content prior to sintering, with the particles suspended in a proprietary solvent mixture. The gold ink was inkjet-printed with 30 μ m drop spacing using a Dimatix Materials Printer (DMP-2800). Printed features were cured with a

slow ramp annealing step on a hotplate (30°C to 230°C with 0.7°C/ min ramp) to remove excess solvent without cracking the film. This was followed by a constant temperature bake at 230°C for 60 minutes in air on a hotplate to further densify the film and achieve the desired conductivity. The minimum line width was 90 μm, and the electrode pads were 500 μm in diameter. All lines were printed as a single layer, requiring slight changes in the routing when compared to the rigid board. Thickness of the printed lines was measured with a Dektak Profilometer, and ranged from 0.5 μm to 1 μm. The average sheet resistance determined using four-point probe measurements was $R_S = 0.54 \Omega/\square$. An amorphous fluoropolymer (Cytop CTX-809A) coating was then spun at 1200 rpm to produce a 100 nm film to insulate and protect the conductive traces during *in vivo* measurements. Vias were selectively opened over the electrodes using oxygen plasma etching through a shadow mask. The flexible array is depicted in Figure 4.6b, and a detailed comparison of the specifications of the rigid PCB electrode array board and the flexible inkjet-printed electrode array is provided in Table 4–1.

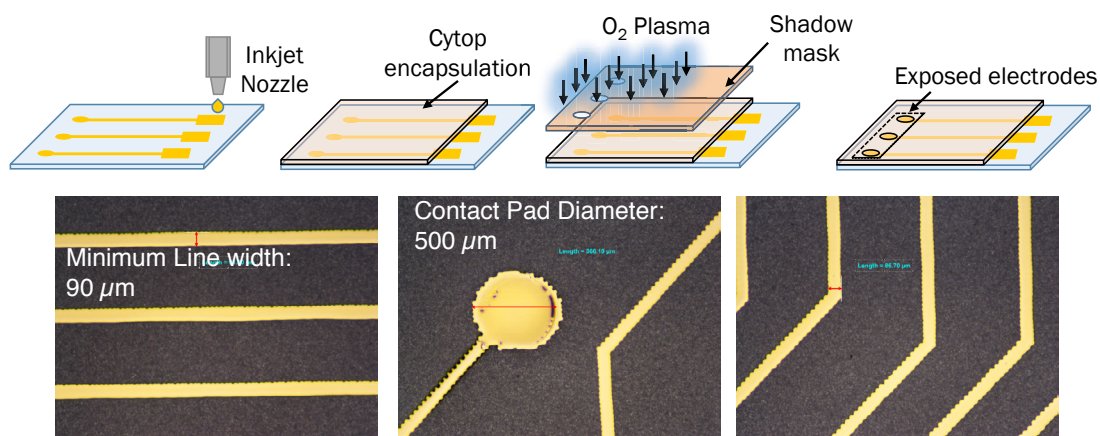


Figure 4.5: Inkjet-printed flexible electrode array.

Gold nanoparticle ink was inkjet-printed onto a thin plastic substrate to create a flexible sensor array capable of making conformal contact during *in vivo* measurements.

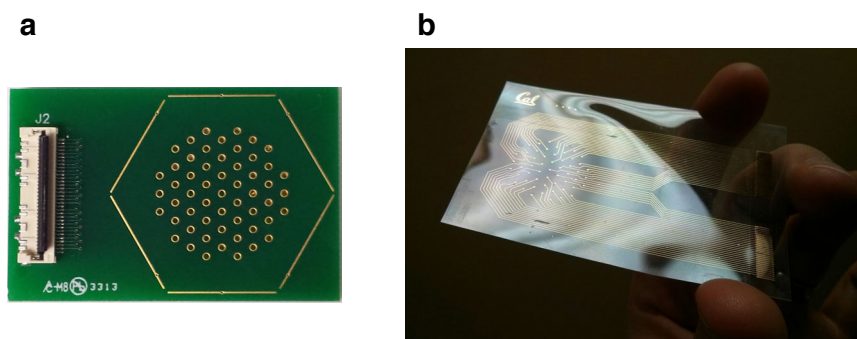


Figure 4.6: 2D impedance sensor electrode arrays.

Photos of the rigid PCB sensing array (a) and the flexible inkjet-printed array (b).

	Inkjet-printed Flex Array	Rigid PCB Array
SENSOR ARRAY		
Overall board dimensions (mm)	40 x 70	30.5 x 47
Overall thickness (mm)	0.035	1.5
Number of electrodes	55	55
Center-to center electrode spacing (mm)	2.54	2.54
Sensor array area (sq. mm)	339	339
Minimum Trace length (mm)	44.61	18.87
Maximum Trace length (mm)	84.82	30.68
Trace line width (um)	90	102
Minimum Trace resistance (Ohms)	240	0.09
Maximum Trace resistance (Ohms)	400	0.15
Minimum Trace-to-trace spacing (um)	400	127
Sense electrode outer diameter (um)	500	980
Sense electrode inner diameter (hole size) (um)	n/a (solid pad, no via)	730
Sense electrode area (sq. um)	1.96E+05	3.36E+05
Trace conductor material	Gold (Sintered Nanoparticle)	Copper (1 oz = 35 um thick)
Electrode surface material	Gold (Sintered Nanoparticle)	Gold (Immersion plated)
Substrate material	Polyethylene naphthalate (PEN)	FR4 (glass-reinforced epoxy resin)
Number of metal layers (total)	1	3
Number of metal layers (routing)	1	1 (Inner layer only)
Encapsulation material covering traces	Cytop CTX-809A	Soldermask
CONNECTION TO CONTROL BOARD		
Connection path	Flex array --> insert into ZIF on daughter board --> FFC --> Control board	Rigid array (with ZIF connector installed) --> FFC --> Control board
Daughter board required?	Yes	No
Number of connectors between sense electrodes and control board	3	2
MOUNTING TO WOUND		
Hydrogel applied to sense electrodes?	Yes	Yes
Held in place during measurement using	Tegaderm adhesive dressing + Coban self-adherent wrap	Coban self-adherent wrap

Table 4–1: Specifications of flexible and rigid arrays.

Two types of sensor arrays were designed for this study: 1) a rigid calibration sensor array and 2) and inkjet-printed flexible sensor array. Both arrays were used to measure impedance of wounds *in vivo*, and provided similar results.

4.2.4 Rat model for pressure ulcers

Wildtype rats (Sprague-Dawley, 250—300g, 8 weeks old, male) were anesthetized with isoflurane mixed with oxygen. Hair was shaved from the back, depilated with Nair, and then the area was cleaned with mild detergent (Dawn) and isopropyl alcohol. The skin was gently tented up and placed between two round, flat magnets (5 x 12 mm diameter, 2.4 g weight, 1000 G magnetic force). This procedure, shown in Figure 4.7, left a 5 mm skin bridge between the magnets, creating approximately 50 mm Hg pressure between the plates. Rats tolerated the procedure well, returning to normal activity within a few minutes with the magnets in place. Magnets were removed after 1 or 3 hours, and impedance measurements were taken while rats were under isoflurane anesthesia daily for 3 days. Rats received a 1-hour treatment and a 3-hour treatment on different areas of the back on separate days; the animals sacrificed for histological analysis on the day of pressure treatment received either the 1-hour or 3-hour treatment but not both. Study sample size was chosen in consultation with a professional statistician at UCSF to minimize animal numbers and suffering while providing statistically significant results. All procedures were reviewed and approved by the University of California San Francisco Institutional Animal Care and Use Committee (IACUC, approval number AN100403-01C).

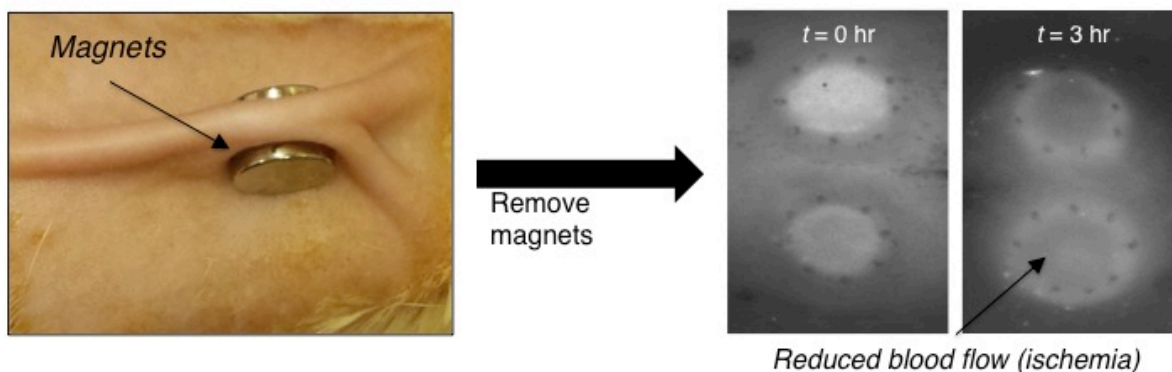


Figure 4.7: Formation of pressure ulcers on rat model.

Magnets apply pressure to the skin on the back of a rat, resulting in ischemic damage to the tissue.

4.2.4.1 Fluorescence angiography

To confirm that the magnets created reversible and irreversible tissue damage in our pressure ulcer model, fluorescence angiography was used to detect blood flow in the area of tissue injury after release of the magnets. Fluorescence angiography utilizes an injected fluorescent dye, indocyanine green (ICG), that briefly binds to plasma proteins and is thus confined to the vascular system. The principle of imaging blood flow with ICG is illustrated in Figure 4.8. The peak spectral absorption of ICG is around 800 nm (depending on the solvent used and the chemical environment), and it has a broad fluorescence spectrum between 750-950 nm [86]. Because these near-infrared (NIR) wavelengths can penetrate tissue rather efficiently, ICG can be used to image blood flow well below the surface of the skin. Using a Novadaq SPY NIR imaging system, tissue with increased blood flow appeared bright, while tissue with low blood flow appeared darker (Figure 4.9). In the tissue with

reversible injury (1 hour treatment group), increased fluorescence (reactive hyperemia) was observed immediately after relieving the pressure from the magnets. The hyperemia was still evident within a few hours of reperfusion. From Day 2 onward, the 1 hour treatment group displayed no detectable difference in fluorescence between the area subjected to the magnets and the surrounding healthy skin. In the tissue with irreversible injury (3 hour treatment group), the angiography demonstrated increased fluorescence after the magnets were released. A few hours later, the central part of the injured tissue had decreased fluorescence compared to the periphery in some animals while others still had increased fluorescence. Within a few days after release of the pressure, all tissues exhibited a central area of decreased fluorescence consistent with the onset of visible tissue injury. Thus these findings using fluorescence angiography suggest that 1 hour of pressure results in reversible alterations of tissue perfusion but 3 hours of pressure causes a permanent decrease of tissue perfusion and permanent tissue damage that results in an ulcer.

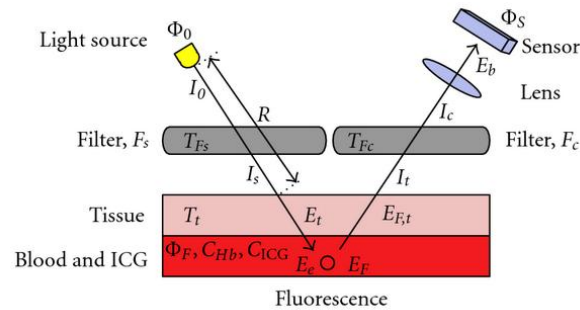
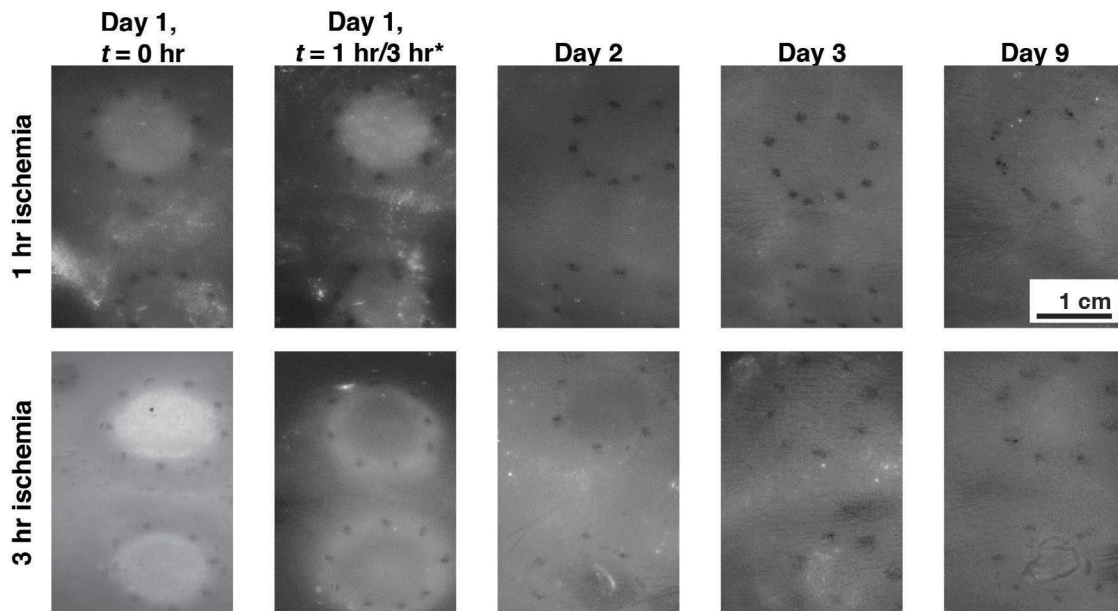


Figure 4.8: Principle of fluorescence imaging with ICG.

A high-pass filter, F_s , removes the fluorescent wavelengths from the incident light source. The blood and ICG suspension under the tissue absorbs the excitation wavelengths and emits in the fluorescent band. The emitted light goes through a low-pass filter, F_c , before reaching the sensor to remove the excitation light reflected from the source. (From reference [86]).



* 1 hr reperfusion time for 1 hr ischemia; 3 hr reperfusion time for 3 hr ischemia. No ICG reinjection

Figure 4.9: Fluorescence angiography following ischemic event.

Fluorescence angiography for 1 hour (top row) and 3 hours (bottom row) of magnet-induced pressure. Angiography was measured on Day 1 immediately after removing the magnets ($t = 0$ hr) and after reperfusion ($t = 1$ hr/3 hr), then measured again on days 2, 3, and 9. The tissue with reversible injury (1 hour treatment group) displays increased perfusion at the site of magnet application for the first day, but no difference from healthy skin beginning from day 2. In the tissue with irreversible injury (3 hour treatment group), the angiography demonstrated increased fluorescence after the magnets were released. A few hours later, the central part of the injured tissue had decreased fluorescence compared to the periphery in some animals while others still had increased fluorescence. Within a few days after release of the pressure, all tissues exhibited a central area of decreased fluorescence consistent with the onset of visible tissue injury. Scale bar (1 cm) applies to all images.

4.2.5 Skin samples for histology

Full thickness skin wounds were excised, immediately placed flat in cassettes and stored in 10% NBF (neutral buffered formalin) for 24-72 hours. Tissue was then transferred to 70% ethanol and stored for up to 1 week. Samples were embedded in paraffin and sectioned at 5 microns. Slides were stained with hematoxylin and eosin.

4.2.6 Impedance measurements

A diagram illustrating the wound measurement system is shown in Figure 4.10. Impedance magnitude and phase were measured using an Agilent E4980AL 20 Hz-1 MHz Precision LCR meter with a 100 mV constant voltage sine wave output signal with a frequency of 100 Hz – 1 MHz. Each electrode on the array can be independently selected by the control hardware, allowing pair-wise impedance measurements between electrodes. Custom software implemented in Python communicated with the control hardware to select electrode pairs in a specified sequence, and simultaneously controlled the LCR meter. A

microcontroller on the control board routed the test signal from the LCR meter to the selected electrodes, the impedance was recorded, then the microcontroller selected the next set of electrodes in the measurement sequence. Impedance data were analyzed using a suite of custom MATLAB scripts utilizing the Statistics, System Identification, and Control System Toolboxes.

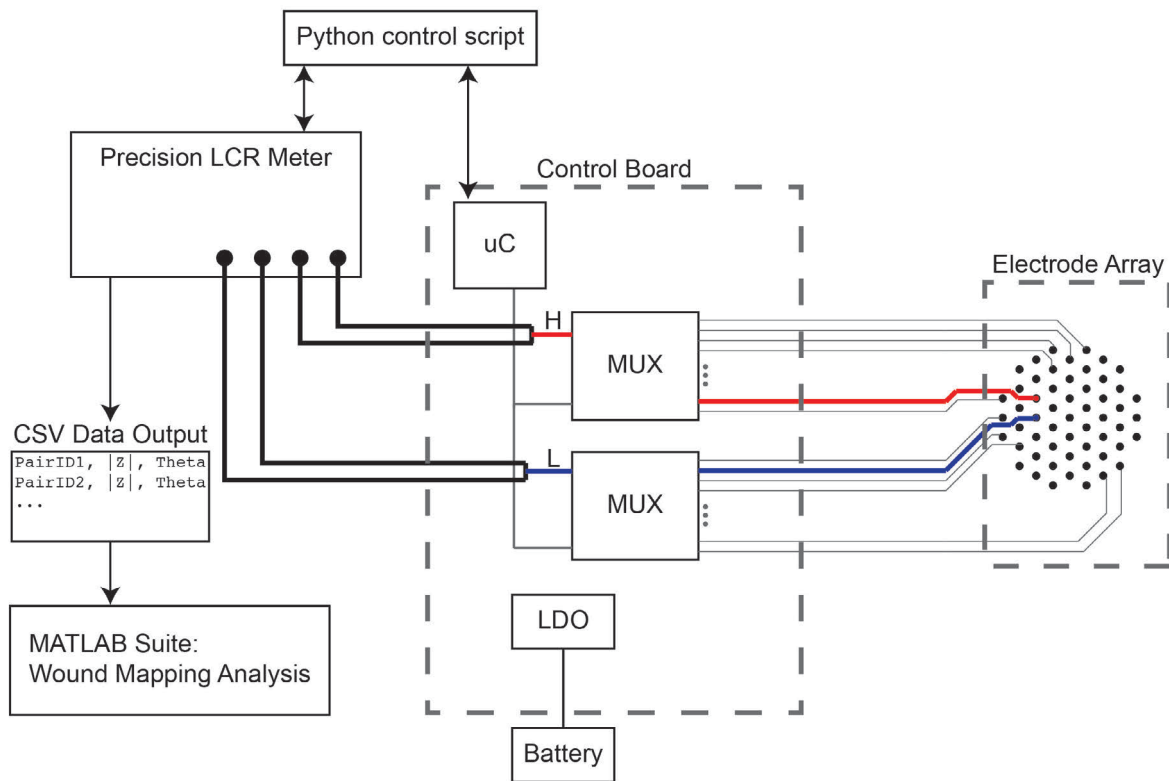


Figure 4.10: Wound measurement system diagram.

The Control Board routes signals from the precision LCR meter to the electrode array to measure the complex impedance between each nearest-neighbor pair of electrodes. Measurement data is exported and analyzed using custom MATLAB scripts.

4.2.6.1 Minimizing parasitics: contact impedance and stray capacitance

Minimizing the effects of parasitic impedance is critical to obtaining accurate measurements of tissue impedance. The main parasitic contributions in this system can be split into two categories: (1) parasitic impedance from the hardware, and (2) contact impedance between the electrode array and the skin. This is illustrated in Figure 4.11. Parasitic impedance in the hardware includes, for example, the series resistance of the routing lines, capacitance associated with connectors, and stray capacitance from the measurement cables; in other words, everything from the output terminals of the measurement instrument (the LCR) up to the electrodes. The contact impedance comes primarily from the capacitance between the electrode and the sample surface; it is expected that this contact impedance will dominate any parasitics from the hardware in this system.

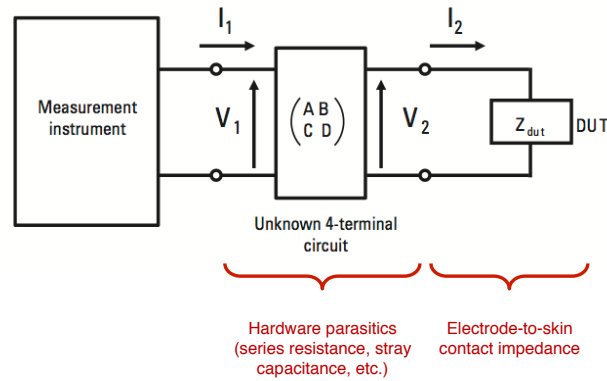


Figure 4.11: Parasitic impedance contributions.

Parasitic impedance can be broken up into two key contributors: (1) series resistance and stray capacitance in the control hardware and array board, and (2) contact impedance from the electrode array to the skin.

Stray capacitance and other measurement parasitics were minimized by choosing minimum-length shielded cables to the LCR meter, properly shielded BNC connections, and noise-minimizing layout and routing techniques in the custom-built control hardware. Though parasitic impedance contributions from the hardware are expected to be minimal, they can be de-embedded from measured data using a procedure in which standard impedance values are measured (“Open”, “Short”, and “Load”) and a correction factor is calculated. The de-embedding procedure is discussed in the Agilent Impedance Measurement Handbook (available from Agilent Technologies), and summarized here. The corrected impedance of a device (or sample) under test based on the circuit in Figure 4.11 is

$$Z_{dut} = \frac{(Z_s - Z_{xm})(Z_{sm} - Z_o)}{(Z_{xm} - Z_o)(Z_s - Z_{sm})} Z_{std} \quad (\text{Equation 4-1})$$

where the terms in Equation 4-1 are defined as

- Z_{dut} Corrected impedance of the device under test (DUT)
- Z_{xm} Measured impedance of the DUT
- Z_o Measured impedance when the measurement terminals are open
- Z_s Measured impedance when the measurement terminals are short
- Z_{sm} Measured impedance of the load device
- Z_{std} True value of the load device

To calculate a correction factor for the impedance sensing array, a $1\text{k}\Omega$ resistor was chosen as the load device; a resistor was soldered onto the rigid PCB array between each individual pair of electrodes. Measurements were also carried out with the electrode array left open (no loads between any of the electrode pairs), and with all electrode pairs shorted. In each configuration, measurements were recorded at frequencies from 100 Hz to 1 MHz. Using these standard measurements, the correction in Equation 4-1 was applied to a set of measurements of a pressure ulcer; the results are shown in Figure 4.12. The difference between the measured and corrected impedance values are negligible for all but the last group of data, which were obtained with a measurement frequency of 1 MHz. It is clear from this

data that at all frequencies below 1MHz, the contribution of parasitics from the hardware are insignificant and no correction is required.

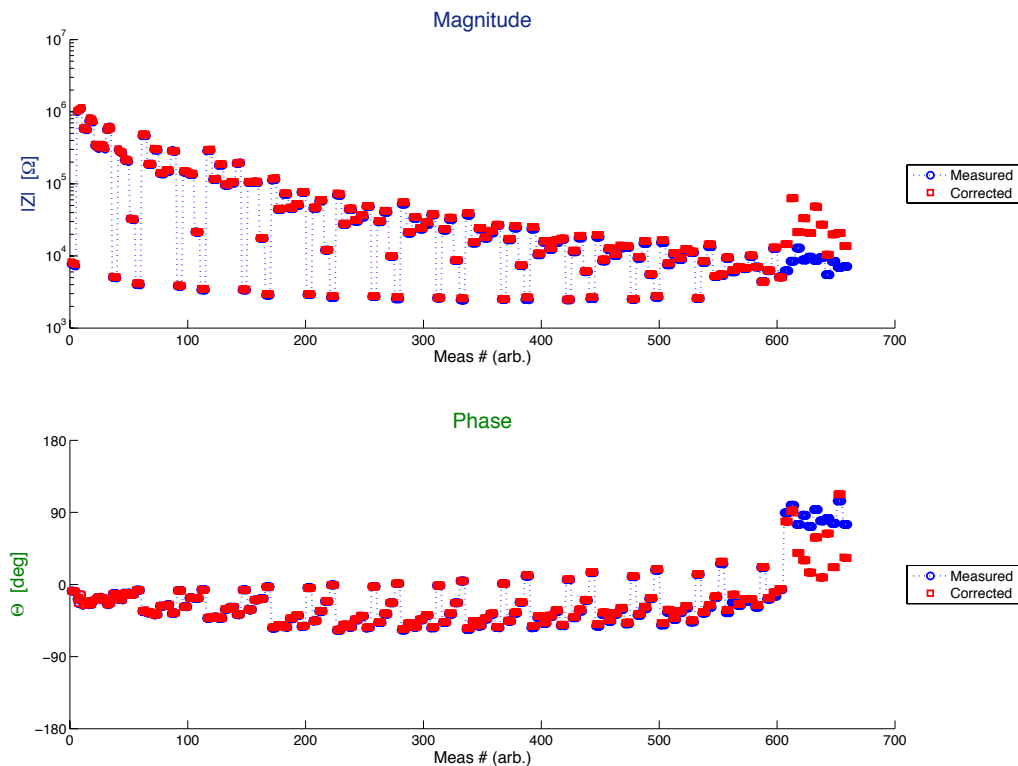


Figure 4.12: De-embedding parasitic impedance from hardware.

Impedance magnitude and phase from a pressure ulcer, where a correction factor has been applied to de-embed the parasitic impedance contributed by the measurement hardware. The measurement frequency varies with measurement number; data beyond measurement number 600 were obtained with a measurement frequency of 1MHz.

Addressing the issue of contact impedance between the electrodes and the sample is more complicated. The contact impedance will vary based on many factors such as the tissue type, the wound topology, and the presence of scab or wound exudate. Thus, the measurement process was optimized to minimize contact impedance by selectively applying high-conductance gel (SignaGel) to each electrode. This process was controlled using a patterned stencil and blade-coating method; the gel can be seen on the electrode array in Figure 4.14. Sufficient pressure was applied during the measurement to ensure the measurement array stayed in contact with the tissue. When the conductive gel bumps were applied, excellent measurement repeatability was observed, indicating well-controlled contact impedance. Figure 4.13 shows the result of two measurements of healthy skin; between measurements, the measurement array was removed, cleaned, and the conductive gel was reapplied. Thus the application of gel to the electrodes sufficiently reduces the contact impedance, allowing accurate, repeatable measurements of the underlying tissue impedance.

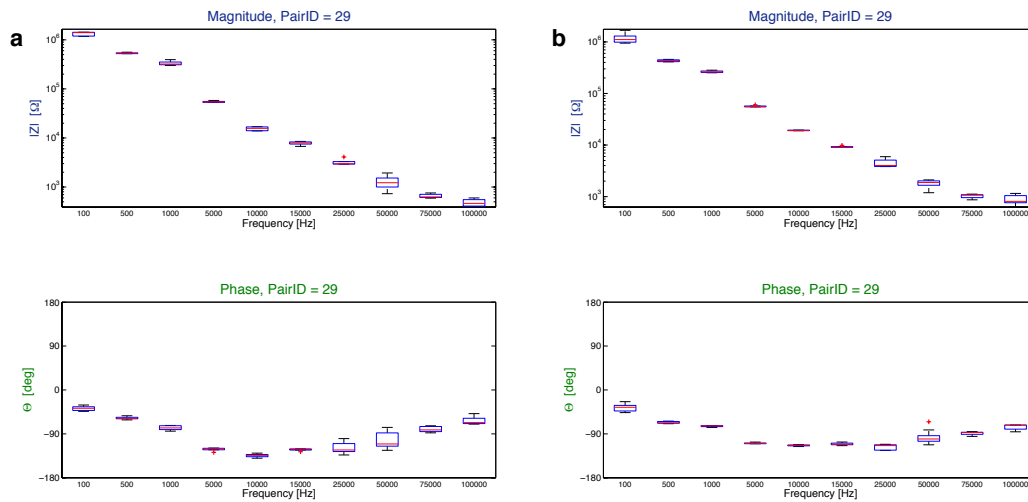


Figure 4.13: Repeatability of impedance measurements with hydrogel.

With conductive hydrogel bumps selectively applied to the electrodes, excellent measurement repeatability is observed. Two impedance measurements of healthy skin are shown (a, b); the electrode array was removed, cleaned, and gel was re-applied between measurements.

4.2.6.2 Mounting the sensor array to the wound

The procedure for mounting the sensing array on wounds is shown in Figure 4.14. A thin Polydimethylsiloxane (PDMS) stencil is first aligned and placed on the flexible array board to allow for selective application of hydrogel (SignaGel Electrode Gel, Parker Laboratories Inc.) to each electrode of the array. The hydrogel ensures adequate electrical contact between each electrode and the skin of the rat. After the stencil is removed, the array is placed carefully on the area of the rat's back to be measured, and secured in place with a transparent Tegaderm™ dressing. Finally, a piece of Coban™ self-adherent wrap is placed around the body of the rat to apply even pressure to the array against the rat's skin. This mounting procedure allows the board to move with the rat's breathing but ensures that it does not shift during measurements. The rigid array board is mounted to the rat in a similar manner.

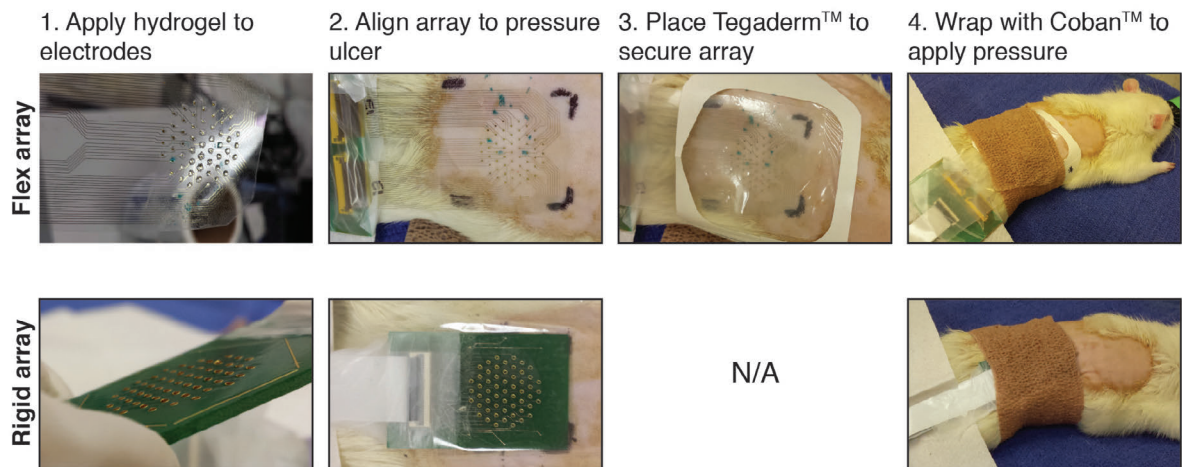


Figure 4.14: Mounting sensor arrays on wounds.

Hydrogel was applied to the electrodes using a stencil-printing process, then the sensor arrays were aligned such that roughly half of the array measured tissue that had pressure applied with magnets, and half of the sensor array measured untreated tissue. Sensor arrays were secured in place with Tegaderm™ dressings and/or Coban™ wraps.

4.2.6.3 Rejecting data from damaged electrode arrays

Repeated use of the flex arrays, including the cleaning and sanitation required between each measurement, eventually resulted in damage to the printed gold lines or the encapsulation layer. The condition of the flexible arrays was tested at least twice daily (before and after wound measurements) by measuring a known impedance value and identifying electrode pairs that reported an incorrect value. The sensor area of the flexible array was submerged in a small beaker of salt water with a concentration of 100 g/L NaCl. The impedance between each pair of electrodes was measured at a single frequency of 1 kHz. If the impedance magnitude between any two electrodes was $< 100 \Omega$, the pair was considered ‘shorted’; this was not the typical failure mechanism, but was occasionally observed. A short in the array was usually a result of a slight misalignment of the contact pads into the connector to the control board. If the impedance magnitude between any electrode pair was greater than $50 \text{ k}\Omega$ (roughly twice the expected value of the salt-water), that pair was considered ‘open’. The most common cause for an open pair was delamination of the gold traces from the plastic substrate. Because of the hexagonal arrangement, one damaged *trace* would result in multiple rejected *pairs* (one for each neighboring electrode). Figure 4.15 shows a measurement of salt water using an array with three ‘open’ electrode pairs: pair ID 17, 18, and 19 (plotted in red).

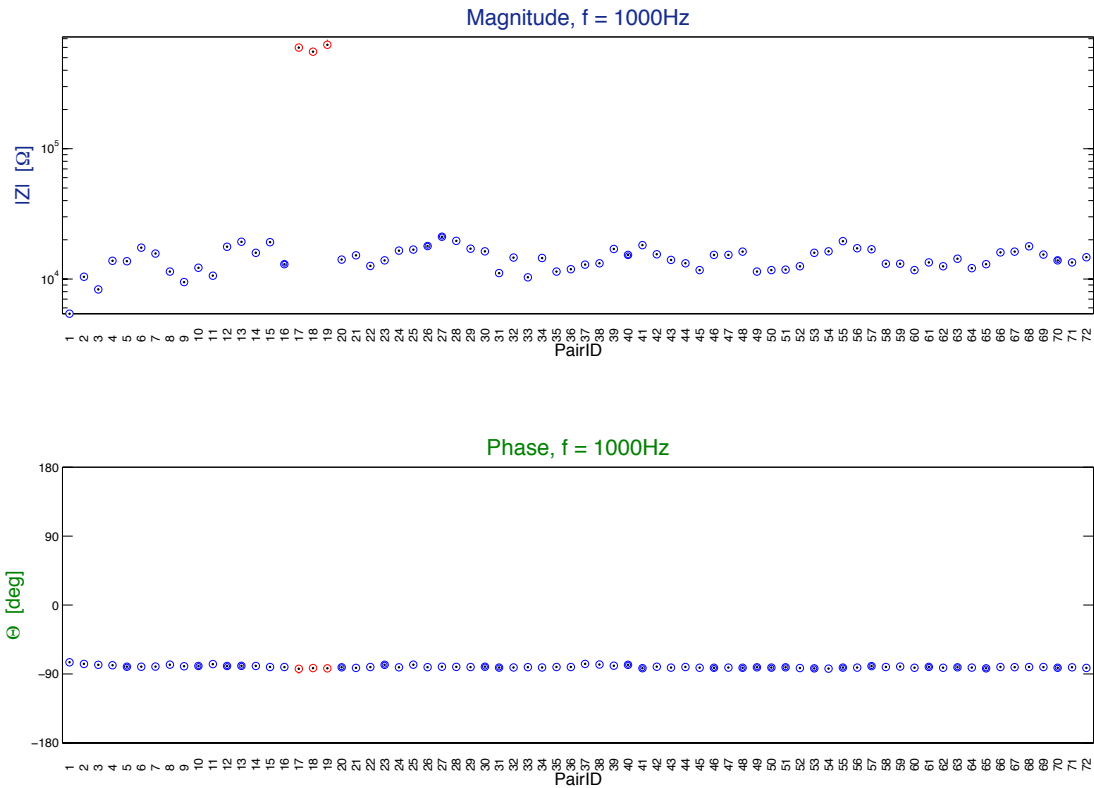


Figure 4.15: Rejected pairs from damaged flexible electrode array.

Repeated use eventually damaged encapsulation or the conductive traces on the flexible electrode arrays. Flex arrays were tested by measuring salt water, and rejecting any pair with impedance magnitude above 50 kΩ. The three rejected pairs in this dataset are plotted in red.

To ensure that only reliable measurements were included in wound analysis, the flexible arrays were tested at least once each day during wound measurements. Any pair of electrodes found to be ‘open’ or ‘short’ was considered a ‘flex reject’ pair. The custom MATLAB scripts that were used for impedance analysis included an automatic filtering procedure that identified ‘flex reject’ pairs based on the salt water test, and then removed those pairs from all impedance measurements made with that particular array. As a result, damaged electrodes caused asymmetrical impedance maps but did not compromise the validity of the data.

4.2.6.4 Four-point vs. two-point measurements, and the “current path problem”

Contact impedance – and the choice of 4-point vs. 2-point impedance measurements to mitigate its impacts – is a critically important issue in bioimpedance analysis. However, trade-offs must be considered when measuring the impedance of heterogeneous complex tissues. In theory, a 4-point probe configuration provides a more accurate impedance measurement than a 2-point probe configuration because the parasitic resistance of the wires is not included in the measurement. In practice, however, 4-point measurements *in vivo* are inherently difficult due to the inhomogeneity of biological tissues.

One of the biggest challenges in measuring the impedance of non-homogeneous materials is the “current path problem”: the path taken by the current between any two electrodes will follow the path of least resistance, rather than the direct path predicted for a homogeneous material. While a 4-point measurement configuration is preferred because of its ability to minimize contact impedance and parasitics, the current path problem is actually *worse* in a 4-point measurement. The measurement of impedance (and the subsequent extraction of material parameters such as resistivity) using a collinear arrangement of 4 electrodes relies on the key assumption that the current driven between the outer pair of electrodes passes through the material uniformly, and thus the voltage measured by the inner sense electrodes can be used to calculate impedance from Ohm’s law (illustrated in Figure 4.16a). If the current takes an unknown path between the drive electrodes instead of passing straight through the material below the sense electrodes (as in Figure 4.16b), the actual voltage generated ($V = I \cdot R$) will be very small and the measured impedance will be erroneously low. In high precision instruments that use an automatic leveling function to ensure linearity in impedance measurements, the problem is worse yet: attempting to maintain a constant voltage at the sense electrodes when the current from the drive electrodes is actually bypassing the tissue beneath the sense electrodes results in an overloading of the drive circuitry and the inability to properly measure impedance. While the current path is still unknown in a 2-point measurement, the impact on the calculated impedance is clearly much less than in 4-point. These issues were observed during early experiments for this study. In Figure 4.16c, the small signal voltage, V_{ac} , as measured by the signal monitor on the LCR meter is plotted for 2pt and 4pt measurements of the same pressure ulcer. In the 4-point data, the red circles indicate the reported V_{ac} values, while the red X’s (arbitrarily plotted as $V_{ac} = 1$) are used to identify measurement overloads where V_{ac} could not be regulated. The electrode array was not moved between measurements; switching between 2-point and 4-point measurements is accomplished by changing the selection of the electrodes in software and using a different connector between the control board and the LCR meter. The automatic level control of the LCR is set such that V_{ac} should be maintained at 100 mV. These data show that the error in the impedance measurement is significantly worse in the 4-point configuration than the 2-point configuration. It was determined that, in practice, using a 2-point configuration with minimized parasitics outweighed the theoretical benefits of a 4-point measurement for this work. It is important to note that the current path problem is not a limitation of this particular device, but a complication inherent in measuring heterogeneous materials such as complex biological tissues. These results demonstrate that the *theoretical* benefits of 4-point measurements do not necessarily bear fruit *in practice*, and that the system as a whole must be designed to minimize confounding effects from various sources.

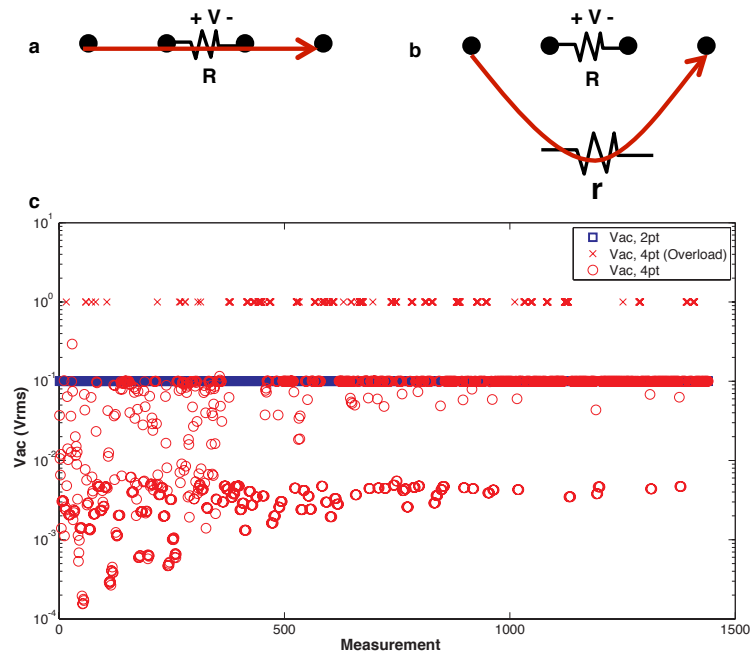


Figure 4.16: Current path problem in 2-pt vs. 4-pt impedance measurements.

(a) The current path during a 4 point measurement in a homogeneous material with 4 collinear electrodes. (b) In a nonhomogeneous material, the current path may not pass directly below the voltage sense electrodes if $r \ll R$. This results in a negligible voltage drop across the sense electrodes, and the measured impedance value is erroneously low. (c) The small signal voltage, V_{ac} , as measured by the signal monitor on the LCR meter is plotted for 2pt and 4pt measurements of the same pressure ulcer. The automatic level control of the LCR is set such that V_{ac} should be maintained at 100 mV. The error in the impedance measurement is worse in the 4-point configuration than the 2-point configuration.

4.3 Results

4.3.1 Multiplexed electrode array maps tissue impedance

An electronic sensing device was designed and implemented that measures spatially-correlated complex impedance *in vivo* using a multiplexed electrode array. The device consists of an electrode array to contact the skin and control hardware that performs impedance spectroscopy across the array. Two versions of the electrode array were developed: 1) a commercial rigid printed circuit board (PCB) with gold-plated electrodes, and 2) a flexible bandage-like array produced using inkjet printing on a plastic substrate. The rigid device was a robust calibration platform that allowed the *method* of detecting pressure ulcers using impedance spectroscopy to be developed while, in parallel, developing the *flexible device* to employ that method *in vivo*. Notably, the rigid array and the flexible array provided similar results (Figure 4.17), and both types were used in the experiments to collect impedance data. A detailed comparison of the specifications of the rigid and flexible arrays is given in . The fabrication process of the printed array is illustrated in Figure 4.18a-b. Gold nanoparticle ink was ink-jet printed on a thin (35 μm) polyethylene naphthalate (PEN)

substrate. Such thin substrates enhance conformity of the printed array, improving electrode-skin contact. A sintering step was required to fuse together gold nanoparticles in the ink to create conductive lines [87]. These conductive lines were encapsulated by spin coating an amorphous fluoropolymer (Cytop); vias over the electrodes were then selectively opened using oxygen plasma etching with a shadow mask. Since several replicate printed arrays were used during animal experiments, minimizing processing variability was essential. The fabrication process proved highly reproducible: for five different arrays we observed low batch-to-batch variation in electrical properties (Figure 4.19). Sheet resistances were obtained with standard deviation of the mean, $\sigma_{\mu, R_s} = 0.01 \text{ } \Omega/\text{sq}$. Printed features demonstrated conductivity of $8.0 \times 10^4 \text{ S cm}^{-1}$ (20% of the bulk conductivity of gold), which is comparable to reported conductivity values in the literature [88]. Mechanical stability of the printed lines was another key concern because the sensor array needed to survive the wear and tear experienced during data collection. Since the arrays were subjected to both bending and torsion, mechanical robustness was tested by torsionally loading an array with angle of twist, $\phi = 30^\circ$. Even after 1,000 cycles, no significant alteration of the printed structures was observed (Figure 4.18d).

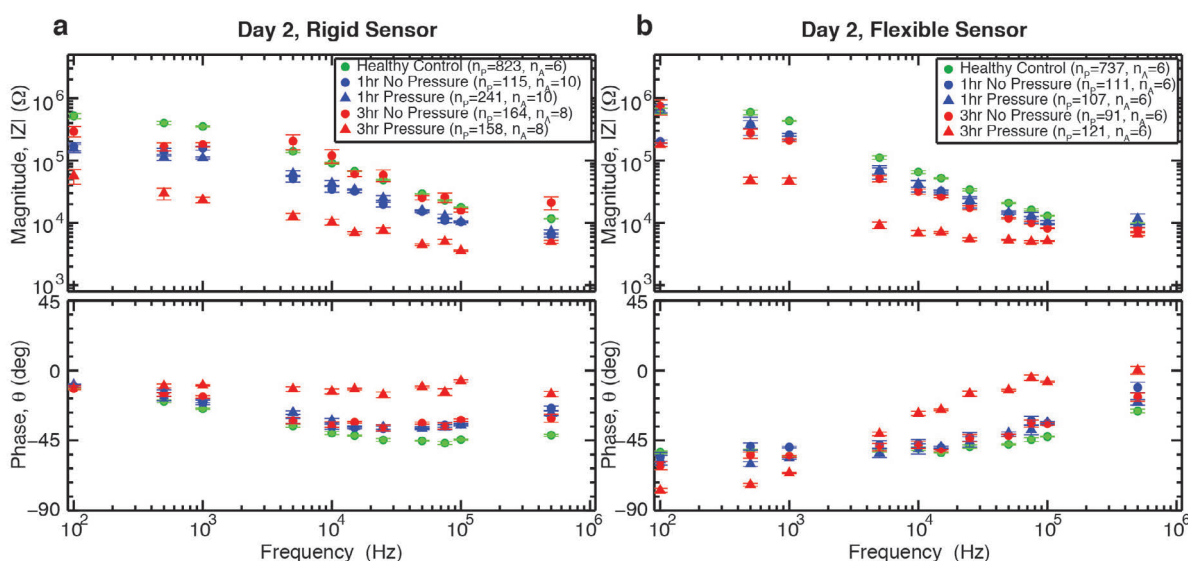


Figure 4.17: Average impedance using rigid vs. flexible array.

Impedance spectra for “Pressure” and “No Pressure” locations of reversible (1hr) and irreversible (3hr) pressure damage, comparing results from the rigid (a) vs flexible (b) sensor array. Impedance data includes all animals in the study measured Day 2. Markers indicate the average data values at each frequency, with error bars showing the standard error of the mean. n_p electrode pairs were used in the calculation of the average values, measured from wounds on n_A animals.

Before the sensing array was placed onto the skin, a thin layer of highly conductive hydrogel was selectively printed onto the electrodes using a silicone stencil; Figure 4.14 illustrates the attachment of the sensor array to the wound. The hydrogel was used on both the rigid and flex arrays to reduce the contact impedance between the electrode and the tissue sample being measured, improving the reliability of the measurements [89]. During operation,

the array control hardware selects two electrodes in the array and performs an impedance measurement across these electrodes using a precision LCR meter; by cycling through pairs, all of the nearest neighbors of the array can be sampled and a map of the impedance measurements can be constructed (Figure 4.18c). “Four-point” measurements were also performed but were found to be much harder to correlate to wound state (see discussion in section 4.2.6.4). Registration marks were stained onto the skin to establish the position of the electrodes with respect to the pressure ulcer being measured.

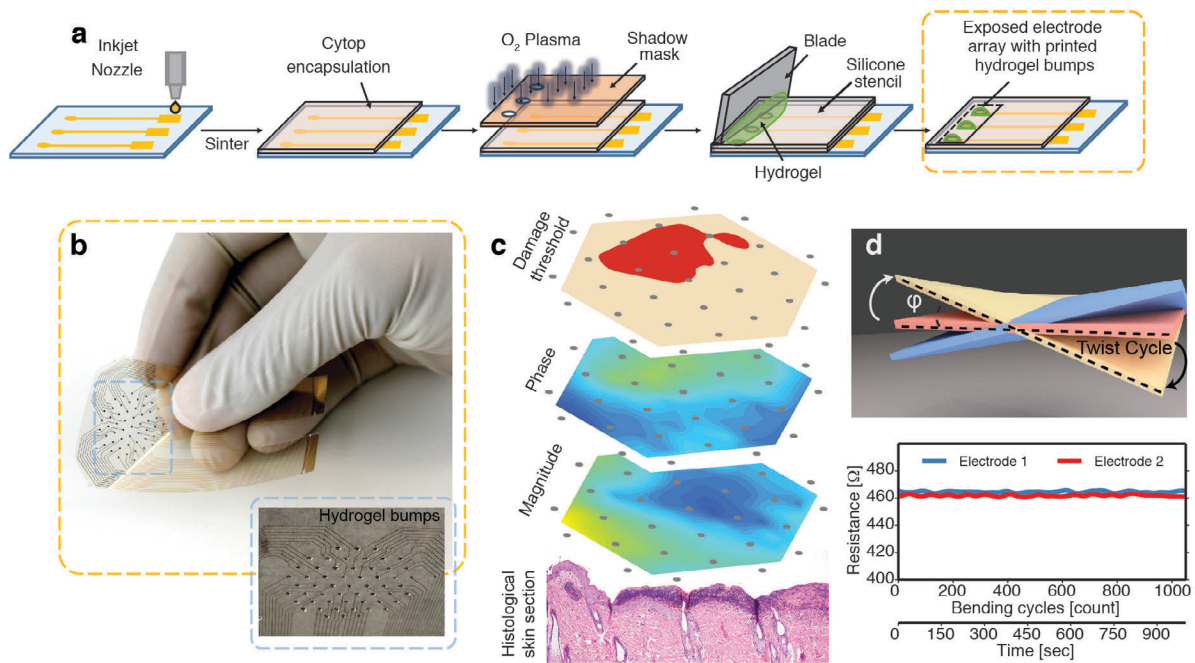


Figure 4.18: Flexible electrode array fabrication and characterization.

a, Fabrication flow for the ink-jet printed flexible electrode array. **b**, An ink-jet printed array, showing the hexagonal configuration of 55 equally-spaced gold electrodes; inset shows printed hydrogel bumps on the fabricated array. **c**, Schematic representation of the device operation. The array is placed on a wound *in vivo* and the electrical impedance is collected for each pair of neighboring electrodes. A map of impedance magnitude, phase angle, and damage threshold (indicated here in red) are constructed based on the location of each measurement pair. **d**, Mechanical robustness testing by torsionally loading the array with angle of twist $\phi = 30^\circ$, with no significant change in line resistance after 1000 twist cycles.

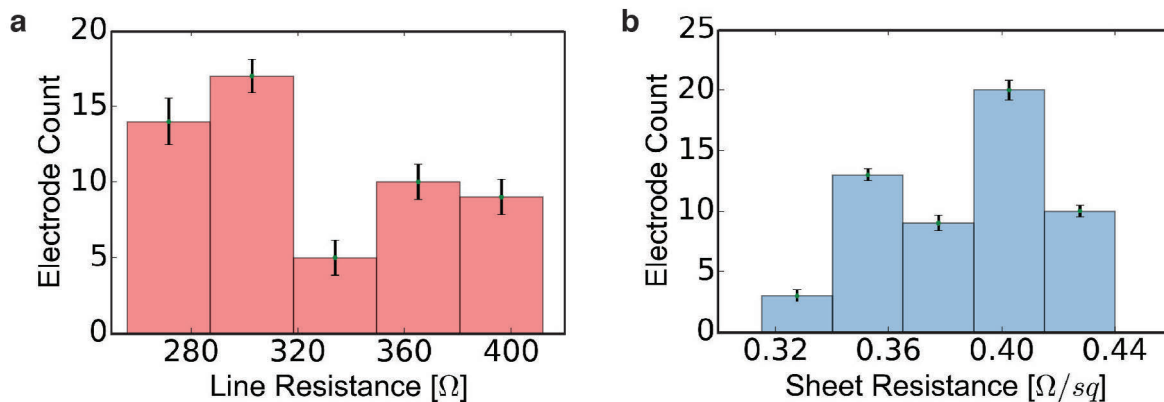


Figure 4.19: Reproducibility of the inkjet printing process.

Histograms show line resistance (a) and sheet resistance (b) of the 55 printed lines of over 5 different printed arrays. Error bars represent the standard deviation across different arrays.

4.3.2 Impedance spectrum correlates to tissue health

To create pressure ulcers, rats were sedated and the dorsal body hair was shaved, and depilated with Nair to provide bare skin for impedance measurements. After the area was cleaned, the skin was gently tented up and placed between two disc-shaped magnets [90]. The animals returned to normal activity with the magnets in place for 1 or 3 hours, at which point they were sedated and the magnets removed. Eleven of the twelve animals used in this study received the 1 hour treatment, and nine of the twelve received the 3 hour treatment. Using fluorescence angiography to image real-time blood flow in the tissue (Figure 4.9), we observed that relieving the pressure initially resulted in increased perfusion (reactive hyperemia) [69], [91] as the blood returned to the affected tissue. When blood returns to the ischemic tissue, it produces reactive oxygen species and free radicals that can accelerate cell death [92], [93]. In our model, one hour of pressure produced mild reversible tissue damage, and three hours of pressure produced more severe irreversible damage. Following the ischemic event, we tracked the wounds for at least three days using impedance spectroscopy.

The system measured impedance using a 100 mV_{RMS} constant voltage test signal at frequencies between $10^2 - 10^6$ Hz across all nearest neighbor electrode pairs on the array; data from a single representative wound in the 3-hour ischemia group is shown in Figure 4.20. Across all animals in the 3-hour group ($n=9$), the impedance spectra for areas developing pressure ulcers were clearly distinguishable by Day 3 (or earlier) from spectra for areas that were healthy. Qualitatively, wounded areas showed a decrease in impedance magnitude and phase angles closer to zero. The tissue appeared less capacitive and more conductive, consistent with a loss of cell membrane integrity [75] (Figure 4.20a). In the impedance spectra (Figure 4.20b), the dominant pole for the wounded tissue was at a lower frequency than for the healthy tissue. To determine specific threshold values of impedance magnitude and phase that defined “damaged tissue”, impedance spectra were analyzed that had been collected with the flexible electrode array from fourteen wounds on eight rats. A contrast optimization process was then used that identified 15 kHz as the frequency at which the maximum difference was observed in impedance between damaged and non-damaged tissue.

From this analysis, a magnitude value of $|Z| = 6 \text{ k}\Omega$ and a phase window of $-30^\circ \leq \theta \leq -10^\circ$ measured at 15 kHz was found to be an effective threshold for identifying damaged tissue while avoiding false positive readings.

Due to the differences in materials and assembly of the ink-jet printed flexible electrode array and the rigid calibration array as detailed previously in Table 4–1, the threshold for detecting damaged tissue was adjusted depending on which electrode array was used to record impedance data. Qualitatively, the flexible arrays had as a slightly higher line resistance and an additional capacitive contribution from one extra connector between the flexible array and the control hardware, both of which need to be taken into account. Threshold values indicating tissue damage were determined separately for the flexible and rigid arrays, and were found to be as follows:

Flexible electrode array: $|Z| \leq 6 \text{ k}\Omega$ and $-35^\circ \leq \theta \leq -10^\circ$

Rigid calibration array: $|Z| \leq 5 \text{ k}\Omega$ and $-5^\circ \leq \theta \leq 10^\circ$

The same threshold values were applied to all wounds, regardless of whether they belonged to the 1-hour or 3-hour treatment group. Any pair of electrodes whose magnitude was below the threshold *and* whose phase value fell within the specified window was labeled as ‘damaged tissue’. In other words, the term “damage” indicates regions where impedance data predicts tissue damage, whereas the term “pressure” indicates data from any area of tissue subjected to magnet pressure. The phase requirement was included to make the damage parameter less susceptible to minor animal-to-animal skin variations than using magnitude alone (such as skin thickness, hydration status, etc.), and thus improve the reliability of tissue classification. Spatial impedance data can thus be translated into a map of the tissue damage parameter that differentiates healthy tissue from a wound. As shown in Figure 4.20, by Day 2 (the day following the ischemic event) the impedance sensor identified an area of tissue damage that correlates with the placement of the magnets. Not surprisingly, tissue damage within the pressure area is not uniform; an ulcer can be seen in the lower right region of the pressure area in the Day 3 image in Figure 4.20a, and this region is also highlighted in the map of the damage threshold. The analysis shown in Figure 4.20a-b was carried out for each wound on each animal in the study, and all animals in the 3-hour treatment group produced similar results. The repeatability of the results across wounds on many animals is shown in Figure 4.20c. Here the impedance spectra for reversible (1hr) and irreversible (3hr) pressure damage measured with the flexible array on Day 2 were averaged over all animals in the study, excluding those sacrificed prior to Day 2. For each wound, each electrode pair was labeled either as ‘Pressure’ or ‘No Pressure’ depending on whether or not the electrodes measured tissue where pressure had been applied. (All pairs spanning the boundary of ‘pressure/no pressure’ were omitted.) The reduction in impedance magnitude and a phase angle closer to zero is clearly evident in this ensemble data for the 3 hour pressure group.

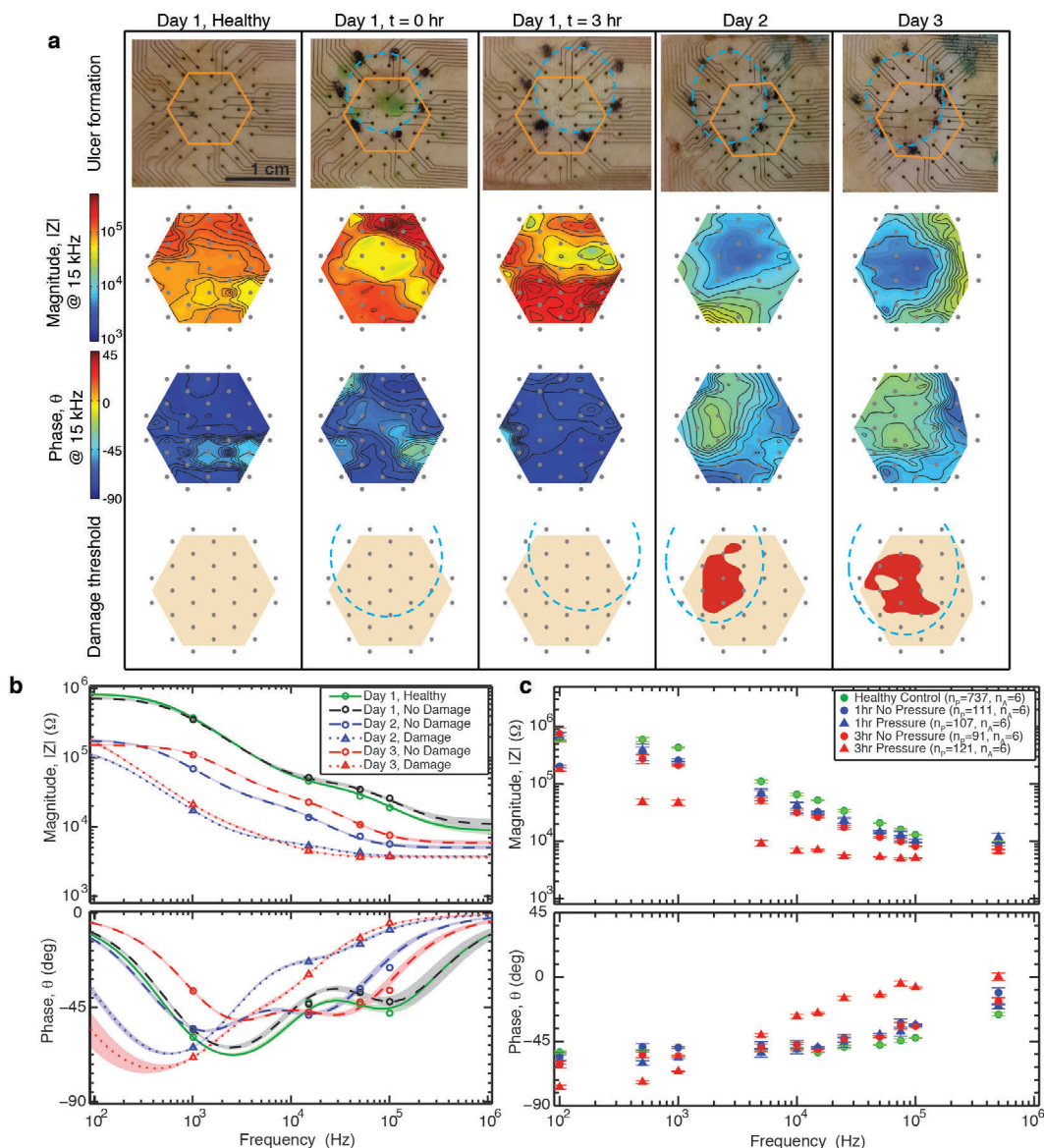


Figure 4.20: Impedance spectrum correlates to severe, irreversible tissue damage.

a, The progression of a representative example of irreversible tissue damage created with a 3-hour ischemia cycle is shown on Days 1-3. On Day 1, *Healthy* is a control measurement taken prior to ulcer formation, $t = 0$ hr corresponds to measurements immediately following magnet removal, and $t = 3$ hr corresponds to measurements after 3 hours of reperfusion. *Row 1*: The transparent, flexible electrode array is in place over the wound, and the pressure area is indicated with a dashed blue circle. The outer ring of electrodes on the array was not used for the 2-point impedance measurements shown here; the hexagon overlaid on the image outlines the area corresponding to the impedance maps. Scale bar (1 cm) applies to all wound photos. *Rows 2-3*: Impedance magnitude and phase angle measured across nearest-neighbor pairs with the flexible electrode array at a frequency of 15 kHz. The asymmetry in the surface map on Day 3 is due to the rejection of one broken electrode. *Row 4*: The damage threshold is determined from the magnitude and phase data at each pair, and mapped across the array. Red indicates tissue damage. On Days 2-3, a region of tissue damage is detected that clearly correlates with the location of the developing pressure ulcer. **b**, Impedance spectra for the wound shown in **a** of healthy skin prior to applying pressure, ‘No damage’ regions on Days 1-

3, and ‘Damage’ regions on Days 2-3. A representative electrode pair was selected from each region. The markers indicate the measured data values, while the lines and the shaded regions indicate the estimated transfer function and the 95% fit confidence interval, respectively. **c**, Impedance spectra for “Pressure” and “No Pressure” locations of reversible (1hr) and irreversible (3hr) pressure damage measured with the flexible array on Day 2, averaged over all animals in the study. Markers indicate the average data values at each frequency, with error bars showing the standard error of the mean. n_p electrode pairs went into the calculation of the average values, measured from wounds on n_A animals.

4.3.3 Impedance spectroscopy identifies damage that is not visible

The ability to detect and monitor a pressure ulcer that has already formed on a patient is valuable, but a key advantage of using impedance spectroscopy to detect pressure ulcers is early detection of tissue damage. Mild, reversible pressure damage was created using a 1-hour ischemia cycle (as opposed to the 3 hour ischemia cycle used above), then monitored with impedance measurements for three days. The skin appeared slightly white during reperfusion, but no visible ulcer developed in the following nine days, indicating that any pressure-induced damage was truly reversible.

The impedance measurements reveal a more nuanced story. Using the same impedance thresholds to detect damage that were employed for irreversible damage, the impedance sensor detected damaged tissue in the region of pressure application in just over half of the cases studied (6 out of 11 animals using the rigid array, and 5 out of 7 animals using the flexible array), again with no false positive results (Figure 4.21). Due to the expected animal-to-animal variation, the combination of pressure and duration used in the 1-hour cases was sufficient to create tissue damage in some, but not all, animals. Histology of skin samples with 1 hour of ischemia confirmed that the tissue was not damaged in all cases. Variation in damage severity was also observed in 3 hour ischemia cases, with some ulcers reaching a stage II classification while others with the same treatment were only classified as a stage I ulcer [68]. This animal-to-animal variation observed for the 1-hour pressure cases (as well as the non-uniform damage within the area of pressure application) explains why averaging the impedance of “Pressure” and “No Pressure” areas over many animals (Figure 4.20c) obscures a meaningful result for the reversible damage case. Three outcomes were observed in response to applied pressure (Figure 4.22): 1) severe, irreversible pressure damage is sustained creating a visible ulcer that is also detected with impedance spectroscopy (panel **A**); 2) mild pressure damage is sustained that is not visible to the naked eye, but can be detected using impedance spectroscopy (panel **B**); and 3) pressure is not sufficient to damage the tissue and, correspondingly, the impedance sensor does not indicate damage (panel **C**). Figure 4.22 also demonstrates that the rigid calibration and flexible printed sensor arrays produced similar results, but that the rigid arrays produced more complete damage maps because they were more robust during multiple measurement-disinfection cycles. The second observation – detecting changes in the tissue that cannot be seen by eye – demonstrates the sensitivity of impedance spectroscopy to physiological changes associated with ulcers and its applicability as an early detection method for pressure ulcers.

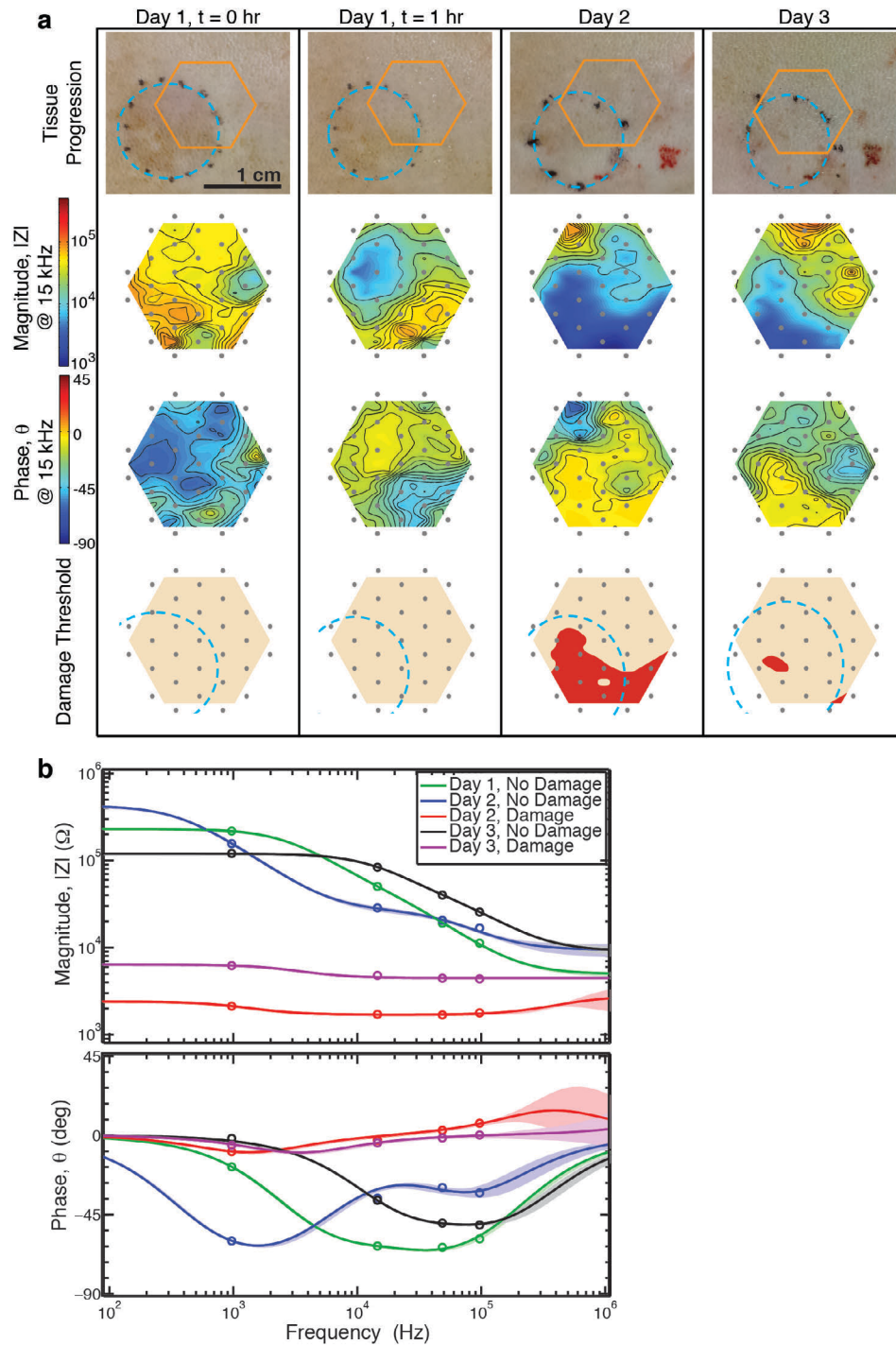


Figure 4.21: Impedance maps identify mild, reversible pressure damage.

a, The progression of reversible pressure damage created with a 1-hour ischemia cycle is shown on Days 1-3. Dashed grey circles indicate where the pressure was applied, and dots represent the placement of the electrodes. Slight discoloration of the skin is observed immediately after removing the magnets, but no ulcer develops. Impedance magnitude and phase were measured with the rigid PCB array. Damage is detected electrically on Day 2 even with no visible evidence of the pressure damage, demonstrating the early detection capability

of the device. (The small abrasion to the right of the measured area was irritation from hair removal.) Only a small region of damage remains on Day 3. Scale bar (1 cm) applies to all wound photos. **b**, A Bode diagram showing the impedance magnitude and phase vs frequency of ‘No damage’ and ‘Damage’ regions on Days 1-3. A representative electrode pair was selected from each region. The circle markers indicate the measured data values, while the lines and the shaded regions indicate the estimated transfer function and the 95% fit confidence interval, respectively.

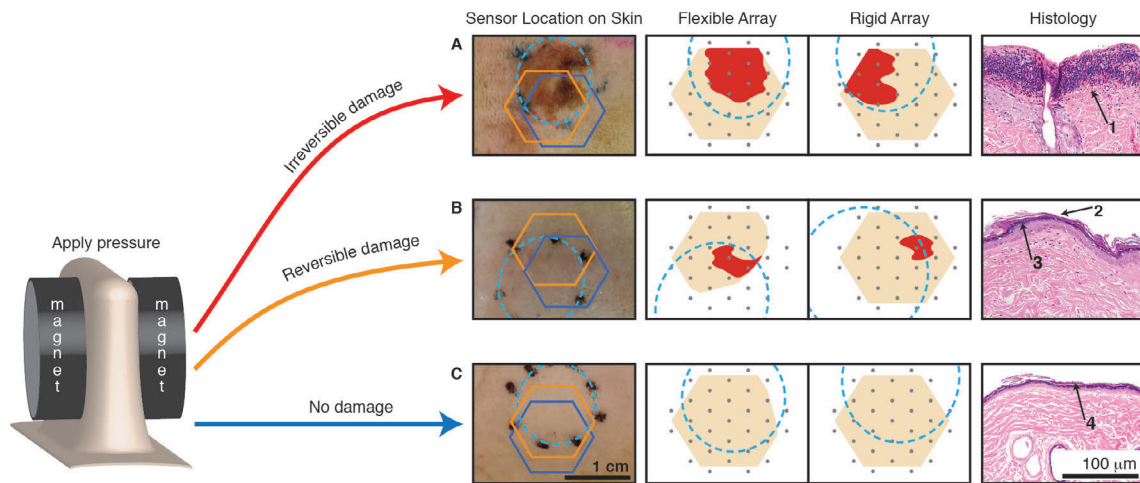


Figure 4.22: Three outcomes observed for pressure-induced tissue damage.

Magnets were used to create a pressure ulcer model on rats *in vivo*. Three outcomes were observed, influenced by the amount of pressure, the duration of treatment, and animal-to-animal variation: **A**) Irreversible damage was detected both visually and electrically; **B**) Reversible damage was detected electrically but not visually; **C**) No damage was detected visually or electrically. Histological analysis indicated loss of epidermis (1) and ulceration when there was irreversible tissue damage, hyperkeratosis (2) and hypergranulosis (3) when the damage was measurable but reversible, and focal hyperkeratosis (4) in the scenario where no damage is detected. Panel **B** illustrates the sensitivity of the impedance sensor to identify damaged tissue, providing an early detection mechanism for pressure ulcers. Representative wound images with sensor locations indicated, damage parameter maps obtained from those wounds using flexible and rigid sensor arrays, and histology results are shown for each scenario. Dashed light blue circles indicate where the pressure was applied to the skin, orange and dark blue hexagons indicate the location of the flexible and rigid arrays on the wound, respectively, and grey dots represent the electrodes. The scale bar is 1 cm for wound photos and 100 μm for histology images.

4.3.4 Cell membrane disruption correlates with impedance change

Histological cross-sections performed at various time points throughout the study (Figure 4.22 and Figure 4.23) support the hypothesis that the alteration of cell membranes and tissue structure causes the observed impedance changes. Histological analysis was performed on tissue samples from reversible (1 hour of ischemia) and irreversible (3 hours of ischemia) pressure groups. Histopathologic examination of the hematoxylin and eosin-stained sections showed focal compact hyperkeratosis and focal hypergranulosis in the area of magnet application in both 1 hour and 3 hour groups. The skin samples from the 1 hour application

group showed no evidence of skin ulceration, while all samples taken after the 3 hour magnet application period demonstrated ulceration. These lesions showed overlying necroinflammatory debris with serum crust, focal loss of epidermis, alteration of underlying collagen and had sparse to moderate amounts of mixed inflammatory infiltrate composed predominantly of lymphocytes and neutrophils. In some cases, the inflammatory infiltrate involved deeper dermis, skeletal muscle and fascia. These histological findings were consistent with the changes in tissue structure that are expected to cause changes in impedance [75].

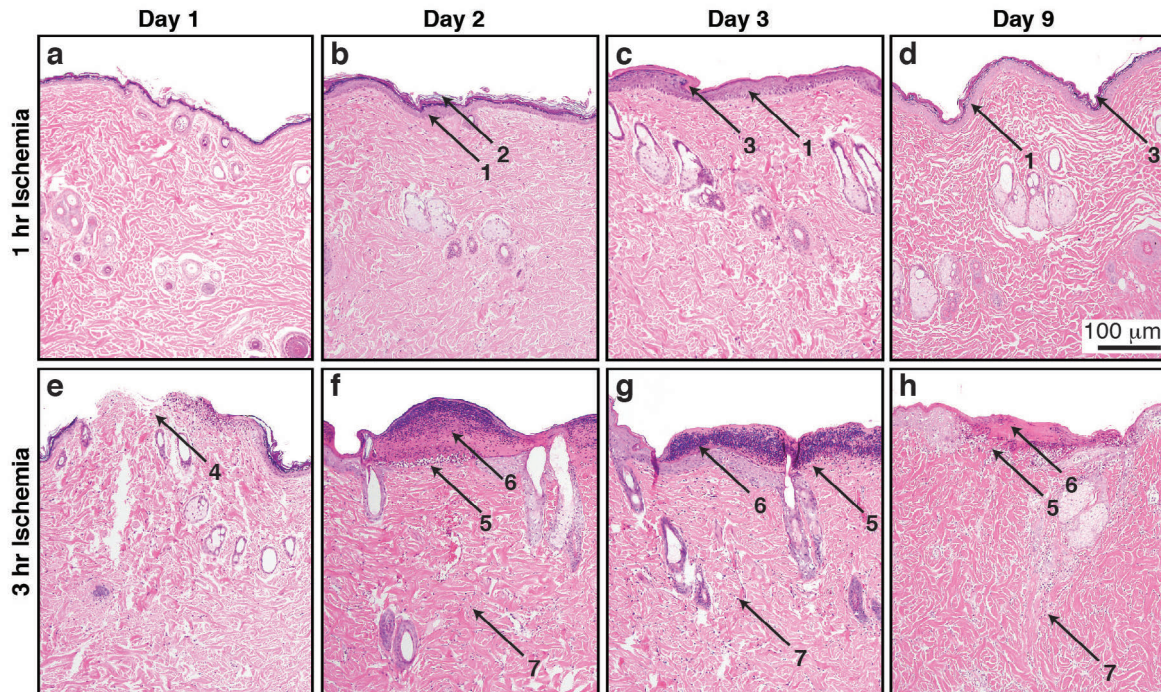


Figure 4.23: Histology of skin samples.

Skin samples were collected for histology on days 1, 2, 3 and 9, and processed with hematoxylin and eosin staining. Samples a-d were taken from animals in the 1-hour pressure treatment group, while samples e-h were taken from animals in the 3-hour pressure treatment group. All images were taken with 100x magnification. **a**, Normal-looking dermis and epidermis. **b**, No signs of ulceration. Normal epidermis (1) with orthokeratosis (2). **c-d**, No signs of ulceration. Normal epidermis (1) with compact hyperkeratosis (3). **e**, Early small ulcer (4). **f-h**, Loss of epidermis (5) and necroinflammatory debris (scab, 6) with inflammation (neutrophils and lymphocytes, 7) deeper in the dermis. Scale bar (100 µm) applies to all images.

4.3.5 Applications extend beyond pressure ulcers

In addition to the detection of pressure ulcers, this device also has the ability to track the state of open skin wounds, such as abrasions, open sores, and lacerations (see Figure 4.24). An open wound was created by surgically excising a small (roughly 1 cm) skin section from the back of the rat using a scalpel ($n=1$). Impedance measurements were taken with both the rigid and flexible array boards on days 1, 2, 3, and 5 to track the progress of the wound

healing. These measurements confirm that the impedance sensor can identify not only the size and shape of an excision by determining the border of the wound, but can also differentiate between a moist wound (exposed wound bed, potentially pus, etc.) and a healing, scab-covered wound. On Day 1, immediately after the wound was created, impedance in the wound bed was significantly lower than the surrounding tissue due to the excess of wound exudate in the wound. Impedance remains lower in the wound bed until day 3 when the scab starts to form. The scabbed area is characterized by higher impedance due to the decrease in ionic exudate and the presence of high resistance fibrin plugs.

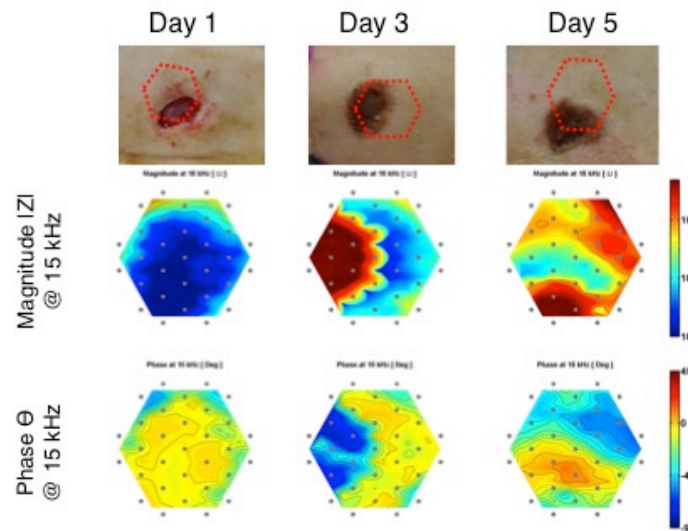


Figure 4.24: Impedance measurements of open wounds.

Impedance of an open, excisional wound was monitored over the course of 5 days using the rigid array board. Initially, on Day 1, the wound area exhibited significantly lower impedance due to the presence of conductive wound exudate. After Day 3, the scabbed region demonstrated higher impedance than the surrounding tissue.

With a slight change in instrumentation, the same device can also be used to measure voltage at each electrode with respect to a common reference, creating a map of the voltage and endogenous electric field across the wound. It is well known that cells can be directed to migrate with an applied electric field [94]–[98], and there is evidence, though somewhat controversial, that applying an electric field may assist in the healing process [99]. The device demonstrated here provides the capability to test the extension of these theories from cells to complex tissues *in vivo*. Thus, it could be adapted to sense the endogenous field, apply an external field, and monitor the response of the tissue to the stimulus, providing much-needed evidence regarding the efficacy of electrical stimulation for healing chronic wounds.

4.4 Conclusions

In this chapter, a non-invasive electrical sensing device was presented that utilizes impedance spectroscopy to detect pressure-induced tissue damage in a rat model *in vivo*. The sensitivity of this detection method and the robustness of the calculated damage parameter are

sufficient to detect mild, reversible physiological changes that are not apparent by visual inspection. While the specific threshold values that indicated tissue damage in this study demonstrate the capability of impedance spectroscopy as a technique for early detection of tissue wounds, additional studies will be needed to determine clinically relevant threshold values in human patients. A commercial device with this capability could have a dramatic impact on the standard of care for pressure ulcers. Disease prevention is a well-recognized approach in medicine; providing an early detection mechanism for pressure damage would allow caregivers to respond proactively, preventing any further damage to the tissue and enabling close monitoring of tissue condition. Further, the variation in wound severity that was observed for a given treatment (which is not unique to this model) strongly supports the value of a device that directly measures the status of the tissue, rather than relying on secondary measurements such as applied pressure. If the subtle changes in tissue are detected early enough, as demonstrated here in the case of the reversible 1 hour pressure damage, the formation of pressure ulcers in some patients may be prevented entirely, greatly reducing health care costs and improving patient outcomes.

Chapter 5: Conclusions & Future Outlook

Outlook

5.1 Summary

Flexible electronics are poised to dramatically change the way that electronic devices are integrated into our everyday lives. Lightweight, flexible form factors will allow new types of displays, sensors, and wearable devices to enter the market. Progress in flexible electronics will continue to be fueled by further advances in the materials and manufacturing methods that underlie their success. In particular, the performance of solution-processed electronic materials employing additive manufacturing techniques will continue to improve, and the cost will continue to drop as a result of high-throughput processing. The industries most likely to exploit these technologies and help bring them to market are next-generation displays and biomedical sensors because they can leverage the low cost per unit area of printed electronics. In this work, solution-processed nanomaterials are studied with an eye towards advanced displays and biological sensing applications.

Metal oxide semiconductor materials were investigated as a candidate for high-performance, solution-processed electronics. Metal oxides (In_2O_3 , ZnO , SnO_2 , etc) are a particularly interesting class of material because they exhibit excellent mobility (an order of magnitude higher than amorphous silicon) even in an amorphous or disordered state. The solution processed electronic materials utilized in this work can be generally categorized as sol-gels and colloidal nanocrystal solutions. Sol-gel precursors typically consist of a metal element surrounded by alkoxide, nitrate or chloride ligands. Precursor solutions are deposited onto a substrate and converted to a dense, thin film with a heat treatment. Colloidal nanocrystals, in contrast, are synthesized in a solution prior to deposition onto a substrate. Nanocrystals offer many benefits over sol-gels, including fine control of the shape, size,

composition, and surface properties. Furthermore, nanocrystal inks are often more stable than sol-gel precursor solutions; the instabilities in sol-gel precursor inks pose challenges both in terms of device uniformity and large-scale manufacturability. Sol-gels and colloidal nanocrystals can both produce high-performance solution-processed TFTs, but the work in this dissertation is primarily focused on colloidal nanocrystal inks. In this work, colloidal nanocrystal thin films undergo a heat treatment to remove the surfactants from the nanocrystal surfaces, allowing the particles to form a high-quality semiconductor channel material. Semiconductor nanocrystals are preferred not because the quantum confinement effects are being exploited, but rather as a way to combine the benefits of inorganic materials with low-cost solution-processing manufacturing methods.

The synthesis of indium oxide nanocrystals was studied, with the goal of obtaining a high-performance solution-processed semiconductor material. Colloidal In_2O_3 nanocrystals were prepared using an air-free synthesis with indium acetylacetonate as the metal precursor, and oleylamine as the solvent and ligand. The synthetic procedure was varied, and the impacts of those variations on the nanocrystal ink and the performance of solution-processed TFTs was examined. Proper degassing of the reaction and optimizing the reaction temperature resulted in nanocrystals that form air-stable, high-performance indium oxide TFTs, the performance of which far exceeds previous reports of indium oxide nanocrystal transistors.

The impact of In_2O_3 nanocrystal TFT fabrication conditions on device performance was investigated in a multifactorial experiment. The annealing temperature, annealing ambient, and the gate dielectric were varied, and TFTs were fabricated at each condition. The choice of a high- κ gate dielectric (specifically, ZrO_2) and a higher annealing temperature had the most significant positive effect on the performance of TFTs. Surprisingly, though a dramatic difference in TFT mobility was observed, there was no change in the average crystallite size in the channel with different annealing conditions or different gate dielectric materials. The field-effect mobility was compared across devices after taking into account the effective transverse electric field in the channel, and TFTs utilizing high- κ gate dielectrics reached higher mobilities than the devices on SiO_2 . These results indicate that the transport in In_2O_3 nanocrystal TFTs is not limited by the crystallinity, and that the mobility boost cannot be attributed strictly to the higher fields achieved with high- κ gate oxides. In this work, In_2O_3 nanocrystal inks were shown to be a promising pathway towards high-performance, air-stable, solution-processed transistors.

One particularly promising application for flexible electronics is bio-integrated devices, from biomedical sensing devices to wearable fitness monitors. Devices for biological applications can build on the vast materials development work in the printed electronics community, but additional studies must be carried out to ensure biocompatibility of the materials and devices. Fortunately, many of the metal oxide materials that are being pursued are biocompatible in their bulk form, and are thus promising candidates for biocompatible printed electronics. High-performance TFTs made from likely biocompatible materials were demonstrated in this work, as well as the ability to dissolve such materials in a simulated body environment. However, nanomaterials have unique concerns in terms of their biocompatibility. Recent research indicates that even materials that are safe in their bulk form

may be hazardous in the nanosize regime, and, further, solution-processed films may have residual contaminants from the ink that alters the toxicity of the material. *In vitro* toxicity tests are proposed that will push the field of bio-integrated flexible electronics devices forward.

The merit of flexible biological sensors was demonstrated with a “smart bandage” prototype. A flexible, non-invasive electrical sensing device was developed that utilizes impedance spectroscopy to detect pressure-induced tissue damage in a rat model *in vivo*. A flexible inkjet-printed 2D electrode array measured the complex impedance of the tissue at many points, then the impedance data was analyzed and presented in a spatially-correlated manner that creates a “map” of the wound. Impedance was found to be strongly correlated with tissue health: the impedance of pressure-damaged tissue has lower magnitude and a phase angle closer to zero. The data support the hypothesis that the change in impedance can be attributed to changes in the integrity of the cell membrane. The sensitivity of this detection method and the robustness of the calculated damage parameter are sufficient to detect mild, reversible physiological changes that are not apparent by visual inspection. The impedance sensor provides objective information about the physiological state of the tissue that could enable early detection (and possibly prevention) or pressure ulcers. A commercial device with this capability could have a dramatic impact on the standard of care for pressure ulcers.

5.2 Suggested Future Work

In this work, solution-processed nanomaterials were investigated for applications in displays and bioelectronics. In particular, an indium oxide nanocrystal semiconductor ink was studied in detail. Further research in the following areas will provide a better fundamental understanding of the device physics in these materials, and thus may lead to further improvements in TFT performance and new applications for solution-processed electronics:

- **Tuning semiconductor material properties via controlled incorporation of various metal cations:** Studies of ternary/quaternary systems indicate that metal cations may contribute different characteristics to the material. For example, indium content increases TFT mobility, but often requires a larger negative bias to fully turn the device off. Zinc stabilizes an amorphous film and can contribute to conduction. Gallium suppresses carrier generation by preventing oxygen vacancies. Synthesizing In_2O_3 , ZnO , Ga_2O_3 nanoparticles separately, then combining them to make an IGZO nanoparticle ink would allow the composition of semiconductor thin films to be tuned by mixing different proportions of metal oxide nanocrystals into the ink. This approach is more promising than a mixed sol-gel route because the size, shape, crystallinity, and phase of each oxide material can be controlled independently.
- **Determine the density of states in the bandgap in solution-processed In_2O_3 :** Conduction in disordered semiconductors is strongly dependent on the density

and distribution of states in the bandgap. Measuring the field effect conductance of In_2O_3 TFTs is one possible method to map out the density of states (DOS). The conductance is measured as a function of gate voltage (V_G) and temperature, then the flat-band voltage (V_{FB}), the conductance activation energy (ΔE), and surface potential $\Psi_s(V_G)$ can be determined. Using V_{FB} and $\Psi_s(V_G)$, the DOS in the bandgap can be calculated. Performing this analysis on devices made with ZrO_2 and SiO_2 gate dielectrics may help to explain the increase in mobility reported in chapter 2.

- **Compare HfO_2 gate dielectric to ZrO_2 in metal oxide TFTs:** Metal oxide TFTs in this work and in work from many other groups have exhibited higher mobility when ZrO_2 gate dielectric is employed. ALD films of HfO_2 have a dielectric constant close to that of ALD ZrO_2 (17 vs. 21). Thus a comparison of metal oxide TFT performance using HfO_2 vs. ZrO_2 would enable a distinction to be clearly made between the effects of a high dielectric constant and the ZrO_2 material in particular. This may help to elucidate the physical mechanism of the improved mobility.

In parallel with the materials development work outlined above, the following studies will build on the newly-developed impedance sensing platform and continue to advance the biomedical applications for flexible electronics:

- **Study the endogenous and applied wound fields during healing:** There is much discussion among the wound healing community about the role of the endogenous (internal) electric field in a healing wound, as well as the efficacy of applied (external) electric fields to promote and speed wound healing. With minor changes in the design and instrumentation of the impedance sensor, the endogenous electric field that is naturally developed at a wound site could be measured and external fields could be applied using the electrode array. The impedance sensor could then be used to monitor the state of the healing wound. This study would provide critical knowledge about the fundamental role of electric fields in wound healing.
- **Investigate the ability of the impedance sensor to detect tumors:** Electrical impedance has recently been pursued as a potential screening technique for breast cancer. The standard screening method, x-ray mammography, has high sensitivity but low specificity, resulting in many false positive screening results. The two-dimensional impedance sensing array developed in this work could be an ideal non-invasive, early detection platform for identifying early stage tumors. By selecting electrodes with varied spacing, the penetration depth of the impedance measurement may be able to be controlled such that a three-dimensional impedance map could identify the structure of breast tissue.

- **Explore extended gate field-effect transistors (EGFETs) based on amorphous metal oxide semiconductors as a platform for biological sensing:** Thin-film EGFET sensors printed on a flexible substrate could be a cost-effective biological sensing platform; integrating sensors with a passive RFID tag and implanting the device subcutaneously could, for example, provide a minimally invasive route to continuous monitoring of glucose in diabetic patients. By expanding the library of analytes detectable with this flexible biosensing platform, a broad array of sensors could be developed for various on-body and in-body monitoring needs, as well as broader health applications such as identifying air or water contamination or detecting spoilage during food production.

Chapter 6: Bibliography

- [1] W. Arden, M. Brillouet, P. Coge, M. Graef, B. Huizing, and R. Mahnkopf, “‘More-than-Moore’ White Paper,” 2010.
- [2] A. Nathan, A. Ahnood, M. T. Cole, Y. Suzuki, P. Hiralal, F. Bonaccorso, T. Hasan, L. Garcia-Gancedo, A. Dyadyusha, S. Haque, P. Andrew, S. Hofmann, J. Moultrie, A. J. Flewitt, A. C. Ferrari, M. J. Kelly, J. Robertson, G. A. J. Amaratunga, and W. I. Milne, “Flexible Electronics: The Next Ubiquitous Platform,” *Proc. IEEE*, vol. 100, no. Special Centennial Issue, pp. 1486–1517, May 2012.
- [3] Y. Sun and J. A. Rogers, “Inorganic semiconductors for flexible electronics,” *Adv. Mater.*, vol. 19, no. 15, pp. 1897–1916, 2007.
- [4] W. Lu and C. M. Lieber, “Nanoelectronics from the bottom up,” *Nat. Mater.*, vol. 6, no. 11, pp. 841–50, Nov. 2007.
- [5] V. Subramanian, J. B. Chang, A. de la Fuente Vornbrock, D. C. Huang, L. Jagannathan, F. Liao, B. Mattis, S. Molesa, D. R. Redinger, D. Soltman, and S. K. Volkman, “Printed electronics for low-cost electronic systems: Technology status and application development,” *ESSCIRC 2008 - 34th Eur. Solid-State Circuits Conf.*, pp. 17–24, Sep. 2008.
- [6] R. A. Street, W. S. Wong, S. E. Ready, M. L. Chabinyc, A. C. Arias, S. Limb, A. Salleo, and R. Lujan, “Jet printing flexible displays,” *Mater. Today*, vol. 9, no. 4, pp. 32–37, Apr. 2006.
- [7] C. J. Brinker and G. W. Scherer, *Sol-gel science: the physics and chemistry of sol-gel processing*, vol. 8. 1990.

- [8] L. L. Hench and J. K. West, "The sol-gel process," *Chem. Rev.*, vol. 90, no. 1, pp. 33–72, 1990.
- [9] J. Jang, R. Kitsomboonloha, S. L. Swisher, E. S. Park, H. Kang, and V. Subramanian, "Transparent high-performance thin film transistors from solution-processed SnO₂ / ZrO₂ gel-like precursors.," *Adv. Mater.*, vol. 25, no. 7, pp. 1042–7, Feb. 2012.
- [10] R. A. Street, T. N. Ng, R. A. Lujan, I. Son, M. Smith, S. Kim, T. Lee, Y. Moon, and S. Cho, "Sol-gel solution-deposited InGaZnO thin film transistors.," *ACS Appl. Mater. Interfaces*, vol. 6, no. 6, pp. 4428–37, Mar. 2014.
- [11] K. K. Banger, Y. Yamashita, K. Mori, R. L. Peterson, T. Leedham, J. Rickard, and H. Sirringhaus, "Low-temperature, high-performance solution-processed metal oxide thin-film transistors formed by a 'sol-gel on chip' process.," *Nat. Mater.*, vol. 10, no. 1, pp. 45–50, Jan. 2011.
- [12] M.-G. Kim, M. G. Kanatzidis, A. Facchetti, and T. J. Marks, "Low-temperature fabrication of high-performance metal oxide thin-film electronics via combustion processing," *Nat. Mater.*, vol. 10, no. 5, pp. 382–8, May 2011.
- [13] H. S. Kim, P. D. Byrne, A. Facchetti, and T. J. Marks, "High performance solution-processed indium oxide thin-film transistors.," *J. Am. Chem. Soc.*, vol. 130, no. 38, pp. 12580–12581, 2008.
- [14] J. H. Park, Y. B. Yoo, K. H. Lee, W. S. Jang, J. Y. Oh, S. S. Chae, H. W. Lee, S. W. Han, and H. K. Baik, "Boron-doped peroxy-zirconium oxide dielectric for high-performance, low-temperature, solution-processed indium oxide thin-film transistor.," *ACS Appl. Mater. Interfaces*, vol. 5, no. 16, pp. 8067–75, Aug. 2013.
- [15] J. S. Lee, Y. Kwack, and W. Choi, "Inkjet-printed In₂O₃ thin-film transistor below 200 °C.," *ACS Appl. Mater. Interfaces*, vol. 5, no. 22, pp. 11578–83, Nov. 2013.
- [16] S.-Y. Han, D.-H. Lee, G. S. Herman, and C.-H. Chang, "Inkjet-Printed High Mobility Transparent-Oxide Semiconductors," *J. Disp. Technol.*, vol. 5, no. 12, pp. 520–524, Dec. 2009.
- [17] K. H. Lee, J. H. Park, Y. B. Yoo, W. S. Jang, J. Y. Oh, S. S. Chae, K. J. Moon, J. M. Myoung, and H. K. Baik, "Effects of solution temperature on solution-processed high-performance metal oxide thin-film transistors.," *ACS Appl. Mater. Interfaces*, vol. 5, no. 7, pp. 2585–92, Apr. 2013.
- [18] A. P. Alivisatos, "Perspectives on physical chemistry of semiconductor Nanocrystals," *J. Phys. Chem.*, vol. 100, no. 31, pp. 13226–13239, Jun. 1996.

- [19] Y. Yin and A. P. Alivisatos, "Colloidal nanocrystal synthesis and the organic-inorganic interface," *Nature*, vol. 437, no. 7059, pp. 664–670, Sep. 2005.
- [20] D. Huang, F. Liao, S. Molesa, D. Redinger, and V. Subramanian, "Plastic-compatible low resistance printable gold nanoparticle conductors for flexible electronics," *J. Electrochem. Soc.*, vol. 150, no. 7, p. G412, May 2003.
- [21] M. V Kovalenko, M. Scheele, and D. V Talapin, "Colloidal nanocrystals with molecular metal chalcogenide surface ligands," *Science (80-.)*, vol. 324, no. 5933, pp. 1417–1420, 2009.
- [22] D. V Talapin, J. S. Lee, M. V Kovalenko, and E. V Shevchenko, "Prospects of colloidal nanocrystals for electronic and optoelectronic applications," *Chem. Rev.*, vol. 110, no. 1, pp. 389–458, 2009.
- [23] P. Buffat and J.-P. Borel, "Size effect on the melting temperature of gold particles," *Phys. Rev. A*, vol. 13, no. 6, pp. 2287–2298, Jun. 1976.
- [24] K. Nomura, H. Ohta, A. Takagi, T. Kamiya, M. Hirano, and H. Hosono, "Room-temperature fabrication of transparent flexible thin-film transistors using amorphous oxide semiconductors," *Nature*, vol. 432, no. 7016, pp. 488–492, 2004.
- [25] Y. Kuo, "Thin Film Transistor Technology—Past, Present, and Future," *Electrochem. Soc. Interface*, no. 22, pp. 55–61, 2013.
- [26] J. F. Wager and R. Hoffman, "Thin, fast, and flexible," *Spectrum*, Jan. 2011.
- [27] S. Xu, Y. Zhang, L. Jia, K. E. Mathewson, K.-I. Jang, J. Kim, H. Fu, X. Huang, P. Chava, R. Wang, S. Bhole, L. Wang, Y. J. Na, Y. Guan, M. Flavin, Z. Han, Y. Huang, and J. a. Rogers, "Soft microfluidic assemblies of sensors, circuits, and radios for the skin," *Science*, vol. 344, no. 6179, pp. 70–4, Apr. 2014.
- [28] J. A. Fan, W. Yeo, Y. Su, Y. Hattori, W. Lee, S. Jung, Y. Zhang, Z. Liu, H. Cheng, L. Falgout, M. Bajema, T. Coleman, D. Gregoire, R. J. Larsen, Y. Huang, and J. A. Rogers, "Fractal design concepts for stretchable electronics," *Nat. Commun.*, vol. 5, p. 3266, Jan. 2014.
- [29] W. Honda, S. Harada, T. Arie, S. Akita, and K. Takei, "Wearable, Human-Interactive, Health-Monitoring, Wireless Devices Fabricated by Macroscale Printing Techniques," *Adv. Funct. Mater.*, vol. 24, no. 22, pp. 3299–3304, Jun. 2014.
- [30] S.-W. Hwang, H. Tao, D.-H. Kim, H. Cheng, J.-K. Song, E. Rill, M. a Brenckle, B. Panilaitis, S. M. Won, Y.-S. Kim, Y. M. Song, K. J. Yu, A. Ameen, R. Li, Y. Su, M. Yang, D. L. Kaplan, M. R. Zakin, M. J. Slepian, Y. Huang, F. G. Omenetto, and J. a

- Rogers, "A physically transient form of silicon electronics.," *Science*, vol. 337, no. 6102, pp. 1640–4, Sep. 2012.
- [31] C. K. Sen, G. M. Gordillo, S. Roy, R. Kirsner, L. Lambert, T. K. Hunt, F. Gottrup, G. C. Gurtner, and M. T. Longaker, "Human skin wounds: a major and snowballing threat to public health and the economy.," *Wound Repair Regen.*, vol. 17, no. 6, pp. 763–71, 2009.
- [32] H. Hosono, "Ionic amorphous oxide semiconductors: Material design, carrier transport, and device application," *J. Non. Cryst. Solids*, vol. 352, no. 9–20, pp. 851–858, 2006.
- [33] W. S. Seo, H. H. Jo, K. Lee, and J. T. Park, "Preparation and Optical Properties of Highly Crystalline, Colloidal, and Size-Controlled Indium Oxide Nanoparticles," *Adv. Mater.*, vol. 15, no. 10, pp. 795–797, May 2003.
- [34] C. H. Lee, M. Kim, T. Kim, A. Kim, J. Paek, J. W. Lee, S.-Y. Choi, K. Kim, J.-B. Park, and K. Lee, "Ambient pressure syntheses of size-controlled corundum-type In₂O₃ nanocubes.," *J. Am. Chem. Soc.*, vol. 128, no. 29, pp. 9326–7, Jul. 2006.
- [35] M. Niederberger, G. Garnweitner, J. Buha, J. Polleux, J. Ba, and N. Pinna, "Nonaqueous synthesis of metal oxide nanoparticles: Review and indium oxide as case study for the dependence of particle morphology on precursors and solvents," *J. Sol-Gel Sci. Technol.*, vol. 40, no. 2–3, pp. 259–266, Apr. 2006.
- [36] D. Caruntu, K. Yao, Z. Zhang, T. Austin, W. Zhou, and C. J. O'Connor, "One-Step Synthesis of Nearly Monodisperse, Variable-Shaped In₂O₃ Nanocrystals in Long Chain Alcohol Solutions," *J. Phys. Chem. C*, vol. 114, no. 11, pp. 4875–4886, 2010.
- [37] T. Cui, Y. Liu, and M. Zhu, "Field-effect transistors with layer-by-layer self-assembled nanoparticle thin films as channel and gate dielectric," *Appl. Phys. Lett.*, vol. 87, no. 18, p. 183105, 2005.
- [38] S. Dasgupta, R. Kruk, N. Mechau, and H. Hahn, "Inkjet Printed, High Mobility Inorganic-Oxide Field Effect Transistors Processed at Room Temperature," *ACS Nano*, no. 12, pp. 9628–9638, 2011.
- [39] B. A. Ridley, B. Nivi, and J. M. Jacobson, "All-Inorganic Field Effect Transistors Fabricated by Printing," *Science (80-.)*, vol. 286, no. 5440, pp. 746–749, Oct. 1999.
- [40] S. K. Volkman, B. A. Mattis, S. E. Molesa, J. B. Lee, A. de la F. Vornbrock, T. Bakhishev, and V. Subramanian, "A novel transparent air-stable printable n-type semiconductor technology using ZnO nanoparticles," *IEEE Int. Electron Devices Meet.*, pp. 769–772, 2004.

- [41] S. L. Swisher, S. K. Volkman, and V. Subramanian, "Tailoring Indium Oxide Nanocrystal Synthesis Conditions for High-performance Solution-processed Thin-film Transistors," *Under Rev.*
- [42] S. L. Swisher and V. Subramanian, "Multifactorial Analysis of Processing Conditions and Gate Dielectric Materials for Solution-Processed In₂O₃ Nanocrystal Thin-film Transistors," *Prep.*
- [43] X. Lu, H.-Y. Tuan, B. a Korgel, and Y. Xia, "Facile synthesis of gold nanoparticles with narrow size distribution by using AuCl or AuBr as the precursor.," *Chemistry*, vol. 14, no. 5, pp. 1584–91, Jan. 2008.
- [44] W. Xu, H. Wang, L. Ye, and J. Xu, "The role of solution-processed high- κ gate dielectrics in electrical performance of oxide thin-film transistors," *J. Mater. Chem. C*, vol. 2, p. 5389, 2014.
- [45] G. Huang, L. Duan, G. Dong, D. Zhang, and Y. Qiu, "High-Mobility Solution-Processed Tin Oxide Thin-Film Transistors with High- κ Alumina Dielectric Working in Enhancement Mode," *ACS Appl. Mater. Interfaces*, 2014.
- [46] K. Nomura, A. Takagi, T. Kamiya, H. Ohta, M. Hirano, and H. Hosono, "Amorphous oxide semiconductors for high-performance flexible thin-film transistors," *JAPANESE J. Appl. Phys. PART 1 Regul. Pap. SHORT NOTES Rev. Pap.*, vol. 45, no. 5B, p. 4303, 2006.
- [47] G. E. P. Box, J. S. Hunter, and W. J. Hunter, *Statistics for Experimenters: Design, Innovation, and Discovery*, 2nd Editio. John Wiley & Sons Inc, 2005.
- [48] S. M. George, "Atomic layer deposition: An overview," *Chem. Rev.*, vol. 110, no. 1, pp. 111–131, 2010.
- [49] K. Chen, H. Clement Wann, J. Dunster, P. K. Ko, C. Hu, and M. Yoshida, "Mosfet carrier mobility model based on gate oxide thickness, threshold and gate voltages," *Solid. State. Electron.*, vol. 39, no. 10, pp. 1515–1518, 1996.
- [50] C. M. Lochner, Y. Khan, A. Pierre, and A. C. Arias, "All-organic optoelectronic sensor for pulse oximetry," *Nat. Commun.*, vol. 5, pp. 1–7, 2014.
- [51] D.-H. Kim, N. Lu, R. Ma, Y.-S. Kim, R.-H. Kim, S. Wang, J. Wu, S. M. Won, H. Tao, A. Islam, K. J. Yu, T. Kim, R. Chowdhury, M. Ying, L. Xu, M. Li, H.-J. Chung, H. Keum, M. McCormick, P. Liu, Y.-W. Zhang, F. G. Omenetto, Y. Huang, T. Coleman, and J. A. Rogers, "Epidermal electronics.," *Science (80-.)*, vol. 333, no. 6044, pp. 838–843, 2011.

- [52] C. Dagdeviren, B. D. Yang, Y. Su, P. L. Tran, P. Joe, E. Anderson, J. Xia, V. Doraiswamy, B. Dehdashti, X. Feng, B. Lu, R. Poston, Z. Khalpey, R. Ghaffari, Y. Huang, M. J. Slepian, and J. a Rogers, "Conformal piezoelectric energy harvesting and storage from motions of the heart, lung, and diaphragm.," *Proc. Natl. Acad. Sci. U. S. A.*, vol. 111, no. 5, pp. 1927–32, 2014.
- [53] M. Vert, Y. Doi, K.-H. Hellwich, M. Hess, P. Hodge, P. Kubisa, M. Rinaudo, and F. Schué, "Terminology for biorelated polymers and applications (IUPAC Recommendations 2012)," *Pure Appl. Chem.*, vol. 84, no. 2, p. 1, 2012.
- [54] T. Mosmann, "Rapid colorimetric assay for cellular growth and survival: application to proliferation and cytotoxicity assays.," *J. Immunol. Methods*, vol. 65, no. 1–2, pp. 55–63, 1983.
- [55] B. M. Ames, J. McCann, and E. Yamasaki, "Methods for detecting carcinogens and mutagens with Salmonella/mammalian microsomes," *Mutat. Res.*, vol. 31, pp. 347–364, 1975.
- [56] United States Food and Drug Administration, "Guidance for Industry: Safety of Nanomaterials in Cosmetic Products," no. June. pp. 1–16, 2012.
- [57] S. Hackenberg, A. Scherzed, A. Technau, M. Kessler, K. Froelich, C. Ginzkey, C. Koehler, M. Burghartz, R. Hagen, and N. Kleinsasser, "Cytotoxic, genotoxic and pro-inflammatory effects of zinc oxide nanoparticles in human nasal mucosa cells in vitro.," *Toxicol. Vitro.*, vol. 25, no. 3, pp. 657–63, Apr. 2011.
- [58] W. Johnson, W. F. Bergfeld, D. V. Belsito, R. a. Hill, C. D. Klaassen, D. Liebler, J. G. Marks, R. C. Shank, T. J. Slaga, P. W. Snyder, and F. a. Andersen, "Safety Assessment of Tin(IV) Oxide as Used in Cosmetics," *International Journal of Toxicology*, vol. 33, no. 4 Suppl. p. 40S–46S, 2014.
- [59] J. Chevalier, "What future for zirconia as a biomaterial?," *Biomaterials*, vol. 27, no. 4, pp. 535–543, 2006.
- [60] International Organization for Standardization, "ISO 5832-1 Fourth Edition, Implants For Surgery -- Metallic Materials." 2007.
- [61] U.S. Department of Health and Human Services National Toxicology Program, "Chemical Information Profile for Indium Tin Oxide." 2009.
- [62] M. Hirenkumar and S. Siegel, "Poly Lactic-co-Glycolic Acid (PLGA) as Biodegradable Controlled Drug Delivery Carrier," *Polymers (Basel).*, vol. 3, no. 3, pp. 1–19, 2011.

Chapter 6: Bibliography

- [63] United States Food and Drug Administration, “Title 21 of the Code of Federal Regulations Part 73, Subpart C: Color additives exempt from batch certification.” 1977.
- [64] L. C. Becker and I. Boyer, “Safety Assessment of Alumina and Aluminum Hydroxide as Used in Cosmetics,” Washington, DC, 2014.
- [65] ASTM, “Standard Specification for High-Purity Dense Aluminum Oxide for Medical Application.” ASTM, pp. 1–3, 2012.
- [66] S. L. Swisher, M. C. Lin, A. Liao, E. J. Leeﬂang, Y. Khan, F. J. Pavinatto, K. Mann, A. Naujokas, D. Young, S. Roy, M. R. Harrison, A. C. Arias, V. Subramanian, and M. M. Maharbiz, “Impedance sensing device enables early detection of pressure ulcers in vivo,” *Nat. Commun.*, vol. 6, pp. 1–10, 2015.
- [67] J. D. Bauer, J. S. Mancoll, and L. G. Phillips, “Pressure Sores,” in *Grabb and Smith’s Plastic Surgery*, 6th editio., C. H. Thorne, Ed. Philadelphia, PA: Lippincott Williams & Wilkins, 2007, pp. 722–729.
- [68] E. Ayello and C. Lyder, “A New Era of Pressure Ulcer Accountability in Acute Care,” *Adv. Skin Wound Care*, vol. 21, no. 3, pp. 134–140, 2008.
- [69] V. Wong, “Skin blood flow response to 2-hour repositioning in long-term care residents: a pilot study,” *J. Wound. Ostomy Continence Nurs.*, vol. 38, no. 5, pp. 529–37, 2011.
- [70] M. Reddy, S. S. Gill, and P. A. Rochon, “Preventing pressure ulcers: a systematic review,” *JAMA*, vol. 296, no. 8, pp. 974–84, Aug. 2006.
- [71] J.-P. Morucci, M. Valentinuzzi, B. Rigaud, C. Felice, N. Chauvea, and P.-M. Marsili, “Bioelectrical impedance techniques in medicine,” *Crit. Rev. Biomed. Eng.*, vol. 24, no. 4–6, pp. 223–681, 1996.
- [72] S. Grimnes and Ø. G. Martinsen, *Bioimpedance and Bioelectricity Basics*. Elsevier, 2008.
- [73] H. C. Lukaski, “Evolution of bioimpedance: a circuitous journey from estimation of physiological function to assessment of body composition and a return to clinical research,” *Eur. J. Clin. Nutr.*, vol. 67 Suppl 1, no. S1, pp. S2–9, Jan. 2013.
- [74] G. H. Markx and C. L. Davey, “The dielectric properties of biological cells at radiofrequencies: Applications in biotechnology,” *Enzyme Microb. Technol.*, vol. 25, pp. 161–171, 1999.

Chapter 6: Bibliography

- [75] P. Patel and G. H. Markx, “Dielectric measurement of cell death,” *Enzyme Microb. Technol.*, vol. 43, no. 7, pp. 463–470, Dec. 2008.
- [76] D. B. Kell, G. H. Markx, C. L. Davey, and R. W. Todd, “Real-time monitoring of cellular biomass: methods and applications,” *Trends Anal. Chem.*, vol. 9, no. 6, pp. 190–194, 1990.
- [77] A. R. A. Rahman, J. Register, G. Vuppala, and S. Bhansali, “Cell culture monitoring by impedance mapping using a multielectrode scanning impedance spectroscopy system (CellMap),” *Physiol. Meas.*, vol. 29, no. 6, pp. S227–39, Jun. 2008.
- [78] M. Dabros, D. Dennewald, D. J. Currie, M. H. Lee, R. W. Todd, I. W. Marison, and U. von Stockar, “Cole-Cole, linear and multivariate modeling of capacitance data for on-line monitoring of biomass,” *Bioprocess Biosyst. Eng.*, vol. 32, no. 2, pp. 161–73, Feb. 2009.
- [79] P. Linderholm, T. Braschler, J. Vannod, Y. Barrandon, M. Brouard, and P. Renaud, “Two-dimensional impedance imaging of cell migration and epithelial stratification,” *Lab Chip*, vol. 6, no. 9, pp. 1155–62, Sep. 2006.
- [80] M. F. Moore, N. Dobson, L. Castellino, and S. Kapp, “Phase angle, an alternative physiological tool to assess wound treatment in chronic nonhealing wounds,” *J. Am. Col. Certif. Wound Spec.*, vol. 3, no. 1, pp. 2–7, Mar. 2011.
- [81] N. Bergstrom, B. J. Braden, A. Laguzza, and V. Holman, “The Braden Scale for predicting pressure sore risk,” *Nurs. Res.*, vol. 36, no. 4, pp. 205–210, 1987.
- [82] D. Wagner, K. Jeter, T. Tintle, M. Martin, and J. Long, “Bioelectrical impedance as a discriminator of pressure ulcer risk,” *Adv. Wound Care*, vol. 9, no. 2, pp. 30–37, 1996.
- [83] H. C. Lukaski and M. Moore, “Bioelectrical impedance assessment of wound healing,” *J. Diabetes Sci. Technol.*, vol. 6, no. 1, pp. 209–12, Jan. 2012.
- [84] “Proof-of-concept Study for Bioimpedance Based Monitoring of Venous Ulcers During Galvanic Stimulation (NCT02101645). Tampere University Hospital, Tampere, Finland.” 2014.
- [85] D. D. Drinan and C. F. Edman, “Monitoring Platform for Wound and Ulcer Monitoring and Detection,” US 2006/0052678 A12006.
- [86] J. T. Alander, I. Kaartinen, A. Laakso, T. Pätälä, T. Spillmann, V. V. Tuchin, M. Venermo, and P. Välisuo, “A Review of indocyanine green fluorescent imaging in surgery,” *International Journal of Biomedical Imaging*, vol. 2012. 2012.

- [87] S. B. Fuller, E. J. Wilhelm, and J. M. Jacobson, "Ink-jet printed nanoparticle microelectromechanical systems," *J. Microelectromechanical Syst.*, vol. 11, no. 1, pp. 54–60, 2002.
- [88] W. Cui, W. Lu, Y. Zhang, G. Lin, T. Wei, and L. Jiang, "Gold nanoparticle ink suitable for electric-conductive pattern fabrication using in ink-jet printing technology," *Colloids Surfaces A Physicochem. Eng. Asp.*, vol. 358, no. 1–3, pp. 35–41, Apr. 2010.
- [89] E. T. McAdams, J. Jossinet, a Lackermeier, and F. Risacher, "Factors affecting electrode-gel-skin interface impedance in electrical impedance tomography.," *Med. Biol. Eng. Comput.*, vol. 34, no. 6, pp. 397–408, Nov. 1996.
- [90] I. Stadler, R.-Y. Zhang, P. Oskoui, M. S. Whittaker, and R. J. Lanzafame, "Development of a simple, noninvasive, clinically relevant model of pressure ulcers in the mouse.," *J. Invest. Surg.*, vol. 17, no. 4, pp. 221–7, 2004.
- [91] E. C. Herrman, C. F. Knapp, J. C. Donofrio, and R. Salcido, "Skin perfusion responses to surface pressure-induced ischemia: implication for the developing pressure ulcer.," *J. Rehabil. Res. Dev.*, vol. 36, no. 2, pp. 109–20, Apr. 1999.
- [92] S. M. Peirce, T. C. Skalak, and G. T. Rodeheaver, "Ischemia-reperfusion injury in chronic pressure ulcer formation: a skin model in the rat.," *Wound Repair Regen.*, vol. 8, no. 1, pp. 68–76, 2000.
- [93] Y. Saito, M. Hasegawa, M. Fujimoto, T. Matsushita, M. Horikawa, M. Takenaka, F. Ogawa, J. Sugama, D. a Steeber, S. Sato, and K. Takehara, "The loss of MCP-1 attenuates cutaneous ischemia-reperfusion injury in a mouse model of pressure ulcer.," *J. Invest. Dermatol.*, vol. 128, no. 7, pp. 1838–51, Jul. 2008.
- [94] R. Nuccitelli, "A Role for Endogenous Electric Fields in Wound Healing," *Curr. Top. Dev. Biol.*, vol. 58, 2003.
- [95] M. Zhao, B. Song, J. Pu, T. Wada, B. Reid, G. Tai, F. Wang, A. Guo, P. Walczysko, Y. Gu, T. Sasaki, A. Suzuki, J. V Forrester, H. R. Bourne, P. N. Devreotes, C. D. McCaig, and J. M. Penninger, "Electrical signals control wound healing through phosphatidylinositol-3-OH kinase-gamma and PTEN.," *Nature*, vol. 442, no. 7101, pp. 457–60, Jul. 2006.
- [96] B. Song, Y. Gu, J. Pu, B. Reid, Z. Zhao, and M. Zhao, "Application of direct current electric fields to cells and tissues in vitro and modulation of wound electric field in vivo.," *Nat. Protoc.*, vol. 2, no. 6, pp. 1479–89, Jan. 2007.
- [97] L. Li, W. Gu, J. Du, B. Reid, X. Deng, Z. Liu, Z. Zong, H. Wang, B. Yao, C. Yang, J. Yan, L. Zeng, L. Chalmers, M. Zhao, and J. Jiang, "Electric fields guide migration of

Chapter 6: Bibliography

- epidermal stem cells and promote skin wound healing.,” *Wound Repair Regen.*, vol. 20, no. 6, pp. 840–51, Nov. 2012.
- [98] D. J. Cohen, W. J. Nelson, and M. M. Maharbiz, “Galvanotactic control of collective cell migration in epithelial monolayers.,” *Nat. Mater.*, vol. 13, no. 4, pp. 409–17, Apr. 2014.
- [99] R. R. Isseroff and S. E. Dahle, “Electrical Stimulation Therapy and Wound Healing: Where Are We Now?,” *Adv. Wound Care*, vol. 1, no. 6, pp. 238–243, Dec. 2012.

Appendix A: Nanocrystal TFT Fabrication Process

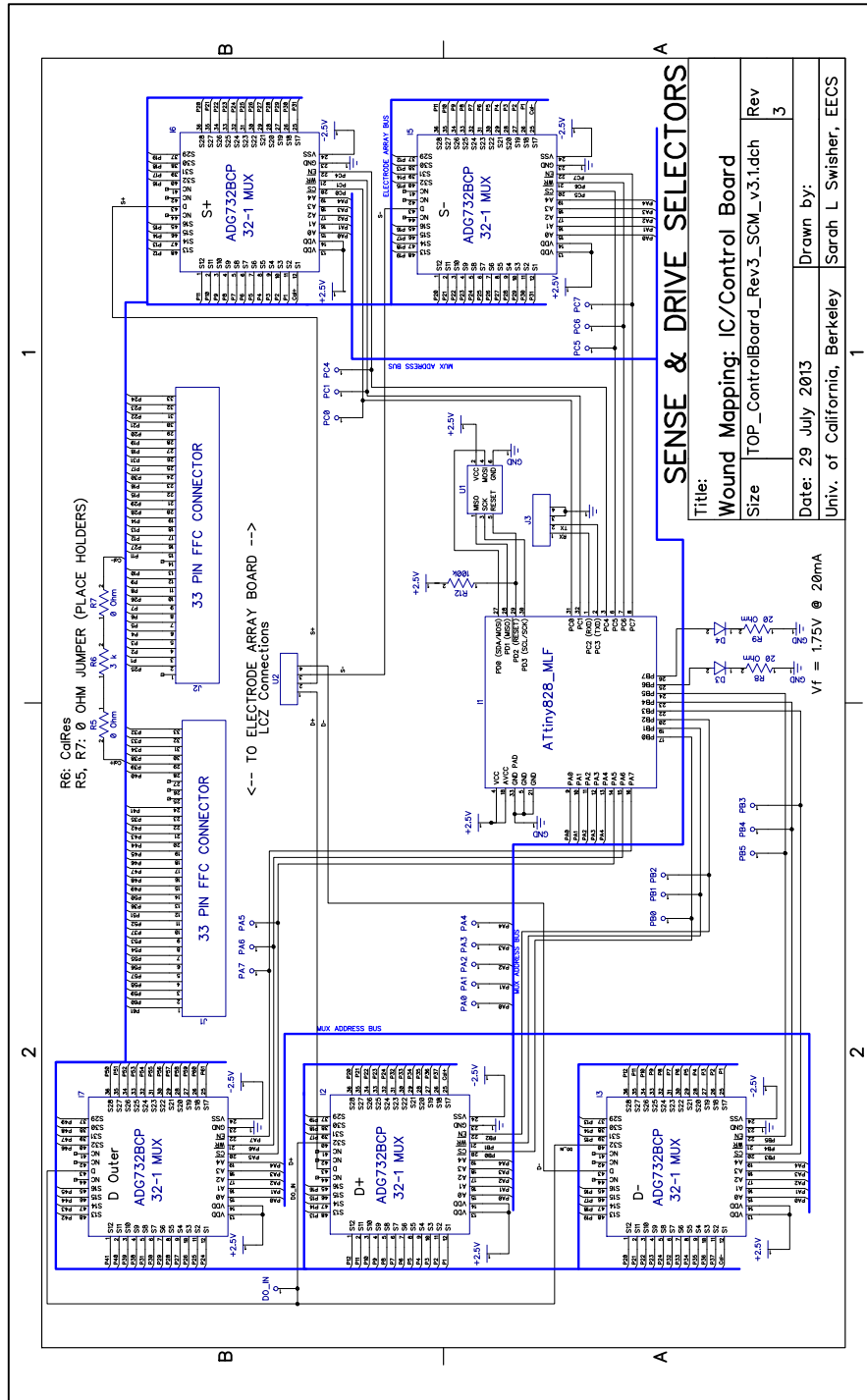
This process flow was designed for the tools in the UC Berkeley Marvell Nanofabrication Laboratory, except where noted.

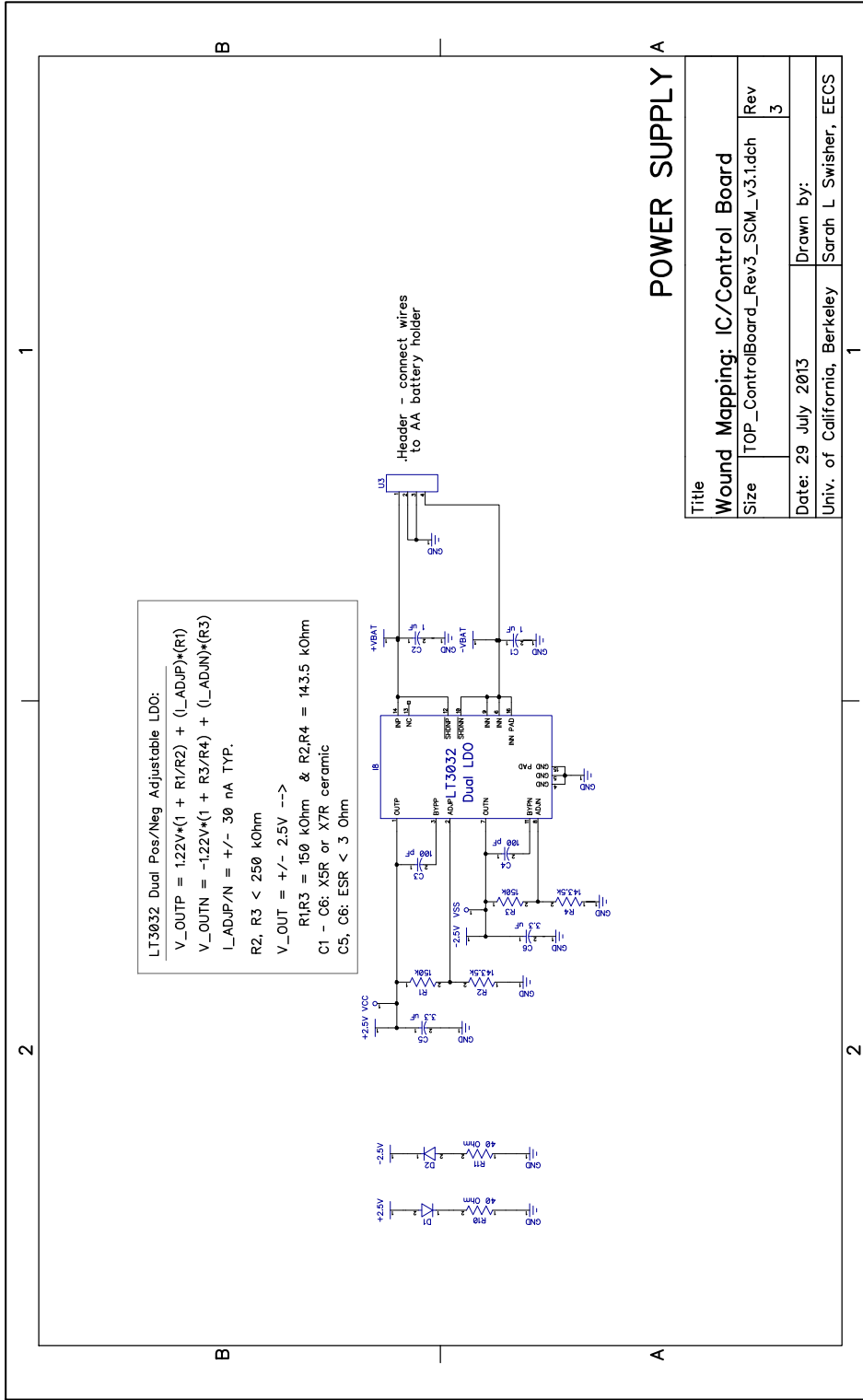
INDIUM OXIDE NANOPARTICLE TFT FABRICATION PROCESS

Sarah Swisher, January 2014
UC Berkeley, EECS – Subramanian Group

Seq. Step No.	PROCESS STEP	SUB STEPS	TOOL / RECIPE	TARGET AND PROCESS SPEC	Notes
1	STARTING WAFERS			<0.005 ohm-cm, n-type, <100>, 4"	n++ wafers purchased from SQI
** Perform either step 2A (for high-K gate dielectric) or step 2B (for SiO2), but NOT both. **					
2A	HIGH-K GATE OXIDE (Stanford Nanolab)	a) RCA clean wafers	Wbdiff	RCA1: 10 min in 5:1:1 H2O:NH4OH:H2O2 @ 50C. RCA2: 10 min in 5:1:1 H2O:HCl:H2O2 @ 70C.	
		b) Deposit HfO2	Fiji1/2, Std Plasma HfO2	500 cycles @ 250C (-1A/cycle)	Measure thickness, uniformity on WOOLLAM
		c) Deposit ZrO2	Savannah, Std Thermal ZrO2	625 cycles @ 200C (-0.9A/cycle)	Measure thickness, uniformity on WOOLLAM
2B	GATE OXIDATION	a) TCA clean	Tystar1, 1TCA	-8 hours, run overnight	
		b) Std. clean wafers	msink6	10 min Piranha + ~1 min 10:1 HF, until dewet	
		c) Dry oxidation	Tystar1, 1GATEOXA	Target = 170A, 900C, 50 min oxidation @ 950C, 20 min N2 anneal NP dispersed in chloroform. Filter = 0.45um pore size, 25mm diameter PTFE. Adjust concentration to ~1 wt%.	Measure oxide thickness using ELLIPS
3	SEMI DEPOSITION	a) Prepare In2O3 Ink	188 Cory synthetic lab	170ml H2SO4 + 26 ml H2O2 (-6.5:1) in glass beaker or crystallization dish. Submerge samples for 10 min. DI Rinse, N2 dry.	Special chemical approved for use at headway by Bill Flounders and Bob Hamilton
		b) Cleave wafers	Nanolab	Quarter wafers	
		c) Gate oxide clean	msink16/18, Piranha	Static dispense; 60 sec @ 5000rpm, 1000rpm/sec	Self-heating solution, no external heat needed.
		d) Spin-coat In2O3	headway	Dispense -0.4mL for 1/4 wafer. Start drop away from wafer to prevent splatter	
4	ANNEAL	a) Cleave samples		Cleave 1/4 wafers into samples <= 1"	Scribe backside with material code or Sample ID
		b) Anneal	1" tube furnace, 432 Cory	Ramp from 0C ==> Tanneal @ 5C/min; Dwell 60 min.	Ambient gas flow; tank output pressure = 5psi, manifold fully open. Flow meter = 5 for 10min @ RT to purge, then reduce flow to 4 for ramp and anneal. Tube output goes through oil bubbler. (Flow meter reading is not quantitative - only calibrated for N2.)
5	S/D LITHO	a) Spin i-line PR	headway, Prog #1	1) 30 sec manual dispense @ 0 rpm 2) 1 sec @ 500 rpm, 1krpm/sec 3) 1.5 sec @ 500 rpm, 10krpm/sec 4) 30sec @ 4100 rpm, 20krpm/sec	OCG OR-700 10, Positive PR for i-line
		b) Softbake	hotplate	60 sec @ 90C	
		c) Exposure	ksaligner	155 mJ/cm2 for i-line	Mask: DenseShadow Hard Contact Mode 50 um Alignment gap Exp. Time = (155 mW*sec/cm2) / (intensity mW/cm2). Add 10% overexposure.
		d) PEB	hotplate	60 sec @ 120C	
		e) Develop	msink3	1 min in developer, DI rinse, N2 dry	ODP HPRD 4262 Developer (1-2% TMAH. Completely miscible with water; aspirate to dispose.)
		f) Inspect pattern	olympus; asiq	PR thickness ~ 1.1um	check for straight edges, fully cleared PR from electrode pattern
		g) Hard bake	oven	30 min @ 120C	Hard-bake required for CHA
6	S/D METAL DEP	a) e-beam Al deposition	CHA, standard Aluminum recipe	Pump down to 5 E-7 Torr prior to deposition. Ensure that aluminum carbide skin is pierced during soak! Deposit 80-100 nm @ 5A/sec	Fabmate coated graphite crucible, edges sanded sharp. 99.999% pure Al pellets.
7	LIFT-OFF	a) Remove PR and unwanted metal	msink18	Sonicate in acetone until pattern is cleared, ~5 minutes	
		b) Inspect pattern	olympus	Ensure all S/D patterns are clear, no residual metal near devices.	
8	ACTIVE AREA LITHO	a) Spin i-line PR	headway, Prog #1	1) 30 sec manual dispense @ 0 rpm 2) 1 sec @ 500 rpm, 1krpm/sec 3) 1.5 sec @ 500 rpm, 10krpm/sec 4) 30sec @ 4100 rpm, 20krpm/sec	OCG OR-700 10, Positive PR for i-line
		b) Softbake	hotplate	60 sec @ 90C	
		c) Exposure	ksaligner	155 mJ/cm2 for i-line	Mask: Active_Area_L2 Hard Contact Mode 50 um Alignment gap Exp. Time = (155 mW*sec/cm2) / (intensity mW/cm2). Add 10% overexposure.
		d) PEB	hotplate	60 sec @ 120C	
		e) Develop	msink3	1 min in developer, DI rinse, N2 dry	ODP HPRD 4262 Developer (1-2% TMAH. Completely miscible with water; aspirate to dispose.)
9	ACTIVE AREA ETCH	a) Wet etch In2O3 NP	msink16/18	ensure proper alignment of AA to S/D. Misalignment will destroy Al S/D during AA etch! 5 min submerged in 1:1 HCl:H2O. DI rinse, N2 dry.	12.1M HCl provided at msink16/18, 1:1 dilution results in 6M HCl etchant.
		b) Remove PR	msink16/18	Submerge in acetone ~1min or spray with squeeze bottle. DI rinse, N2 dry.	
		c) Inspect pattern	Olympus	Measure dimensions of electrodes. Check edges of AA, and margin of AA above/below the S/D pads.	

Appendix B: Impedance Sensor Control Board Circuit Schematic





POWER SUPPLY

Title	
Wound Mapping: IC/Control Board	
Size	TOP_ControlBoard_Rev3_SCM_v3.1.dch
Rev	3
Date: 29 July 2013	
Drawn by: Sarah L Swisher, EECS	

Appendix C: Impedance Sensor Control Board Bill of Materials

IC/Control Board Rev 3 BOM
Page 1 of 2

Project NSF EFRI Wound Mapping
Board Name IC/Control Board
Version Rev3
Schematic File TOP_ControlBoard_Rev3_SCM_v3.1.dch
PCB Layout File TOP_ControlBoard_Rev3_PCB_v3.1.dip
Assembly Drawing
Date 7-Aug-13
Last Revised by Sarah Swisher

BILL OF MATERIALS						
Ref Des	Description	Value	Manfr.	Manufacturer Part Number	Digi-key Part Number	Qty
C1	Capacitor, 0402, X5R or X7R Ceramic	1 uF	TDK Corporation	C1005X5R0J105K050BB	445-4998-1-ND	1
C2	Capacitor, 0402, X5R or X7R Ceramic	1 uF	TDK Corporation	C1005X5R0J105K050BB	445-4998-1-ND	1
C3	Capacitor, 0402, X5R or X7R Ceramic	100 pF	AVX Corporation	0402YC101KAT2A	478-7887-1-ND	1
C4	Capacitor, 0402, X5R or X7R Ceramic	100 pF	AVX Corporation	0402YC101KAT2A	478-7887-1-ND	1
C5	Capacitor, 0402, X5R or X7R Ceramic, ESR < 3 Ohm	3.3 uF	TDK Corporation	C1005X5R0J335K050BC	445-5946-1-ND	1
C6	Capacitor, 0402, X5R or X7R Ceramic, ESR < 3 Ohm	3.3 uF	TDK Corporation	C1005X5R0J335K050BC	445-5946-1-ND	1
D1	LED 0603, Red, 1.75V		Rohm Semi	SML-310LT	511-1298-1-ND	1
D2	LED 0603, Red, 1.75V		Rohm Semi	SML-310LT	511-1298-1-ND	1
D3	LED 0603, Red, 1.75V		Rohm Semi	SML-310LT	511-1298-1-ND	1
D4	LED 0603, Red, 1.75V		Rohm Semi	SML-310LT	511-1298-1-ND	1
I1	ATTiny828, 8-bit AVR Microcontroller, 32 pin MLF package		Atmel	ATTiny828-MU	ATTINY828-MU-ND	1
I2	Analog Devices 32 Channel Analog	32-1 MUX	Analog Devices	ADG732BCPZ	ADG732BCPZ-ND	1
I3	Analog Devices 32 Channel Analog	32-1 MUX	Analog Devices	ADG732BCPZ	ADG732BCPZ-ND	1
I5	Analog Devices 32 Channel Analog	32-1 MUX	Analog Devices	ADG732BCPZ	ADG732BCPZ-ND	1
I6	Analog Devices 32 Channel Analog	32-1 MUX	Analog Devices	ADG732BCPZ	ADG732BCPZ-ND	1
I7	Analog Devices 32 Channel Analog	32-1 MUX	Analog Devices	ADG732BCPZ	ADG732BCPZ-ND	1
I8	Dual Pos/Neg Low Noise LDO, Adjustable Output, 14 pin DFN		Linear Technologies	LT3032IDE or LT3032EDE	LT3032EDE#PBF-ND	1
J1	0.5mm pitch FFC connector, LVDS shielded, bottom contact		Molex	502244-3330	Mouser 538-502244-3330	1

IC/Control Board Rev 3 BOM
Page 2 of 2

J2	0.5mm pitch FFC connector, LVDS shielded, bottom contact		Molex	502244-3330	Mouser 538-502244-3330	1
J3	Header Receptacle, Top entry, 4-pin	Tx,Rx	Molex	22-02-2045	WM3202-ND	1
R1	Resistor, 0402, 150k, 1%, 1/10W	150k	Panasonic	ERJ-2RKF1503X	P150KLCT-ND	1
R2	Resistor, 0402, 143k, 1%, 1/10W	143k	Panasonic	ERJ-2RKF1433X	P143KLCT-ND	1
R3	Resistor, 0402, 150k, 1%, 1/10W	150k	Panasonic	ERJ-2RKF1503X	P150KLCT-ND	1
R4	Resistor, 0402, 143k, 1%, 1/10W	143k	Panasonic	ERJ-2RKF1433X	P143KLCT-ND	1
R5	Resistor, 0402, 0 Jumper, 1/10W	0 Ohm	Panasonic	ERJ-2GE0R00X	P0.0JDKR-ND	1
R6	Resistor, 0402, 3k, 1%, 1/10W	3 k	Panasonic	ERJ-2RKF3001X	P3.00KLCT-ND	1
R7	Resistor, 0402, 0 Jumper, 1/10W	0 Ohm	Panasonic	ERJ-2GE0R00X	P0.0JDKR-ND	1
R8	Resistor, 0402, 20, 1%, 1/10W	20 Ohm	Panasonic	ERJ-2RKF20R0X	P20.0LCT-ND	1
R9	Resistor, 0402, 20, 1%, 1/10W	20 Ohm	Panasonic	ERJ-2RKF20R0X	P20.0LCT-ND	1
R10	Resistor, 0402, 40.2, 1%, 1/10W	40 Ohm	Panasonic	ERJ-2RKF40R2X	P40.2LCT-ND	1
R11	Resistor, 0402, 40.2, 1%, 1/10W	40 Ohm	Panasonic	ERJ-2RKF40R2X	P40.2LCT-ND	1
R12	Resistor, 0402, 100k, 1%, 1/10W	100k	Panasonic	ERJ-2RKF1003X	P100KLTR-ND	1
U1	AVR ISP Header, 6 pin, Shrouded				N/A	0
U2	Header Receptacle, Top entry, 4-pin	LCZ	Molex	22-02-2045	WM3202-ND	1
U3	Header Receptacle, Top entry, 4-pin	PWR	Molex	22-02-2045	WM3202-ND	1